Electromagnetic Imaging of the marine subsurface: A novel approach to assess sediment patterns and dynamics on clastic shelf systems

Benjamin Baasch

Faculty of Geosciences

University of Bremen

A thesis submitted for the doctoral degree in natural sciences

(Dr. rer. nat.)

Colloquium held on 12/12/2016

Reviewers: Prof. Dr. Tilo von Dobeneck and PD Dr. Christian Winter

Versicherung an Eides Statt

Ich, _____
(Vorname, Name, Anschrift, Matr.-Nr.)

versichere an Eides Statt durch meine Unterschrift, dass ich die vorstehende Arbeit selbständig und ohne fremde Hilfe angefertigt und alle Stellen, die ich wörtlich dem Sinne nach aus Veröffentlichungen entnommen habe, als solche kenntlich gemacht habe, mich auch keiner anderen als der angegeben Literatur oder sonstiger Hilfsmittel bedient habe.

Ich versichere an Eides Statt, dass ich die vorgenannten Angaben nach bestem Wissen und Gewissen gemacht habe und dass die Angaben der Wahrheit entsprechen und ich nichts verschwiegen habe.

Die Strafbarkeit einer falschen eidesstattlichen Versicherung ist mir bekannt, namentlich die Strafandrohung gemäß § 156 StGB bis zu drei Jahren Freiheitsstrafe oder Geldstrafe bei vorsätzlicher Begehung der Tat bzw. gemäß § 161 Abs. 1 StGB bis zu einem Jahr Freiheitsstrafe oder Geldstrafe bei fahrlässiger Begehung.

_____ _____
Ort, Datum Unterschrift

Acknowledgements

First of all I would like to thank my supervisor Tilo von Dobeneck for offering me the possibility doing this PhD and for the great support throughout this PhD project. I am especially grateful that it has been possible to continue this project from abroad.

Special thanks to my co-supervisor Hendrik Müller for introducing me to the small but great world of Marine EM Profiling. It has always been great to work with you in the office and on the water. I hope we can keep this going somehow.

Christian Hilgenfeldt, thank you for your help and support, for your outstanding work on NERIDIS III, which made this PhD project possible.

Janna Just, I had the pleasure to share the office with you during the whole three years in Bremen. Thanks for the daily lunch break and organising the numerous get-togethers.

Heike Piero, Liane Brück and Martina Braun, I thank you for doing a very good job and being helpful and friendly colleagues all the time which makes working so much easier.

Many thanks to all other recent and former members of the Marine Geophysics Group who passed my way and created a nice working atmosphere including Firoz Badesab,Thomas Frederichs, Cletus Itambi, Lucy Korff, Sebastian Razik, Tobias Kulgemeyer, Vera Bender, Konstantin Reeck, Max Kluger and Grasiane Luz Mathias.

Ferdinand Oberle, we had many inspiring conversations, good cooperation and every now and then a few good beers. Thanks for that. Thanks to Jan Schröder for cycling on a GLOMAR tandem with me.

I am deeply grateful for having so many good friends who do not contributed at all to this thesis, but just make my life better. This includes all the Moabiter boys and girls (and all remaining friends from Berlin), all Friends from MARUM, my flat mates from the Schwachhauser Heerstraße and during the last three years the Thirsty Thursday crew who has introduced me to the English culture.

In the end, I would like to thank my family for the encouragement, trust and support during my entire life.

Abstract

Electromagnetic (EM) imaging is a new approach to investigate marine near-surface sediments. The EM data provide information about electric conductivity and magnetic susceptibility of the sediments. Both are important physical parameters in exploration geophysics. Electric conductivity of marine sediments is a function of porosity, tortuosity and chemistry of the pore fluid. Magnetic susceptibility indicates the magnetic particle concentration and is hence related to the mineral composition of the sediment. In this thesis data processing, inversion and machine learning methods for a novel marine EM profiling system are developed, with the goal to explore the internal structure and spatial variability of sediment patterns in coastal and shelf regions. The investigated EM data were acquired on the NW Iberian shelf during the Meteor cruise M84/4b with the bottom towed electromagnetic profiler MARUM NERIDIS III. This non-conductive, non-magnetic fiberglass sled accommodates a controlled source electromagnetic system based on a frequency-domain concentric-loop EM induction sensor. In order to estimate quantitative seafloor sediment properties from the NERIDIS III EM data, the approach developed in this thesis follows three main steps: The first step is to calibrate the EM data such that instrument related bias is removed and the EM response is solely controlled by the frequency of the source signal, the system geometry, the electric conductivity and magnetic susceptibility of the seawater and the sediment. Calibration is necessary to make data from different measurements and surveys comparable and to enable solving of the ill-posed inverse problem for electric conductivity and magnetic susceptibility. This thesis shows that calibrating the primary EM field alone, by means of independently measured water conductivity and constant water susceptibility, is not sufficient. Therefore, a calibration methodology is developed which firstly calibrates the recorded EM data to compensate for bias in the primary EM field followed by a secondary EM field calibration by means of ground-truth data. The second step involves the inversion of the EM data, which can be subdivided into a half-space and 1-D inversion. The half-space inversion aims for the reconstruction of bulk sediment conductivity and susceptibility of the uppermost approximately 0.5 to 1 m. It is demonstrated that recovered half-space conductivity and susceptibility well reflect

the main sediment patterns on the NW Iberian shelf and allow the reconstruction of sediment pathways. The 1-D inversion can be used to reconstruct the vertical conductivity structure of the subsurface. An algorithm is developed which employs the half-space susceptibility as a priori information and hence allows the utilisation of the in-phase component of the complex earth response increasing the depth of investigation. It is shown that vertical conductivity variations down to approximately 3 m below the seafloor can be reconstructed revealing the internal structure of the Galician Mud Belt. The third step covers the predictive modelling of grain-size from the electric conductivity and magnetic susceptibility of the sediment. Correlation analyses are carried out which reveal a strong relation between the electromagnetic and textural sediment properties. A radial basis function network is developed which predicts the entire grain-size distribution for each EM measurement location along shelf wide survey lines. The predicted grain-size distributions are used to identify the well-known sediment facies on the NW Iberian shelf and give new insights into their distribution and transitions.

Kurzfassung

Die elektromagnetische (EM) Sondierung ist ein neues Verfahren für die Untersuchung von marinen oberflächennahen Sedimenten. Die EM-Daten bieten Informationen über die elektrische Leitfähigkeit und magnetische Suszeptibilität der Sedimente. Beides sind wichtige physikalische Parameter in der Explorationsgeophysik. Die elektrische Leitfähigkeit von marinen Sedimenten ist eine Funktion der Porosität, der Tortuosität und der chemischen Zusammensetzung des Porenwassers. Die magnetische Suszeptibilität gibt den Anteil der magnetischen Teilchen an und steht somit im Bezug zu der mineralogischen Zusammensetzung des Sediments. Diese Doktorarbeit entwickelt Datenbearbeitungs-, Inversions- sowie maschinelle Lernverfahren für ein neues marine EM-System, mit dem Ziel, den inneren Aufbau und die räumliche Variabilität von Sedimentstrukturen in Schelf- und Küstengebieten zu erforschen. EM-Daten, aufgenommen auf dem NW iberischen Schelf, werden untersucht. Die Daten wurden während der Meteor Forschungsfahrt M84-4b mit dem elektromagnetischen Benthosschlitten Marum Neridis III gemessen, der in direktem Grundkontakt hinter dem Schiff geschleppt wird. Dieser nichtleitende und nichtmagnetische glasfaserverstärkte Kunststoffschlitten bietet Platz für ein EM-System, das auf einem im Frequenzbereich arbeitenden konzentrischen Induktionsspulensytem mit künstlicher Anregung beruht. Um quantitative Merkmale der Meeresbodensedimente zu ermitteln, folgt der Ansatz, der in dieser Doktorarbeit entwickelt wird, drei wesentlichen Schritten: Im ersten Schritt werden die EM-Daten kalibriert, so dass systematische Messabweichungen entfernt werden und die EM-Antwort ausschließlich von der Frequenz des Sendesignals, der Sensorgeometrie, der elektrischen Leitfähigkeit und der magnetischen Suszeptibilität des Meereswassers und des Sedimentes abhängt. Die Kalibrierung ist notwendig, um Daten von unterschiedlichen Messungen vergleichbar zu machen und das schlecht gestellte inverse Problem für die elektrische Leitfähigkeit und magnetische Suszeptibilität zu lösen. Diese Doktorarbeit zeigt, dass die Kalibrierung des EM-Primärfeldes alleine mit Hilfe von unabhängig gemessener Wasserleitfähigkeit und konstanter Wassersuszeptibilität nicht ausreichend ist. Aus diesem Grund wurde eine Kalibrierungsmethode entwickelt, die zuerst die aufgenommenen EM-Daten korrigiert, um Messabweichungen des EM-Primärfeldes zu kompensieren

und anschließend das EM-Sekundärfeld mit Hilfe von Bodenproben kalibriert. Der zweite Schritt beinhaltet die Inversion der EM-Daten, welche weiter in Halbraum- und 1-D-Inversion unterteilt werden kann. Die Halbrauminversion hat das Ziel die Gesamtleitfähigkeit und -suszeptibilität des obersten ca. 0,5 bis 1 m zu ermitteln. Es wird nachgewiesen, dass die so ermittelte Halbraumleitfähigkeit und -suszeptibilität die Hauptsedimentstrukturen auf dem NW iberischen Schelf gut widerspiegeln und die Rekonstruktion von Sedimenttransportwegen ermöglichen. Die 1-D-Inversion kann verwendet werden, um die vertikale Leitfähigkeitsstruktur des Untergrundes zu rekonstruieren. Ein Algorithmus wird entwickelt, der die Halbraumsuszeptibilität als A-priori-Information verwendet und es somit ermöglicht, den Realteil (In-Phase) des komplexen Messsignals in die Inversion mit einzubeziehen. Es wird gezeigt, dass vertikale Leitfähigkeitsänderungen bis zu einer Tiefe von ungefähr 3 m unterhalb des Meeresbodens ermittelt und damit die interne Struktur des "Galizischen Schlammgürtels" erkundet werden kann. Der dritte Schritt umfasst die Entwicklung von Vorhersagemodellen zur Bestimmung von Korngrößen anhand von elektrischer Leitfähigkeit und magnetischer Suszeptibilität. Korrelationsanalysen werden durchgeführt, welche einen starken Zusammenhang zwischen den elektromagnetischen und strukturellen Sedimenteigenschaften aufzeigen. Ein künstliches neuronales Netz aus radialen Basisfunktionen wird entwickelt, welches die gesamte Korngrößenverteilungskurve für jeden EM-Messpunkt entlang der Messprofile auf dem Schelf berechnet. Die so vorhergesagten Korngrößenverteilungen werden dazu verwendet, die bekannten Sedimentfazien auf dem NW iberischen Schelf zu identifizieren. Ferner geben sie neue Einblicke in deren Verteilung und deren Übergänge.

Contents

Chapter 1

Introduction

Continental shelves and coastal areas have a great political, economic and ecological importance for modern societies worldwide. Most of the marine resources from hydrocarbons to food supplies are located on continental shelves which cover only 32 million km^2 or about 8.9 % of the total area of the oceans (Harris et al. 2014). As a consequence of the wealth of resources and a higher quality of life, half of the world's population lives within 60 miles of the coast, and this proportion may increase to 70 % in 2020 (FAO 2014). The high population together with the intense exploitation of natural resources and other industrial activities such as shipping, tourism and power generation from waves, tidal currents and offshore wind has led to an enormous ecological pressure on the on average only 75 km wide (Shepard 1963) continental shelves. Additionally, coastal zones are strongly affected by climate change and natural hazards including extreme weather events, flooding, erosion and sea level rise (Dilley et al. 2005; McGranahan et al. 2007). It is therefore a major challenge for integrated coastal management to find the balance between economic and environmental interests.

From a sedimentological point of view, clastic shelf systems as major sediment sources and sinks build critical interfaces between the continent and ocean on the sediment pathway. Freshwater, suspended fine material, as well as carbon, nutrients and anthropogenic contaminants are transported from estuaries to the shelf where they are stored, reworked, redistributed and further transported to the slope and ocean. The sedimentary processes on the shelf are controlled by waves, tides, storm events and tectonics and are also impacted by the industrial activities mentioned above. In particular excessive bottom trawling causes considerable sediment resuspension (Oberle et al. 2016a,b).

Near-surface coastal and shelf sediments provide a natural archive of sedimentary history preserving information on the past and present transport, erosion, and depo-

sitional processes. Geophysical exploration methods play an important role in recovering this geological information enabling to understand the influence of the seafloor on the marine environment, the protection of the seafloor and the sustainable use of its resources.

Seismic and acoustic methods provide bathymetric and stratigraphic information and are widely used for seabed characterisation but are limited in quantitative determination of texture, porosity, mineralogy and other non-acoustic physical or chemical sediment properties. In contrast, grab samples and cores are still the predominant method of obtaining quantitative sediment information. These measurements are time-consuming, expensive and only available at isolated point positions. Therefore, employing other methodologies providing quantitative estimates of the seafloor sediments over large areas is needful. Controlled-source electromagnetic (CSEM) systems are promising methods to quantify the seafloor electric conductivity (e.g. Cheesman et al. 1993; Evans 2001) and magnetic susceptibility (Müller et al. 2012); both can be linked to textural and chemical properties of the seafloor substrata. Electromagnetic (EM) imaging has therefore the potential to be a decisive geophysical method for coastal zone management, mineral exploration, seafloor contamination and sediment provenance studies in worldwide continental shelf systems. However, the development of new statistical tools for geophysical data processing and analysis remains an important task to close the gap between sediment sampling and remote seafloor characterisation.

1.1 Marine electromagnetic imaging

EM methods are routinely employed on land to study the EM properties of the earth interior. Their applications on land are manifold including deep mantle investigations, exploration of natural resources such as petroleum, mineral deposits, geothermal energy and groundwater. They are also applied in engineering and environmental geophysics to localise and dimension waste disposals, to find buried metallic objects such as land mines and unexploded ordnance, and to investigate hydrological features. Another field of application is archaeology where man-made structures can be localised based on their different EM properties compared to the surrounding sediments.

The variety of EM methods, survey configurations, processing and interpretation procedures is as large as their range of applications. However, all techniques commonly employ one or several receivers to sense the electric and/or magnetic fields

which originate from an EM source and have been altered by the subsurface EM properties.

EM techniques can be divided into two classes based on the sources employed, which are either passive or active (controlled) sources. The most common passive source technique uses natural variations in the Earth's magnetic field that induce electric currents and fields in the ground and is therefore called magnetotelluric (MT) method (Vozoff 1991). Controlled-source EM (CSEM) methods use an artificial source field excited by either magnetic coils or grounded electric wires. The induced electric and/or magnetic fields are measured as a function of frequency or decay time and source-receiver geometry.

Initially, the application of EM methods in the ocean was thought to be impossible. It was assumed that the seawater is too conductive to let a detectable amount of the EM field penetrate into the seafloor (Chave et al. 1991). The modification of EM methods for sea-floor measurements has never been straightforward due to difficulties in building and operating the necessary instruments for a high pressure and corrosive environment (Constable 2013).

The first seafloor application of the MT methods was carried out in the 1960s (Filloux 1967). The limited sensitivity of the first MT methods to shallow structures led to the development of a CSEM method for the deep seafloor (C. Cox 1980). An EM transmitter towed close to the seafloor replaced the MT source allowing to map shallower structures (Fig. 1.1). Sinha et al. (1990) developed a similar system. Both systems were used to study the oceanic lower crust/upper mantle (Constable and C. S. Cox 1996; C. S. Cox et al. 1986) and mid-ocean ridge systems (Evans et al. 1991; Sinha et al. 1997).

In the last decade CSEM methods had become recognised by the oil and gas industry as a complementary exploration tool following a successful CSEM survey over a known oil reservoir offshore Angola (Eidesmo et al. 2002; Ellingsrud et al. 2002). Subsequently, the CSEM method was quickly commercialised and within the first ten years over 500 surveys reportedly having been carried out (Constable 2010). CSEM hydrocarbon exploration is well documented throughout the literature and introductions are given in Constable and Weiss (2006), Constable and Srnka (2007), and Um and Alumbaugh (2007). The basic idea is that the vertical eddy currents created by the CSEM transmitters are affected by thin resistive layers i.e. the hydrocarbon reservoirs, causing a detectable increase in the measured EM field (Key 2012). All methods described above have been designed to investigate deeper targets several hundred to several thousand meters below the seafloor.

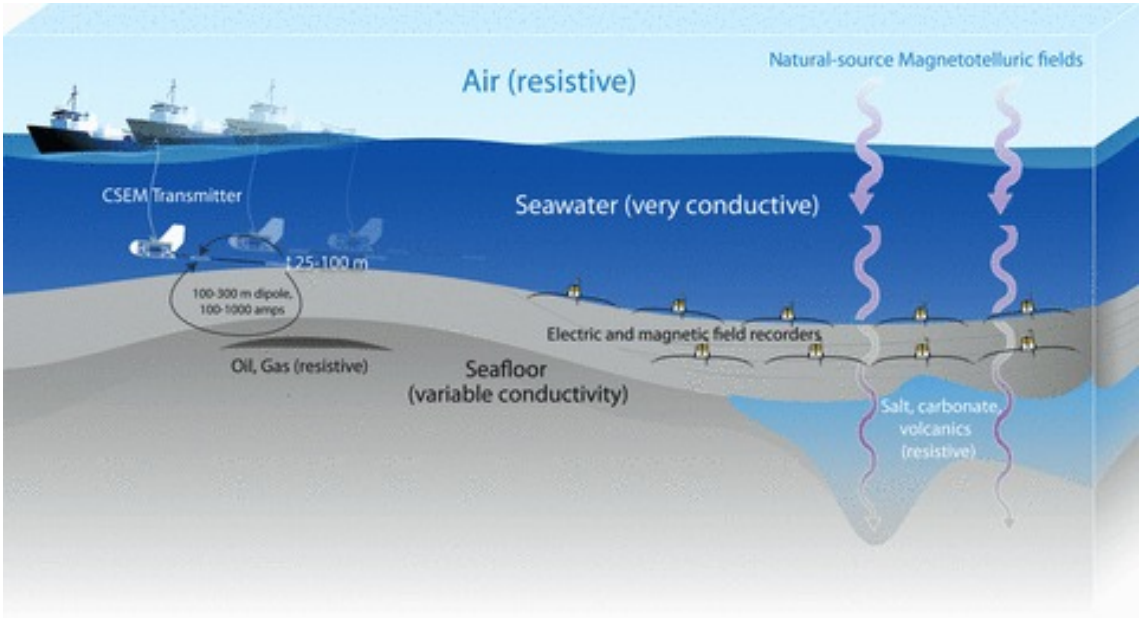

Figure 1.1: Illustration of marine MT and CSEM concepts (Constable 2013). The MT sea-floor receivers record time series of the Earth's varying magnetic field and the related electric field sensitive to deeper geological objects. Towing a CSEM transmitter close to the seafloor enables to map shallower, thin resistive targets (e.g. hydrocarbon reservoirs) using the same receivers.

The interest in marine near-surface EM mapping came up with the first discovery of polymetallic sulphide deposits and the corresponding possibility of deep-sea mining (Chave et al. 1991). To map shallow structures short source-receiver spacing of a few tens of meters or less is necessary which can best be achieved by towing or dragging both the transmitter and the receivers. This kind of survey mode also enables a continuous data collection and real-time data analysis. Cheesman et al. (1987) investigated different possible configurations for a bottom-towed transient seafloor EM system trying to produce a tool equivalent to the well-established airborne EM methods in mineral exploration on land. Based on these studies Cheesman et al. (1990) developed a horizontal, coaxial magnetic dipole-dipole system, one of the first marine EM systems to map the near-surface electric conductivity of the seafloor. This system was successively refined and used to measure the shallow porosity structure within the top 20 m of continental shelves (Cheesman et al. 1990; Evans et al. 1999; Evans 2001; Evans 2007), seafloor mounds (Ellis et al. 2008) and to measure the conductivity of the Kane Oceanic Core Complex (Evans et al. 2010). A similar towed dipole-dipole system was built at the University of Toronto (Fig. 1.2, Yuan and Edwards 2000) with the difference that it uses electric transmitters and receivers and operates in the

time domain. This system was successfully employed to assess marine gas hydrates down to depth of a few hundred meters below the seafloor (Schwalenberg et al. 2005; Schwalenberg et al. 2010a,b; Yuan and Edwards 2000).

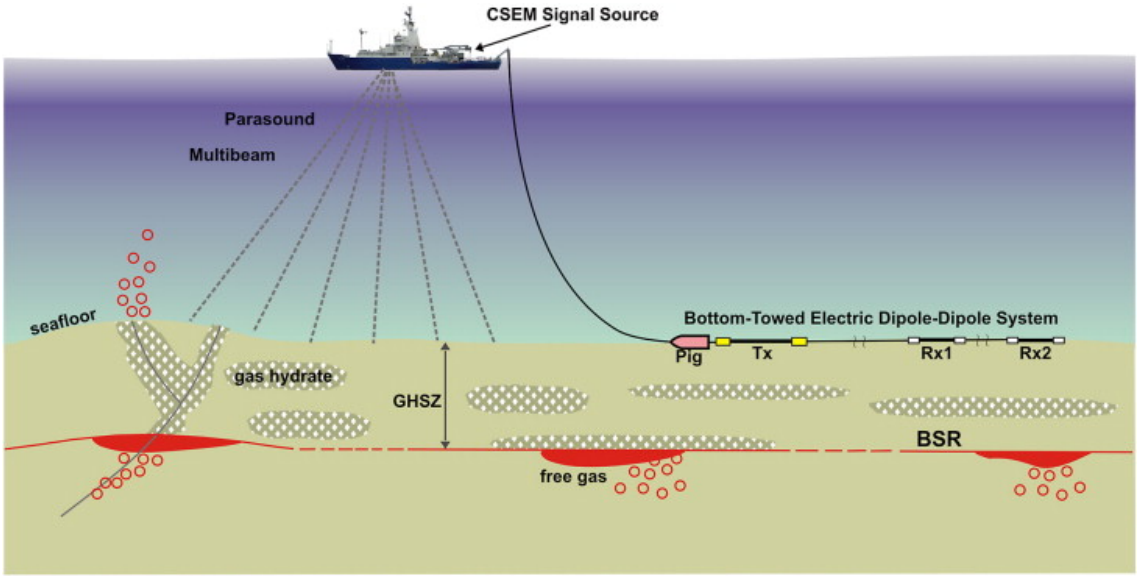

Figure 1.2: Concept of the inline dipole-dipole CSEM system by Schwalenberg et al. (2010a). The two receivers Rx1 and Rx2 are towed on the seafloor behind the transmitter. The source signal is generated on the ship and sent down via a coaxial cable to the Tx dipole. The receivers measure the EM earth response dependent on the seafloor conductivity structure. The different source-receiver spacings make the two receivers sensitive to different depths.

A more compact marine CSEM system was developed by Müller et al. (2012) with the goal to provide a tool capable of measuring both, the electric conductivity and the magnetic susceptibility with significantly better sensitivity and resolution than potential-field methods. They modified a commercial frequency domain, concentric, coplanar CSEM sensor (GEM-3, Won et al. 1997) initially designed for near-surface geophysical investigations on land. This system was successfully employed to investigate freshwater seepage in the Baltic Sea (Müller et al. 2011) and the distribution of surficial sediments on the NW Iberian shelf (Müller et al. 2012). After the loss of this system in 2009 on research cruise M78/3a, 'NERIDIS III', a new modular multi-sensor benthic profiler, was developed at MARUM - Center for Marine Environmental Sciences and Faculty of Geosciences at the University of Bremen. The development of this system has provided the technical basis of the research presented here. The NERIDIS III profiler is introduced in chapter 2 (Baasch et al. 2015) and was employed for acquisition of the EM data used in this thesis.

1.1.1 Electric conductivity of marine surficial sediments

Electric conductivity shows the greatest variation of all physical rock and mineral properties. It ranges from 10^{-7} S/m for close grained rocks to 10^{5} S/m of some metallic minerals (Telford et al. 1990). However, the electric conductivity of the topmost seafloor sediments is generally dominated by the presence of seawater in pores and interstices (Evans 2007). This is because the electric conductivity of seawater is normally several orders of magnitude higher than that of the sediment grains. As a result the sediments act as electrolytic conductors. Due to this relation electric conductivity has been interpreted in terms of porosity in many studies (e.g. Cheesman et al. 1993; Ellis et al. 2008; Evans et al. 1999; Evans et al. 2000; Evans 2001; Jackson et al. 1978; Müller et al. 2011, 2012). Most commonly porosity is derived from conductivity using Archie's law (Archie 1942) given by

$$\sigma_s = \frac{1}{a}\sigma_w \Phi^m S^n \ , \tag{1.1}$$

where σ_s and σ_w are the electric bulk conductivity of the sediment and the water conductivity, respectively, Φ is the porosity and S the degree of saturation. The dimensionless tortuosity factor a, the cementation exponent m and the saturation exponent n are material constants and empirically derived. For shallow marine sediments it can normally be assumed that all pore space is filled with water such that $S = 1$. The porosity of unconsolidated clastic sediment is mainly controlled by grain size, shape and packing, which therefore also influence the electric conductivity. In general, porosity and hence electric conductivity is decreasing with increasing grain-size. Natural sedimentary processes of sand-size grains are controlled by gravity forming structures, such as those in Fig 1.3 a-c where larger grains are usually in direct contact (Hamilton 1970). In contrast, fine silt and clay-sized particles form 'card house' structures (Fig. 1.3 d-f) controlled by interparticle forces. This highly tortuous networks formed by clay particles result in high porosity of up to over 70 per cent enabling the identification of clayey and silty sediments by means of electric conductivity measurements. In contrast, the porosity of sandy sediments is almost entirely controlled by the degree of sorting (Beard and Weyl 1973). Well sorted sands have usually a higher porosity than poorly sorted sands. However, the influence of sorting on electric conductivity is less well understood (Evans 2007). Compaction, consolidation and diagenesis, generally lead to a decrease in porosity. The elimination of interconnected pore space has a huge impact on electric conductivity due to a reduction of ionic conduction paths for the propagation of currents. For highly

compacted sediments the conductivity of the matrix becomes relevant which further complicates the conduction porosity relationship. The interrelated effects of the above factors make the conductivity based quantification of one of these factors difficult and the incorporation of complementary information might be necessary.

1.1.2 Magnetic susceptibility of marine surficial sediments

Magnetic susceptibility is defined as the ratio between an induced magnetisation and an inducing magnetic field. It indicates the bulk sediment magnetic mineral content and is therefore sensitive to the abundance and type of iron-bearing minerals. Ferrimagnetic minerals, such as magnetite, maghemite, titano-magnetite, pyrrhotite, and greigite are the minerals with the highest magnetic susceptibility. Antiferromagnetic minerals such as hematite and goethite and paramagnetic minerals such as ilmenite, olivine and pyrite are less magnetic but also have a considerable influence on bulk magnetic properties. Because magnetic minerals mainly originate from eroded igneous and metamorphic rocks, magnetic susceptibility is generally considered as a proxy for the detrital terrigenous component of marine sediments (Ellwood et al. 2000). As a result magnetic properties have been employed in a variety of studies to investigate the processes controlling the terrigenous sediment supply such as sea-level variation and eustacy (Crick et al. 2001; Zhang et al. 2000), climatic variation (Arai et al. 1997; Party 1995), atmospheric dust (Hladil et al. 2006; Razik et al. 2014) and volcanic eruptions (Somayajulu et al. 1978). Magnetic susceptibility has also been used to investigate sources and sinks of magnetic grains (Andrews and Stravers 1993; Bloemendal et al. 1992, 1993; Ellwood et al. 2006; Razik et al. 2014), to identify sediment flow pathways (Sachs and Ellwood 1988) and the related sediment-, morpho- and hydrodynamic conditions (Badesab et al. 2012; Kulgemeyer et al. 2016). Furthermore, variation of magnetic concentration in marine sediments can be caused by diagenesis through mineralogical transformations, dissolution, authigenesis and biomineralisation (Kawamura et al. 2012; Mohamed et al. 2010; Odin and Lamboy 1988; Petersen et al. 1986). Due to the normally small grain size of terrigenous magnetic minerals, susceptibility has been used as a particle size proxy (Booth et al. 2005; Hatfield and Maher 2009; Müller et al. 2012).

The sensitivity to a variety of sediment processes and properties makes magnetic susceptibility measurements an attractive tool for sediment characterisation. As for electric conductivity, the interaction of different factors impacting the magnetic susceptibility (e.g. mineralogy, grain-size, source, transport and climate signatures)

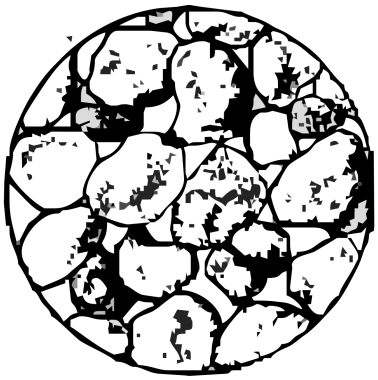

(a)
Single-grained structure

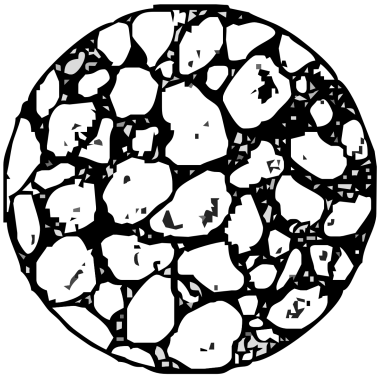

(b)
Mixed-grained structure

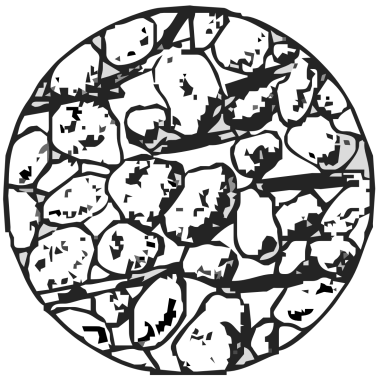

(c)
Bridging effect of platy minerals

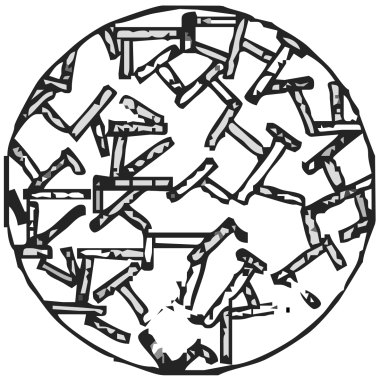

(d)
Card-house structure marine clay

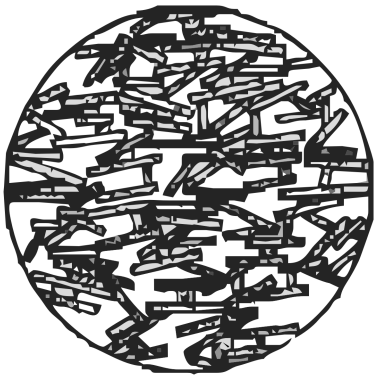

(e)
Card-house structure fresh
water clay (dispersed)

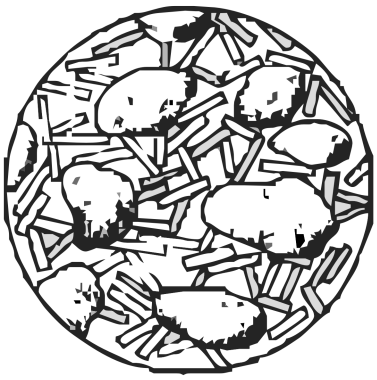

(f)
Card-house structure marine
silty clay

Figure 1.3: Different sediment structures, modified from Hamilton (1970).

makes the identification of a relation to a particular sediment property non-trivial and additional information may be required for a reliable interpretation.

1.2 Motivation and main objectives

This thesis is part of MARUM Research Area SD which investigates seafloor dynamic processes between the coast, shelves and continental slopes. On the pathway from the estuaries to the ocean sediments are subjected to various physical and biogeochemical processes which lead to the deposition, concentration, alteration and resuspension of the sediments. These processes are controlled by tides, currents, waves, storms and anthropogenic influences. The understanding of the driving forces and the interactions of these processes is a key aspect of MARUM Research Area SD.

The study area of the research presented in this thesis is the NW Iberian shelf representing a non-glaciated clastic shelf system. Although the NW Iberian shelf has been investigated for several years and the main sedimentary structures are therefore well described, many open questions remain on the sediment dynamics in this area. In particular, the sediment transport from shelf to slope with the shelf break zone as critical interface is still unsolved. Another important question is how internal processes such as production, transport, preservation and remobilisation of sediments affect accumulation conditions and contribute to sedimentation patterns.

This thesis aims to contribute to answer these questions providing a more detailed representation and deeper insight in the lateral and internal structure of the sediment systems on local scale. This will be achieved through quantitative estimation of sedimentary physical properties from in-situ high-resolution EM measurements.

This PhD project was motivated by the successful development and application of a new benthic EM profiling technique at MARUM in cooperation with the University of Vigo MARGO Group (Müller 2009). Müller et al. (2012) showed that bivariate interpretation of the EM properties electric conductivity and magnetic susceptibility has a great potential to differentiate main lithologic units on the NW Iberian shelf. Based on these early results, the following objectives of this thesis were developed:

1. The development of a 1-D inversion methodology for marine EM profiling data to reconstruct vertical conductivity changes representing surficial sediment stratification. The goal is in particular to gain new insights in the internal structure of the Galicia Mud Belt.

2. Evaluation of the potential for EM data to be used for quantitative estimation of textural properties.

3. Predictive modelling of sediment properties (e.g. porosity, grain size) from EM profiling data with the aim to provide quantitative estimates of sediment properties along shelf-wide survey lines.

1.3 Thesis outline and author contributions

The major scientific outcomes of this cumulative thesis are presented in three manuscripts (chapter 2 to 4) which cover the processing, inversion and interpretation of EM profiling data from the NW Iberian shelf, as well as the prediction of grain-size distributions from the EM data. Chapter 2 and 3 originate from the work of several authors and the contribution of each author is detailed below. During this PhD project the author of this thesis contributed to two other research papers (Appendix C and D) which are part of the PhD thesis by Oberle (2015) which quantifies the long-term anthropogenic and natural effects of sediment resuspension on the NW Iberian shelf. The EM data used for the analyses in chapter 2 to 4 were acquired on the Meteor cruise M84/4b with the benthic profiler MARUM - NERIDIS III which is introduced in chapter 2. Benjamin Baasch partly contributed to the design, development and construction of the profiler. However, Tilo von Dobeneck, Hendrik Müller and Christian Hilgenfeldt mainly contributed to the successful development of NERIDIS III. Tilo von Dobeneck and Hendrik Müller alongside the cruise leader Till J.J. Hanebuth were also mainly responsible for planning the EM survey and the sediment sampling campaign during this cruise. During the acquisition of the EM data, the on-board control of the profiler and the live data quality control were carried out by Hendrik Müller, Christian Hilgenfeldt, Benjamin Baasch and Tilo von Dobeneck. The electric conductivity measurements at the sediment samples were carried out by several members of the scientific crew of M84/4b. The sample magnetic susceptibility was measured by Max Kluger. Benjamin Baasch carried out the grain-size measurements and analyses with help from Inka Meyer.

Chapter 2 Inversion of marine multifrequency electromagnetic profiling data: a new approach to resolve surficial sediment stratification. Benjamin Baasch, Hendrik Müller, Ferdinand K.J. Oberle and Tilo von Dobeneck, *Geophysical Journal International*, 2015, 200, pp. 439-451.

This chapter investigates the potential of concentric-loop EM induction methods to recover conductivity and susceptibility of layered marine sediments. Sensitivity analyses to determine the depth of investigation related to electric conductivity and magnetic susceptibility are carried out. Based on these results an inversion approach is developed enabling the reconstruction of vertical conductivity distributions, incorporating half-space magnetic susceptibility and electric conductivity obtained through simultaneously half-space inversion. The inversion algorithms are tested on synthetic and real data acquired on the NW Iberian shelf.

The conception, development and implementation of the presented calibration and inversion methodology are the work of Benjamin Baasch and build the main scientific achievement of this paper. Benjamin Baasch provided the initial draft and created the final version of the paper incorporating the comments of the co-authors. Hendrik Müller, Tilo von Dobeneck and Ferdinand K.J. Oberle contributed to the data interpretation and gave editorial support. Ferdinand K.J. Oberle processed the seismo-acoustic data and image.

Chapter 3 Determination of grain-size characteristics from electromagnetic seabed mapping data: A NW Iberian shelf study. Benjamin Baasch, Hendrik Müller, Tilo von Dobeneck and Ferdinand K.J. Oberle, *submitted to Continental Shelf Research.*

This chapter deals with the correlation of electric conductivity and magnetic susceptibility with grain-size characteristics. Simple and multiple linear regression analyses are carried out to predict mean grain-size, mud content and the standard deviation of the grain-size distribution from conductivity and susceptibility. It is tested how conductivity and susceptibility complement each other in terms of grain-size quantification. This analysis suggests that electric conductivity and magnetic susceptibility obtained from EM profiling data have a high potential for predictive mapping of textural seafloor properties.

Benjamin Baasch developed the idea to quantitatively predict grain-size properties from EM profiling data. Processing of the EM data, grain-size analyses, the correlation and regression analyses which provide the key results of this manuscript are the work of Benjamin Baasch. Benjamin Baasch provided the initial draft and created the final version of the manuscript incorporating the comments of the co-authors. Hendrik Müller, Tilo von Dobeneck and Ferdinand K.J. Oberle contributed to the manuscript through critical discussion on data

representation, statistics, and the structure of the manuscript and gave editorial assistance.

Chapter 4 Predictive modelling of grain size distributions from marine electromagnetic profiling data by Benjamin Baasch, in preparation.

In this work a new methodology is developed to predict grain-size distribution from EM data. The presented methodology is, to the author's knowledge, the first published approach to predict an entire grain-size distribution from geophysical data. Testing and validating of the predicted models reveal high prediction accuracy. The predicted grain-size distributions represent the well-known sediment facies and patterns on the NW Iberian shelf and give new insights into their distribution, transition and dynamics.

At this stage there is no contribution from co-authors to this manuscript.

Appendix C Volumetric budget calculation of sediment and carbon storage and export for a late Holocene mid-shelf mudbelt system (NW Iberia). Ferdinand K.J. Oberle, Till J.J. Hanebuth, Benjamin Baasch, Tilmann Schwenk, *Continental Shelf Research* 2014, 76, 12–24.

Ferdinand K.J. Oberle developed the ideas of this study and carried out data analysis and interpretation and wrote this manuscript. Ferdinand K.J. Oberle processed all data, carried out all analysis and interpretations Till J.J. Hanebuth headed the research cruises. Benjamin Baasch contributed to supplying salt content measurements and temperature measurements and discussed and commented on the paper. Tilmann Schwenk helped with the acoustic data processing.

Appendix D Deciphering the lithological consequences of bottom trawling to sedimentary habitats on the shelf. F. K. Oberle, P. W. Swarzenski, C. M. Reddy, R. K. Nelson, B. Baasch, and T. J. Hanebuth *Journal of Marine Systems*, 159, pp. 120Ű131.

Ferdinand K.J. Oberle developed the ideas of this study and carried out data analysis and interpretation and wrote this manuscript. C. M. Reddy contribute by teaching the GCxGC method and providing help with interpretation of HFO-markers. P. W. Swarzenski helped with ^{210}**Pb** processing and analysis. R. K. Nelson helped with GCxGC injections and runs. Benjamin Baasch provided data on sediment grain size. Till J.J. Hanebuth headed multiple research cruises that collected the core data used in this study. All authors discussed and commented on the paper.

References

Andrews, J. and J. Stravers (1993). "Magnetic susceptibility of late quaternary marine sediments, Frobisher Bay, N.W.T.: An indicator of changes in provenance and processes". In: *Quaternary Science Reviews* 12.3, pp. 157–167. ISSN: 0277-3791. DOI: http://dx.doi.org/10.1016/0277-3791(93)90050-V.

Arai, K., H. Sakai, and K. Konishi (1997). "High-resolution rock-magnetic variability in shallow marine sediment: a sensitive paleoclimatic metronome". In: *Sedimentary Geology* 110.1, pp. 7–23. ISSN: 0037-0738. DOI: http://dx.doi.org/10.1016/S0037-0738(96)00082-6.

Archie, G. (1942). "The electrical resistivity log as an aid in determining some reservoir characteristics". In: *Petroleum Transactions of AIME* 146, pp. 54–62.

Baasch, B., H. Müller, F. K. J. Oberle, and T. von Dobeneck (2015). "Inversion of marine multifrequency electromagnetic profiling data: a new approach to resolve surficial sediment stratification". In: *Geophysical Journal International* 200.1, pp. 438–451. DOI: 10.1093/gji/ggu406.

Badesab, F., T. von Dobeneck, K. R. Bryan, H. Müller, R. M. Briggs, T. Frederichs, and E. Kwoll (2012). "Formation of magnetite-enriched zones in and offshore of a mesotidal estuarine lagoon: An environmental magnetic study of Tauranga Harbour and Bay of Plenty, New Zealand". In: *Geochemistry, Geophysics, Geosystems* 13.6. Q06012. ISSN: 1525-2027. DOI: 10.1029/2012GC004125.

Beard, D. C. and P. K. Weyl (1973). "Influence of Texture on Porosity and Permeability of Unconsolidated Sand". In: *AAPG Bulletin* 57.2, pp. 349–369. ISSN: 0149-1423.

Bloemendal, J., J. W. King, F. R. Hall, and S.-J. Doh (1992). "Rock magnetism of Late Neogene and Pleistocene deep-sea sediments: Relationship to sediment source, diagenetic processes, and sediment lithology". In: *Journal of Geophysical Research: Solid Earth* 97.B4, pp. 4361–4375. ISSN: 2156-2202. DOI: 10.1029/91JB03068.

Bloemendal, J., J. W. King, A. Hunt, P. B. Demenocal, and A. Hayashida (1993). "Origin of the sedimentary magnetic record at Ocean Drilling Program Sites on the Owen Ridge, western Arabian Sea". In: *Journal of Geophysical Research: Solid Earth* 98.B3, pp. 4199–4219. ISSN: 2156-2202. DOI: 10.1029/92JB02914.

Booth, C., J. Walden, A. Neal, and J. Smith (2005). "Use of mineral magnetic concentration data as a particle size proxy: A case study using marine, estuarine and fluvial sediments in the Carmarthen Bay area, South Wales, U.K." In: *Science of The Total Environment* 347.1 - 3, pp. 241–253. ISSN: 0048-9697. DOI: http://dx.doi.org/10.1016/j.scitotenv.2004.12.042.

Chave, A. D., S. C. Constable, and R. N. Edwards (1991). "Electrical Exploration Methods for the Seafloor". In: *Electromagnetic Methods in Applied Geophysics*, pp. 931–966. DOI: 10.1190/1.9781560802686.ch12.

Cheesman, S. J., R. N. Edwards, and A. D. Chave (1987). "On the theory of sea-floor conductivity mapping using transient electromagnetic systems". In: *GEOPHYSICS* 52.2, pp. 204–217. DOI: 10.1190/1.1442296.

Cheesman, S. J., R. N. Edwards, and L. K. Law (1990). "A test of a short-baseline sea-floor transient electromagnetic system". In: *Geophysical Journal International* 103.2, pp. 431–437. ISSN: 0956540X. DOI: 10.1111/j.1365-246X.1990.tb01782.x.

Cheesman, S. J., L. K. Law, and B. S. Louis (1993). "A porosity mapping survey in Hecate Strait using a seafloor electro-magnetic profiling system". In: *Marine Geology* 110.3, pp. 245–256. ISSN: 0025-3227. DOI: http://dx.doi.org/10.1016/0025-3227(93)90087-C.

Constable, S. and C. S. Cox (1996). "Marine controlled-source electromagnetic sounding: 2. The PEGASUS experiment". In: *Journal of Geophysical Research: Solid Earth* 101.B3, pp. 5519–5530. ISSN: 2156-2202. DOI: 10.1029/95JB03738.

Constable, S. and C. J. Weiss (2006). "Mapping thin resistors and hydrocarbons with marine EM methods: Insights from 1D modeling". In: *GEOPHYSICS* 71.2, G43–G51. DOI: 10.1190/1.2187748.

Constable, S. and L. J. Srnka (2007). "An introduction to marine controlled-source electromagnetic methods for hydrocarbon exploration". In: *GEOPHYSICS* 72.2, WA3–WA12. DOI: 10.1190/1.2432483.

Constable, S. (2010). "Ten years of marine CSEM for hydrocarbon exploration". In: *GEOPHYSICS* 75A.5, pp. 67–81. DOI: 10.1190/1.3483451.

– (2013). "Review paper: Instrumentation for marine magnetotelluric and controlled source electromagnetic sounding". In: *Geophysical Prospecting* 61, pp. 505–532. ISSN: 1365-2478. DOI: 10.1111/j.1365-2478.2012.01117.x.

Cox, C. (1980). "Electromagnetic induction in the oceans and inferences on the constitution of the earth". In: *Geophysical surveys* 4.1, pp. 137–156. ISSN: 1573-0956. DOI: 10.1007/BF01452963.

Cox, C. S., S. C. Constable, A. D. Chave, and S. C. Webb (1986). "Controlled-source electromagnetic sounding of the oceanic lithosphere". In: *Nature* 320.6057, pp. 52–54.

Crick, R., B. Ellwood, J. Hladil, A. E. Hassani, F. Hrouda, and I. Chlupác (2001). "Magnetostratigraphy susceptibility of the Pridolian-Lochkovian (Silurian-Devonian) GSSP (Klonk, Czech Republic) and coeval sequence in Anti-Atlas Morocco". In: *Palaeogeography, Palaeoclimatology, Palaeoecology* 167.1-2, pp. 73–100. ISSN: 0031-0182. DOI: http://dx.doi.org/10.1016/S0031-0182(00)00233-9.

Dilley Maxx; Chen, R. S., U. Deichmann, A. L. Lerner-Lam, M. Arnold, J. Agwe, P. Buys, O. Kjevstad, B. Lyon, and G. Yetman (2005). *Natural disaster hotspots: A global risk analysis*. World Bank.

Eidesmo, T., S. Ellingsrud, L. MacGregor, S. Constable, M. Sinha, S. Johansen, F. Kong, and H. Westerdahl (2002). "Sea Bed Logging (SBL), a new method for remote and direct identification of hydrocarbon filled layers in deepwater areas". In: *First Break* 20.3, pp. 144–152.

Ellingsrud, S., T. Eidesmo, S. Johansen, M. C. Sinha, L. M. MacGregor, and S. Constable (2002). "Remote sensing of hydrocarbon layers by seabed logging (SBL): Results from a cruise offshore Angola". In: *The Leading Edge* 21.10, pp. 972–982. DOI: 10.1190/1.1518433.

Ellis, M., R. Evans, D. Hutchinson, P. Hart, J. Gardner, and R. Hagen (2008). "Electromagnetic surveying of seafloor mounds in the northern Gulf of Mexico". In: *Marine and Petroleum Geology* 25.9, pp. 960–968. ISSN: 0264-8172. DOI: http://dx.doi.org/10.1016/j.marpetgeo.2007.12.006.

Ellwood, B. B., R. E. Crick, A. E. Hassani, S. L. Benoist, and R. H. Young (2000). "Magnetosusceptibility event and cyclostratigraphy method applied to marine rocks: Detrital input versus carbonate productivity". In: *Geology* 28.12, pp. 1135–1138. DOI: 10.1130/0091-7613(2000)28<1135:MEACMA>2.0.CO;2.

Ellwood, B. B., W. L. Balsam, and H. H. Roberts (2006). "Gulf of Mexico sediment sources and sediment transport trends from magnetic susceptibility measurements of surface samples". In: *Marine Geology* 230.3-4, pp. 237–248. ISSN: 0025-3227. DOI: http://dx.doi.org/10.1016/j.margeo.2006.05.008.

Evans, R. L., S. C. Constable, M. C. Sinha, C. S. Cox, and M. J. Unsworth (1991). "Upper crustal resistivity structure of the East Pacific Rise near 13° N". In: *Geophysical Research Letters* 18.10, pp. 1917–1920. ISSN: 1944-8007. DOI: 10.1029/91GL02305.

Evans, R. L., L. Law, B. S. Louis, S. Cheesman, and K. Sananikone (1999). "The shallow porosity structure of the Eel shelf, northern California: results of a towed electromagnetic survey". In: *Marine Geology* 154.1-4, pp. 211–226. ISSN: 0025-3227. DOI: http://dx.doi.org/10.1016/S0025-3227(98)00114-5.

Evans, R. L., L. Law, B. S. Louis, and S. Cheesman (2000). "Buried paleo-channels on the New Jersey continental margin: channel porosity structures from electromagnetic surveying". In: *Marine Geology* 170.3-4, pp. 381–394. ISSN: 0025-3227. DOI: http://dx.doi.org/10.1016/S0025-3227(00)00081-5.

Evans, R. L. (2001). "Measuring the shallow porosity structure of sediments on the continental shelf: A comparison of an electromagnetic approach with cores and acoustic backscatter". In: *J. geophys. Res.* 106.C11, pp. 27047–27060. ISSN: 0148-0227.

Evans, R. L. (2007). "Using CSEM techniques to map the shallow section of seafloor: From the coastline to the edges of the continental slope". In: *GEOPHYSICS* 72.2, WA105–WA116. DOI: 10.1190/1.2434798.

Evans, R. L., J. Escartín, and M. Cannat (2010). "A short electromagnetic profile across the Kane Oceanic Core Complex". In: *Geophysical Research Letters* 37.15. L15309. ISSN: 1944-8007. DOI: 10.1029/2010GL043813.

FAO (2014). *State of World Fisheries and Aquaculture 2014*. Food & Agriculture Organization of the United Nations (FAO).

Filloux, J. H. (1967). "AN OCEAN BOTTOM, D COMPONENT MAGNETOMETER". In: *GEOPHYSICS* 32.6, pp. 978–987. DOI: 10.1190/1.1439910.

Hamilton, E. L. (1970). "Sound velocity and related properties of marine sediments, North Pacific". In: *Journal of Geophysical Research* 75.23, pp. 4423–4446. ISSN: 2156-2202. DOI: 10.1029/JB075i023p04423.

Harris, P., M. Macmillan-Lawler, J. Rupp, and E. Baker (2014). "Geomorphology of the oceans". In: *Marine Geology* 352. 50th Anniversary Special Issue, pp. 4–24. ISSN: 0025-3227. DOI: http://dx.doi.org/10.1016/j.margeo.2014.01.011.

Hatfield, R. G. and B. A. Maher (2009). "Fingerprinting upland sediment sources: particle size-specific magnetic linkages between soils, lake sediments and suspended sediments". In: *Earth Surface Processes and Landforms* 34.10, pp. 1359–1373. ISSN: 1096-9837. DOI: 10.1002/esp.1824.

Hladil, J., M. Gersl, L. Strnad, J. Frana, A. Langrova, and J. Spisiak (2006). "Stratigraphic variation of complex impurities in platform limestones and possible significance of atmospheric dust: a study with emphasis on gamma-ray spectrometry and magnetic susceptibility outcrop logging (Eifelian-Frasnian, Moravia, Czech Republic)". In: *International Journal of Earth Sciences* 95.4, pp. 703–723. ISSN: 1437-3262. DOI: 10.1007/s00531-005-0052-8.

Jackson, P. D., D. T. Smith, and P. N. Stanford (1978). "Resistivity-porosity-particle shape relationships for marine sands". In: *GEOPHYSICS* 43.6, pp. 1250–1268. DOI: 10.1190/1.1440891.

Kawamura, N., N. Ishikawa, and M. Torii (2012). "Diagenetic alteration of magnetic minerals in Labrador Sea sediments (IODP Sites U1305, U1306, and U1307)". In: *Geochemistry, Geophysics, Geosystems* 13.8. Q08013. ISSN: 1525-2027. DOI: 10.1029/2012GC004213.

Key, K. (2012). "Marine Electromagnetic Studies of Seafloor Resources and Tectonics". In: *Surveys in Geophysics* 33.1, pp. 135–167. ISSN: 1573-0956. DOI: 10.1007/s10712-011-9139-x.

Kulgemeyer, T., T. von Dobeneck, H. Müller, K. Bryan, W. de Lange, and C. N. Battershill (2016). "Magnetic mineral and sediment porosity distribution on a storm-dominated shelf investigated by benthic electromagnetic profiling (Bay of Plenty, New Zealand)". In: *Submitted to Marine Geology*.

McGranahan, G., D. Balk, and B. Anderson (2007). "The rising tide: assessing the risks of climate change and human settlements in low elevation coastal zones". In: *Environment and Urbanization* 19.1, pp. 17–37. DOI: 10.1177/0956247807076960.

Mohamed, K. J., D. Rey, B. Rubio, F. Vilas, and T. Frederichs (2010). "Interplay between detrital and diagenetic processes since the last glacial maximum on the northwest Iberian continental shelf". In: *Quaternary Research* 73.3, pp. 507–520. ISSN: 0033-5894. DOI: http://dx.doi.org/10.1016/j.yqres.2010.02.003.

Müller, H. (2009). "Characterisation of marine near-surface sediments by electromagnetic profiling". PhD thesis. University of Bremen.

Müller, H., T. von Dobeneck, W. Nehmiz, and K. Hamer (2011). "Near-surface electromagnetic, rock magnetic, and geochemical fingerprinting of submarine freshwater seepage at Eckernförde Bay (SW Baltic Sea)". English. In: *Geo-Marine Letters* 31.2, pp. 123–140. ISSN: 0276-0460. DOI: 10.1007/s00367-010-0220-0.

Müller, H., T. von Dobeneck, C. Hilgenfeldt, B. SanFilipo, D. Rey, and B. Rubio (2012). "Mapping the magnetic susceptibility and electric conductivity of marine surficial sediments by benthic EM profiling". In: *Geophysics* 77.1, E43–E56. ISSN: 0016-8033. DOI: 10.1190/geo2010-0129.1.

Oberle, F. K. (2015). "Quantifying the long-term anthropogenic and natural effects of sediment resuspension on the NW Iberian shelf". PhD thesis. University of Bremen.

Oberle, F. K., P. W. Swarzenski, C. M. Reddy, R. K. Nelson, B. Baasch, and T. J. Hanebuth (2016a). "Deciphering the lithological consequences of bottom trawling to sedimentary habitats on the shelf". In: *Journal of Marine Systems* 159, pp. 120–131. ISSN: 0924-7963. DOI: http://dx.doi.org/10.1016/j.jmarsys.2015.12.008.

Oberle, F. K., C. D. Storlazzi, and T. J. Hanebuth (2016b). "What a drag: Quantifying the global impact of chronic bottom trawling on continental shelf sediment". In: *Journal of Marine Systems* 159, pp. 109–119. ISSN: 0924-7963. DOI: http://dx.doi.org/10.1016/j.jmarsys.2015.12.007.

Odin, G. and M. Lamboy (1988). "Glaucony From The Margin off Northwestern Spain". In: *Green Marine Clays*. Ed. by G. Odin. Elsevier, pp. 249–275. DOI: http://dx.doi.org/10.1016/S0070-4571(08)70067-0.

Party, L. 1. S. (1995). "Ceara rise sediments document ancient climate change". In: *Eos, Transactions American Geophysical Union* 76.5, pp. 41–45. ISSN: 2324-9250. DOI: 10.1029/EO076i005p00041-02.

Petersen, N., T. von Dobeneck, and H. Vali (1986). "Fossil bacterial magnetite in deep-sea sediments from the South Atlantic Ocean". In: *Nature* 320.6063, pp. 611–615.

Razik, S., M. J. Dekkers, and T. von Dobeneck (2014). "How environmental magnetism can enhance the interpretational value of grain-size analysis: A time-slice study on sediment export to the NW African margin in Heinrich Stadial 1 and Mid Holocene". In: *Palaeogeography, Palaeoclimatology, Palaeoecology* 406, pp. 33–48. ISSN: 0031-0182. DOI: http://dx.doi.org/10.1016/j.palaeo.2014.04.009.

Sachs, S. D. and B. B. Ellwood (1988). "Controls on magnetic grain-size variations and concentration in the Argentine Basin, South Atlantic Ocean". In: *Deep Sea Research Part A. Oceanographic Research Papers* 35.6, pp. 929–942. ISSN: 0198-0149. DOI: http://dx.doi.org/10.1016/0198-0149(88)90069-6.

Schwalenberg, K., E. Willoughby, R. Mir, and R. Edwards (2005). "Marine gas hydrate electromagnetic signatures in Cascadia and their correlation with seismic blank zones". In: *First Break* 23.4, pp. 57–63.

Schwalenberg, K., M. Haeckel, J. Poort, and M. Jegen (2010a). "Evaluation of gas hydrate deposits in an active seep area using marine controlled source electromagnetics: Results from Opouawe Bank, Hikurangi Margin, New Zealand". In: *Marine Geology* 272.1-4, pp. 79–88. ISSN: 0025-3227. DOI: http://dx.doi.org/10.1016/j.margeo.2009.07.006.

Schwalenberg, K., W. Wood, I. Pecher, L. Hamdan, S. Henrys, M. Jegen, and R. Coffin (2010b). "Preliminary interpretation of electromagnetic, heat flow, seismic, and geochemical data for gas hydrate distribution across the Porangahau Ridge, New Zealand". In: *Marine Geology* 272.1-4, pp. 89–98. ISSN: 0025-3227. DOI: http://dx.doi.org/10.1016/j.margeo.2009.10.024.

Shepard, F. (1963). *Submarine Geology*. New York: Harper and Row, p. 557.

Sinha, M. C., P. D. Patel, M. J. Unsworth, T. R. E. Owen, and M. R. G. Maccormack (1990). "An active source electromagnetic sounding system for marine use". In: *Marine Geophysical Researches* 12.1, pp. 59–68. ISSN: 1573-0581. DOI: 10.1007/BF00310563.

Sinha, M. C., D. A. Navin, L. M. MacGregor, S. Constable, C. Peirce, A. White, G. Heinson, and M. A. Inglis (1997). "Evidence for accumulated melt beneath the slow–spreading

Mid–Atlantic Ridge". In: *Philosophical Transactions of the Royal Society of London A: Mathematical, Physical and Engineering Sciences* 355.1723, pp. 233–253. ISSN: 1364-503X. DOI: 10.1098/rsta.1997.0008.

Somayajulu, B. L. K., C. Radhakrishnamurty, and T. J. Walsh (1978). "Susceptibility as a tool for studying magnetic stratigraphy of marine sediments". In: *Proceedings of the Indian Academy of Sciences - Section A, Earth and Planetary Sciences* 87.11, pp. 201–213. ISSN: 0370-0089. DOI: 10.1007/BF02861514.

Telford, W. M., L. P. Geldart, and R. E. Sheriff (1990). "Electrical Properties of Rocks and Minerals". In: *Applied Geophysics*. Second. Cambridge Books Online. Cambridge University Press, pp. 283–292. ISBN: 9781139167932.

Um, E. S. and D. L. Alumbaugh (2007). "On the physics of the marine controlled-source electromagnetic method". In: *GEOPHYSICS* 72.2, WA13–WA26. DOI: 10.1190/1.2432482.

Vozoff, K. (1991). "The Magnetotelluric Method". In: *Electromagnetic Methods in Applied Geophysics*, pp. 641–712. DOI: 10.1190/1.9781560802686.ch8.

Won, I., D. Keiswetter, D. Hanson, E. Novikova, and T. Hall (1997). "GEM-3: A Monostatic Broadband Electromagnetic Induction Sensor". In: *Journal of Environmental and Engineering Geophysics* 2.1, pp. 53–64. DOI: 10.4133/JEEG2.1.53.

Yuan, J. and R. N. Edwards (2000). "The Assessment of Marine Gas Hydrates Through Electrical Remote Sounding: Hydrate Without a BSR?" In: *Geophysical Research Letters* 27.16, pp. 2397–2400. ISSN: 1944-8007. DOI: 10.1029/2000GL011585.

Zhang, S., X. Wang, and H. Zhu (2000). "Magnetic susceptibility variations of carbonates controlled by sea-level changes". In: *Science in China Series D: Earth Sciences* 43.3, pp. 266–276. ISSN: 1862-2801. DOI: 10.1007/BF02906822.

Chapter 2

Inversion of marine multifrequency electromagnetic profiling data: a new approach to resolve surficial sediment stratification

Geophysical Journal International

Geophys. J. Int. (2015) **200,** 439–451
GJI Marine geosciences and applied geophysics

doi: 10.1093/gji/ggu406

Inversion of marine multifrequency electromagnetic profiling data: a new approach to resolve surficial sediment stratification

B. Baasch,* H. Müller, F. K. J. Oberle and T. von Dobeneck

MARUM – Center for Marine Environmental Sciences and Faculty of Geosciences, University of Bremen, Germany. E-mail: baasch@uni-bremen.de

Accepted 2014 October 16. Received 2014 October 15; in original form 2014 February 27

SUMMARY

Electromagnetic induction (EMI) methods are widely used on land to map electric conductivity and/or magnetic susceptibility distributions of surficial sediments. In contrast, the application of these methods in marine environments is relatively novel. Based on the recently developed electromagnetic benthic profiler MARUM-NERIDIS III we investigate the potential of concentric-loop EMI methods to recover conductivity and susceptibility of layered marine sediments. Sensitivity analyses based on a data and model normalized Jacobian matrix were performed to compare the influence of conductivity and susceptibility to in-phase and quadrature components at different frequencies. Both parameters substantially affect the EM response. However, the influence of susceptibility decreases more with depth and offers lower depth resolution than that of conductivity. A 1-D inversion algorithm to reconstruct vertical conductivity distributions was developed from existing non-linear inversion methods using apparent conductivity and apparent susceptibility recovered from simultaneous half-space inversion as *a priori* information. This algorithm was tested on synthetic and real marine EM data from a commercial multifrequency concentric loop EMI system (GEM-3). The results indicate that our inversion algorithm yields meaningful results down to approximately 3 m depth under typical shallow marine conditions. The comparison of inversion results recovered with 1-D and 2-D constraints showed that combining lateral with vertical constraints substantially improves the resolution of the inversion outputs. Field data from the NW Iberian shelf was calibrated according to a processing flow specifically designed for underwater conditions and analysed. Inversion outputs are in good agreement with ground-truthing stratigraphic investigations and deliver relevant clues on past and present sediment dynamics.

Key words: Inverse theory; Electromagnetic theory; Magnetic and electrical properties; Marine electromagnetics.

1 INTRODUCTION

As critical interface between land and ocean, coastal and shelf areas play an important role in the chain of marine sedimentary processes. These are not only of high scientific interest, but increasingly relevant for infrastructural offshore projects such as wind farms, pipeline and power cable routes as well as for exploitation of marine mineral resources.

Acoustic surveys offer fast high-resolution imaging of seabed sediment distributions but are limited in quantitative analysis of sedimentological parameters. An alternative approach to assess the distribution and stratification of coastal and shelf sediments is controlled-source electromagnetics (CSEM). Cheesman *et al.* (1990) developed a towed transient electromagnetic system to map the near-surface electrical conductivity of the seafloor. Swidinsky *et al.* (2012) investigated the capability of central loop transient electromagnetic methods to map seafloor ore deposits. In this paper, we focus on a novel approach using multifrequency concentric loop electromagnetic induction (CLEM) sensors (Müller *et al.* 2012). CLEM sensors are characterized by horizontally oriented co-axial coplanar transmitter and receiver loops. To enable the receiver of these systems to measure a weak secondary magnetic field in the presence of the high primary magnetic field of the collocated transmitter, an adequate bucking scheme is needed (Won 2003). An appropriate source cancellation can be achieved by employing a third coil which compensates the primary field at the centre of the sensor, so that the receiver does not 'see' the primary field (Won *et al.* 1997). The zero-offset between transmitter and receiver coil together with the wide bandwidth, typically between a few Hertz and several ten thousand Hertz, makes these systems sensitive not only to changes in electric conductivity but also in magnetic susceptibility. Both are standard parameters in marine environmental research. Electric conductivity is related to the pore fluid and mostly interpreted in terms of sediment porosity (Boyce 1968; Evans 2001; Müller *et al.* 2012), bulk density (Boyce 1968) or pore-water

*Now at: PGS Exploration (UK) Limited, Weybridge, Surrey, UK.

salinity (Müller *et al.* 2011). Magnetic susceptibility depends on the mineralogy of the sediment and reflects the content of magnetic minerals which is characteristic of, for example, source, age and/or grain size of the sediment.

Electromagnetic induction (EMI) methods with small constant or zero offset have been almost exclusively applied on land (Butler 2009). For near surface investigations two main sensor types have established themselves: Small-loop EMI (SLEM) sensors are, as the name implies, small, usually portable systems. Their applications range from classical hydrological problems, such as groundwater distribution and contamination (Carcione *et al.* 2003; Martinelli & Duplaá 2008), to archaeological prospecting (Bongiovanni *et al.* 2008) and unexploded ordnance (UXO) detection (Huang & Won 2003). The much larger helicopter EM (HEM) systems are applied in mineral exploration (Huang & Fraser 2003) and groundwater surveys (Auken *et al.* 2006; Juhl Tølbøll & Bøie Christensen 2006).

The first sedimentological applications of CLEM systems in coastal and shelf research by Müller *et al.* (2011, 2012) demonstrated that a multifrequency CLEM sensor towed at constant distance above the seafloor is very efficient in measuring the electric conductivity and magnetic susceptibility of the shallow seabed.

For quantitative interpretation of CLEM data a very stable and precise sensor calibration is needed. CLEM systems working with a source cancellation scheme are very sensitive to calibration errors (Won 2003; Ley-Cooper & Macnae 2007; Sasaki *et al.* 2008). Incomplete bucking of the primary field leads to systematic offset errors, which can strongly affect inverse solutions and compromise the accurate reconstruction of physical properties. While random noise can be removed by means of classical filter strategies such as spatial low-pass filtering or principal component analysis filtering (Minsley *et al.* 2012), systematic errors need an instrument specific handling. For measurements on land, the primary EM field equals the static EM field in air. Offset errors can be determined through free space measurements far enough away from conductive and magnetic objects. One practical way to achieve this is to hang the sensor from the top of a tall tree (Won 2003). Mitsuhata & Imasato (2009) proposed a procedure for on-site correction of bias noise for calibrating GEM-2 instruments. Gain factors can be obtained from calibration measurements using loops of wire or ferrite cores (Scott 2011). In contrast, the calibration of marine EM data must consider that the EM sensor is located in a highly conductive medium. The offset errors depend on sea water conductivity and change with local temperature and salinity. In this paper, we develop a calibration algorithm taking sea water conductivity into account.

Another challenge of inverting marine as well as land CLEM data is that most data is equally affected by magnetic susceptibility and electric conductivity. Inverting for just one of the two parameters is not only a waste of information but also leads to inaccurate reconstruction of the other parameter (Zhang & Oldenburg 1999). Müller *et al.* (2012) developed a forward solution for double and layered half-space models of marine multifrequency CSEM data. A look-up table method was used to recover apparent half-space magnetic susceptibility from a low-frequency in-phase component and subsequently determine electric conductivity from a high-frequency quadrature component. They showed that this method offers meaningful results for marine CLEM data. One can find other sequential half-space inversion techniques in literature such as a method described by Huang & Won (2000) requiring that the sensor operates at sufficiently low frequencies so that the conductivity–frequency product is small. At this 'resistive limit' the sensor measures only susceptibility (Won & Huang 2004). If such low frequencies are not available due to hardware limitations or ambient noise, or if the subsurface susceptibility is very low in relation to the conductivity, this method is likely to fail. Following the approach of Beard & Nyquist (1998), we use a method incorporating the in-phase and quadrature components of all frequencies to invert simultaneously for conductivity and susceptibility.

The assumption of a homogeneous half-space is not valid, where strong porosity gradients can be expected in the uppermost sediments, as is often the case in coastal environments. Müller *et al.* (2012) stated that the potential of marine near surface EM methods were much better exploited by taking the step from half-space to 1-D models. Simultaneous 1-D inversion algorithms to reconstruct susceptibility and conductivity from EM data already exist; fundamental work has been carried out by Zhang & Oldenburg (1999) and Farquharson *et al.* (2003), who used a multilayer inversion approach minimizing the data misfit together with measures of the structure in the conductivity and susceptibility models. Huang & Fraser (2003) developed an algorithm inverting EM data for resistivity, magnetic permeability, and thickness of a layered model. All of these algorithms have been developed for HEM data. By contrast, Sasaki *et al.* (2010) stated that their multidimensional simultaneous inversion is unstable for SLEM data from a single height. To our knowledge no such methods have been applied to marine data sets so far. Here we investigate the potential of the marine CLEM method to recover vertical susceptibility and conductivity distributions and determine the depth of investigation (DOI) for both parameters through sensitivity analyses. Based on these results we introduce a 1-D inversion algorithm with vertical and lateral constraints to reconstruct pseudo 2-D distributions of sediment electric conductivity. This algorithm incorporates apparent susceptibility information derived through half-space inversion, which makes the inversion additionally applicable to a magnetic seafloor. We test our algorithms on synthetic data and field data from the NW Iberian shelf. These real data are also used to test a newly developed calibration technique which is presented as well. All analyses in this paper refer to the recently developed MARUM-NERIDIS III system which is introduced in Section 6.1. However, these analyses are also fully scalable to other marine or land-based CLEM sensors.

2 FORWARD PROBLEM

The sensor output of CLEM systems is usually the receiver coil voltage induced by the secondary magnetic field normalized against the voltage induced by the primary magnetic field. This complex value U is expressed in parts per million (ppm). For forward modelling we use the formula developed by Müller *et al.* (2012) based on an EM field solution of a loop-source over a layered Earth given by (Ward & Hohmann 1988, p. 219). For the configuration shown in Fig. 1, where a CLEM sensor is located in a conductive, diamagnetic half-space (the sea water) at a constant height h_w over a layered conducive and magnetic half-space (the seafloor), the sensor response reads

$$U = \frac{2R_t^2}{R_r}\int_0^\infty r_{TE}\, e^{-2u_w h_w}\frac{\lambda}{u_w} J_1(\lambda R_t)\, J_1(\lambda R_r)\, d\lambda, \quad (1)$$

where R_t is the radius of the transmitter coil, R_r is the radius of the receiver coil, J_1 is the Bessel function of first kind and order and λ is the Hankel transformation parameter. The reflection coefficient r_{TE} in eq. (1) can be expressed as

$$r_{TE} = \frac{Y_w - \hat{Y}_1}{Y_w + \hat{Y}_1}, \quad (2)$$

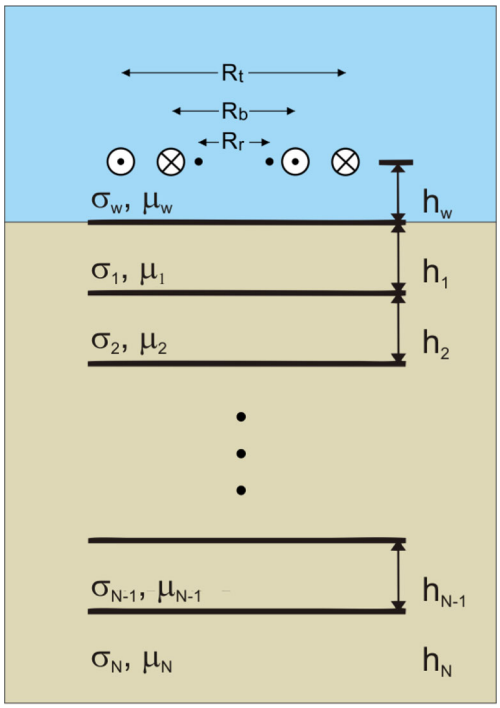

Figure 1. Vertical cross section of a GEM-3 system with transmitter coil radius R_t, bucking coil radius R_b and receiver coil radius R_r located in the water column over a layered Earth.

where $Y_w = u_w/i\omega\mu_w$ is the intrinsic admittance of the sea water and $\hat{Y}_1$ is the surface admittance. Furthermore, $u_w = \sqrt{\lambda^2 + i\omega\mu_w\sigma_w}$, $i = \sqrt{-1}$ and ω is the angular frequency. σ_w and μ_w are the respective electric conductivity and magnetic permeability of the sea water. The magnetic permeability $\mu = \mu_0(1+\kappa)$ is a function of the magnetic susceptibility κ, where μ_0 is the magnetic permeability of free-space.

For a N-layer Earth the surface admittance is given by the recursive series (Ward & Hohmann 1988)

$$\hat{Y}_j = Y_j \frac{\hat{Y}_{j+1} + Y_j \tan h(u_j h_j)}{Y_j + \hat{Y}_{j+1} \tan h(u_j h_j)}, \quad j = 1, 2, \ldots, N-1, \tag{3}$$

with

$$Y_j = \frac{u_j}{i\omega\mu_j}, \tag{4}$$

$$u_j = \sqrt{\lambda^2 + i\omega\mu_j\sigma_j}, \tag{5}$$

where h_j, σ_j, μ_j describe, respectively the thickness, the electric conductivity and the magnetic permeability of the jth layer. Eq. (3) can be solved iteratively starting at the deepest layer N with $\hat{Y}_N = Y_N$.

In the following, our analyses refer to a marinized GEM-3 sensor (Won *et al.* 1997; Müller *et al.* 2012) with three coplanar–coaxial coils: a transmitter, a receiver and a bucking coil with diameters of 0.96, 0.30 and 0.44 m, respectively. Fig. 2 shows the response of this sensor at 0.25 m height above the seafloor according to eq. (1) for a magnetic and non-magnetic sediment with conductivities higher and lower than sea water. Under most aquatic conditions sediment conductivity σ_s is smaller than water conductivity σ_w and in-phase and quadrature values are both negative. Therefore, the in-phase components decrease with increasing frequency over the represented frequency range, while the quadrature components

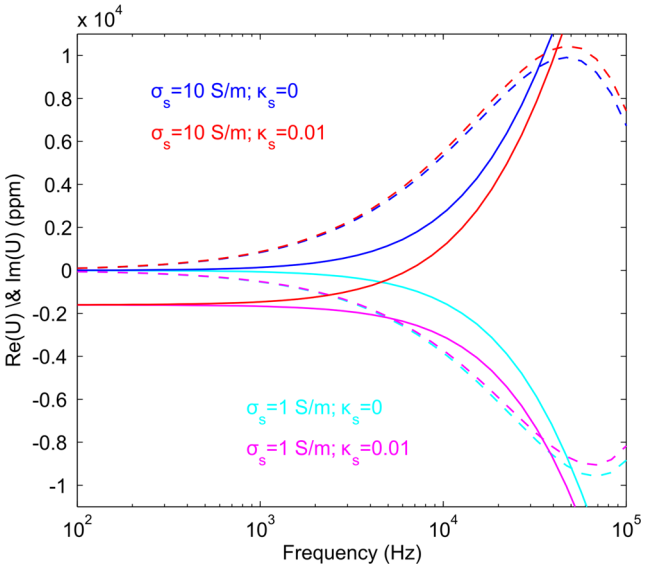

Figure 2. In-phase (solid lines) and quadrature (dashed lines) response of an underwater GEM-3 sensor to a homogeneous half-space versus frequency for different σ_s and κ_s and a water conductivity σ of 4.4 S m^{-1}.

decrease with increasing frequencies up to approximately 50 000 Hz, and then increase. If sediment conductivity is higher than water conductivity, the shape of the response functions is similar to that of measurements on land and opposed to that which was described before, due to the change of sign in eq. (2). In both cases, a magnetic susceptibility above zero causes a negative shift in the in-phase component, whereas the quadrature component is only slightly affected by susceptibility. For small frequencies (<400 Hz) quadrature components converge to zero. In-phase components become independent of conductivity and are almost purely controlled by magnetic susceptibility.

3 SENSITIVITY ANALYSES AND DOI

3.1 Sensitivity analyses

Inversion algorithms based on the linearization of the forward operator need an adequate calculation of the EM field sensitivities. In addition, sensitivity analyses provide clues regarding the capability to reconstruct physical parameters from EM data and can be used to calculate the DOI Christiansen & Auken (2012). The sensitivity (Jacobian) matrix **J** contains the partial derivatives of the data vector with respect to model parameters:

$$J_{ij}(\mathbf{m}) = \frac{\partial d_i(\mathbf{m})}{\partial m_j}, \quad i = 1, 2, \ldots, M, \quad j = 1, 2, \ldots, N, \tag{6}$$

where **d** is the data vector of length M containing the in-phase and quadrature values for each frequency and **m** is the model vector of length N containing the model parameters. Analytical calculations of **J** should be favoured over numerical solutions due to the comparatively higher computational speed and superior accuracy. From eq. (1) it can be seen that the partial derivatives with respect to the model parameters only apply to the term r_{TE}. Thus, the sensitivities can be calculated from eqs (2) to (5). The derivatives of the recursive series in eq. (3) are found by applying the chain rule.

To compare the sensitivities of multifrequency data for conductivity and susceptibility we convert **J** into a model and data independent sensitivity matrix. Christiansen & Auken (2012) suggested

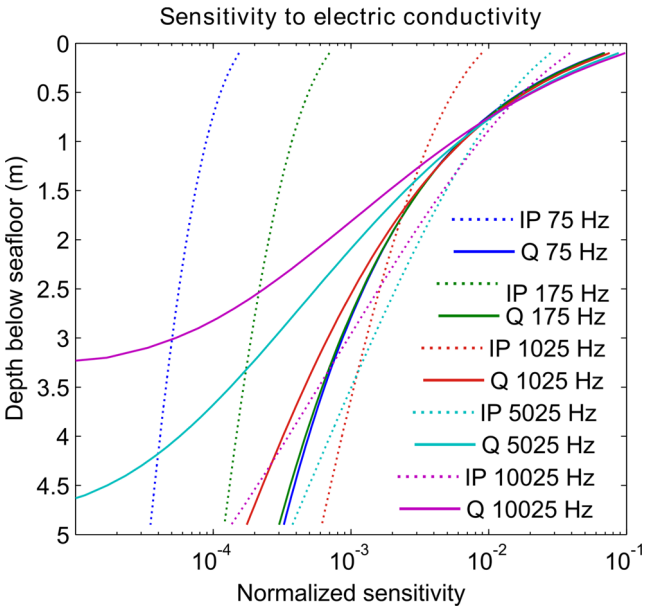

Figure 3. Sensitivities to conductivity at 75, 175, 1025, 5025 and 10 025 Hz. Solid lines mark sensitivities of in-phase (IP) and dashed lines indicate sensitivities of quadrature (Q) components of the sensor response.

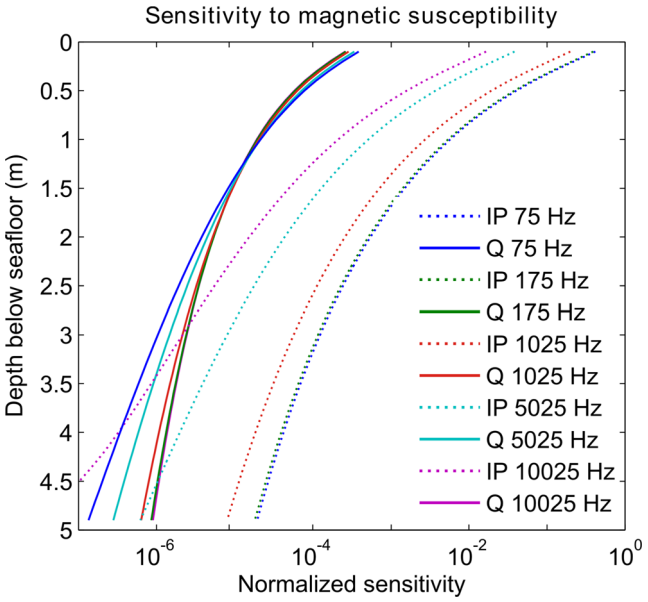

Figure 4. Sensitivities to susceptibility at 75, 175, 1025, 5025 and 10 025 Hz. Solid lines mark sensitivities of in-phase (IP) and dashed lines indicate sensitivities of quadrature (Q) components of the sensor response.

to take the logarithm of the data and model vector. Since our data contains negative values in most cases (see Fig. 2), we cannot work in the logarithmic domain. We therefore use the absolute value of a data normalized semi-logarithmic sensitivity matrix **S**. Its elements are given by

$$S_{ij} = \left| \frac{1}{d_i} \cdot \frac{\partial d_i}{\partial \log(m_j)} \right| = \left| \frac{m_j}{d_i} \cdot \frac{\partial d_i(\mathbf{m})}{\partial m_j} \right| . \quad (7)$$

Figs 3 and 4 show the sensitivities for 75, 175, 1025, 5025 and 10 025 Hz signals for conductivity and susceptibility to a depth of 5 m. The underlying forward modelling is based on the GEM-3 sensor configurations as explained in the previous section. We assume that the sensor is located in sea water with a conductivity of 4.4 S m^{-1}, 0.25 m above a homogeneous subseafloor with conductivity of 1 S m^{-1} and magnetic susceptibility of 400 $\times$ 10^{-6}. For the sensitivity calculations we discretize the lower half-space into 0.1-m-thick layers.

From Fig. 3 it can be seen that at shallow depths down to ≈0.5 m the quadrature components have the highest sensitivities. In this depth range quadrature sensitivities differ only slightly in magnitude and slope over all frequencies. Below 1 m depth the quadrature sensitivity is highly dependent on frequency; not surprisingly sensitivities of higher frequencies decrease more with depth than those of lower frequencies. The sensitivities of the in-phase components, in general, decrease less than the quadrature sensitivities do. In-phase components at 1025 Hz and above have substantial conductivity depth information, whereas conductivity has only a minor effect on in-phase components at 75 and 175 Hz.

Fig. 4 depicts EM sensitivity to susceptibility change at various depths. It can be seen that nearly all susceptibility information is contained in the in-phase components. Susceptibility sensitivities of in-phase components at all shown frequencies decrease parallel with depth. This indicates that all in-phase components are similarly affected by susceptibility depth variations and therefore do not provide independent depth information about susceptibility. However, if noise is present in the data the signal-to-noise ratio may differ at different frequencies and hence influences the DOI. The comparison with Fig. 3 shows that quadrature values have by some orders of magnitude higher sensitivities to conductivity than towards susceptibility. The low-frequency (75 and 175 Hz) in-phase values have the highest sensitivities to susceptibility, near the surface they are even higher than the quadrature sensitivities towards conductivity are (Fig. 3).

3.2 DOI

To analyse the DOI we follow the work of Christiansen & Auken (2012), who developed a global measure for DOI of geophysical EM systems. Their approach has the advantage of taking all data points and the actual model into account. Their absolute threshold value does not hold true for our applications because of fundamental differences between their models and ours, as we consider models with magnetic susceptibility different from zero and negative data. We therefore adapted their approach to calculate an absolute DOI based on a reference threshold. In the first step we take the sum of each column of S:

$$\overline{S}_j = \sum_{M}^{i=1} S_{ij} . \quad (8)$$

Now, $\overline{S}$ contains the total normalized sensitivities for the model parameters with respect to all frequencies. In the next step we sum the layer sensitivities upward to determine cumulated total sensitivities.

Fig. 5 shows cumulated values of $\overline{S}$. The black crosses indicate the points where a value of 0.11 is reached which corresponds to 5 per cent of the integral sensitivities to conductivity for this specific model. We define this sensitivity value as a reference threshold to calculate an absolute DOI for different models. One has to keep in mind that this value has no empirical background and therefore does not indicate to which depth an inversion model can be regarded as reliable. However, this global reference value provides a measure to compare the DOI for different models, hence different geological situations and system configurations. In the following sections we

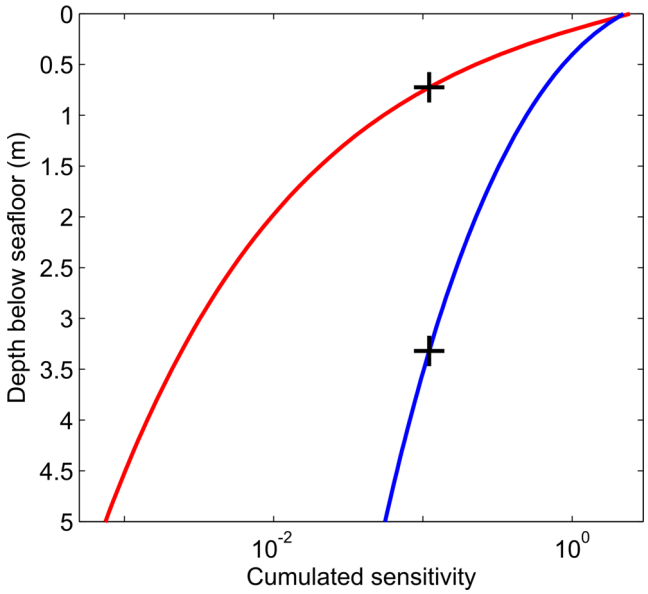

Figure 5. Cumulated values of the total sensitivity $\overline{S}$ with respect to conductivity (blue line) and susceptibility (red line). Black crosses indicates the depth where the cumulated sensitivities corresponds to the reference threshold value of 0.11.

use this absolute threshold to calculate the DOI from the actual inversion models.

For the model and sensor configuration considered in Fig. 5, the total sensitivity to susceptibility decreases much more with depth than sensitivity to conductivity. The uppermost 0.7 m contribute to 95 per cent of the susceptibility sensitivity, while the layer corresponding to 95 per cent of the sensitivity to conductivity is 3.3 m thick. Simultaneous 1-D inversion would therefore only be possible for very shallow depths, for which no sufficient depth resolution is available. This indicates that simultaneous 1-D inversion for magnetic susceptibility and electric conductivity is not possible for this CLEM system and model. Nevertheless, the cumulative total sensitivity to susceptibility is about 10 per cent higher than to conductivity, which makes accurate susceptibility information indispensable for 1-D conductivity inversion.

4 INVERSION

4.1 Half-space inversion

Under the above-mentioned conditions in which low-frequency in-phase components primarily respond to susceptibility and high-frequency quadrature components essentially to conductivity, an independent inversion of susceptibility and conductivity produces reasonable half-space models. This does not hold true for a very weakly or very highly magnetic subsurface. In a weakly magnetic environment the in-phase component is significantly affected by conductivity, and for a highly magnetic subsurface, susceptibility has a non-negligible influence on high-frequency quadrature components.

In our studies, we therefore use a non-linear least-square inversion approach incorporating the in-phase and quadrature components of all frequencies to invert simultaneously for conductivity and susceptibility. This leads to an overdetermined problem which is solved by iteratively minimizing the weighted data misfit function

$$\Phi_d = \|\mathbf{W}_d\,(\mathbf{f}\,(\mathbf{m}) - \mathbf{d})\|^2 = \sum_{i=1}^{M}\left[\frac{1}{\xi_i}\,(f_i\,(\mathbf{m}) - d_i)\right]^2, \tag{9}$$

which measures the discrepancy between the observed data **d** and the forward modelling operator **f**(**m**) calculated for the model parameter **m**, where $\|\cdot\|$ indicates the l_2-norm. The data vector **d** contains the measured in-phase and quadrature components for each frequency as independent data. The model vector **m** contains the logarithms of half-space conductivity $\sigma_{\rm hs}$ and half-space susceptibility $\mu_{\rm hs}$. The logarithms are used to ensure positivity of the model parameters. The elements of the diagonal weighting matrix $\mathbf{W}_d$ are the reciprocals of the standard deviation ξ_i of the errors in the ith observation. Linearization and minimization of the problem in eq. (9) leads for the kth iteration to the normal equation

$$\mathbf{J}_k^T\mathbf{W}_d^T\mathbf{W}_d\mathbf{J}_k\delta\mathbf{m}_k = \mathbf{J}_k^T\mathbf{W}_d^T\mathbf{W}_d[\mathbf{d} - \mathbf{f}(\mathbf{m}_k)]\,, \tag{10}$$

where $\mathbf{J}_k$ is the Jacobian matrix with respect to half-space conductivity and half-space susceptibility. After solving eq. (10) the model update is given by $\mathbf{m}_{k+1} = \mathbf{m} + \delta\mathbf{m}_k$.

4.2 1-D conductivity inversion

The goal of the 1-D inversion is to recover a vertical conductivity distribution explaining the observed data in a simple and reasonable way. We use in-phase and quadrature data of all frequencies to guarantee the best possible vertical resolution and highest DOI. Since in-phase components are significantly influenced by magnetic susceptibility even for a low magnetic subsurface, we need accurate susceptibility information. As was explained in the previous paragraph, this can be obtained through half-space inversion.

EM profiling offers a dense lateral series of soundings. Therefore, 2-D inversion seems reasonable, but is still relatively slow for large data sets. A computationally less expensive method combining neighbouring soundings is lateral constraint inversion (Auken & Christiansen 2004; Siemon *et al.* 2009). In our studies 1-D conductivity distributions were recovered using a multilayer inversion approach, in which the lower half-space is divided into multiple layers with predefined thickness. The data of two adjacent soundings are then inverted simultaneously for the conductivity of each layer. The resulting inverse problem is solved using a standard Tikhonov regularization method (Tikhonov & Arsenin 1977). The idea is to select a model that adequately fits the data and meets some constraints on model structure at the same time. The resulting cost function to be minimized can be written in compact form as

$$\Phi = \Phi_d + \lambda^2\Phi_m. \tag{11}$$

Here, Φ_d is a weighted data misfit function:

$$\Phi_d = \|\mathbf{W}_d\,(\mathbf{f}\,(\mathbf{m}) - \mathbf{d})\|^2 = \sum_{i=1}^{M}\left[W_{ii,d}\,(f_i\,(\mathbf{m}) - d_i)\right]^2, \tag{12}$$

where **f**(**m**) is the multilayer model's forward response. The model parameters in vector **m** are the logarithms of σ for each layer. The weighting function $\mathbf{W}_d$ is a diagonal matrix with the elements

$$W_{ii,d} = \left|\frac{1}{\xi_i}\cdot\frac{\partial d_i}{d_i\,\partial m_{\rm hs}}\right|. \tag{13}$$

The first term on the right-hand side of eq. (13) contains the reciprocals of the standard deviation ξ_i of the errors in the ith observation. The second term accounts for the different sensitivities of

the components in **d**. It is computed by taking the partial derivations of the *i*th datum with respect to a homogeneous half-space model m_{hs} derived from preceding half-space inversion and normalizing it by the data.

In consequence, a datum with high sensitivity-to-amplitude ratio and low uncertainty contributes more to the data misfit than a datum with low sensitivity and high uncertainty. The regularization (Tikhonov) parameter λ controls the trade-off between data misfit and model structure measured by the model constraint function

$$\Phi_m = \left\|\mathbf{W}_v\mathbf{m}^{\mathrm{I}}\right\|^2 + \left\|\mathbf{W}_v\mathbf{m}^{\mathrm{II}}\right\|^2 + \left\|\mathbf{W}_l(\mathbf{m}^{\mathrm{II}} - \mathbf{m}^{\mathrm{I}})\right\|^2, \tag{14}$$

which penalizes models with sharp vertical and lateral layer transitions. The first two terms are vertical smoothness constraints, where $\mathbf{W}_v$ is a first-order finite-difference operator. The third term enforces little variation between the two adjacent models $\mathbf{m}^{\mathrm{I}}$ and $\mathbf{m}^{\mathrm{II}}$. The diagonal weighting matrix $\mathbf{W}_l$ controls the trade-off between vertical and lateral model roughness.

After inserting eq. (14) in eq. (11), minimization of the cost function Φ can be accomplished by finding the least-squares solution of the system of equations

$$\begin{pmatrix} \mathbf{W}_d^{\mathrm{I}}\mathbf{J}_k^{\mathrm{I}} & 0 \\ 0 & \mathbf{W}_d^{\mathrm{II}}\mathbf{J}_k^{\mathrm{II}} \\ \lambda^2\mathbf{W}_v & 0 \\ 0 & \lambda^2\mathbf{W}_v \\ \lambda^2\mathbf{W}_l & -\lambda^2\mathbf{W}_l \end{pmatrix} \begin{pmatrix} \delta\mathbf{m}_k^{\mathrm{I}} \\ \delta\mathbf{m}_k^{\mathrm{II}} \end{pmatrix} = \begin{pmatrix} \mathbf{W}_d^{\mathrm{I}}[\mathbf{d}^{\mathrm{I}} - \mathbf{f}(\mathbf{m}_k^{\mathrm{I}})] \\ \mathbf{W}_d^{\mathrm{II}}[\mathbf{d}^{\mathrm{II}} - \mathbf{f}(\mathbf{m}_k^{\mathrm{II}})] \\ \lambda^2\mathbf{W}_v\mathbf{m}_k^{\mathrm{I}} \\ \lambda^2\mathbf{W}_v\mathbf{m}_k^{\mathrm{II}} \\ \lambda^2\mathbf{W}_l(\mathbf{m}_k^{\mathrm{II}} - \mathbf{m}_k^{\mathrm{I}}) \end{pmatrix}, \tag{15}$$

where the upper indices distinguish between the terms referring to two adjacent soundings I and II.

5 INVERSION OF SYNTHETIC DATA

Two different synthetic data sets were generated to test the performance of the inversion algorithm. Both consist of multiple 1-D models stitched together to simulate a 2-D subsurface. This simplification holds true as long as only negligible lateral changes in sedimentology exist in the range of the system's footprint. All 1-D models comprise a homogeneous upper half-space simulating sea water of 4.4 S m^{-1} electric conductivity and -9×10^{-6} SI magnetic susceptibility. The susceptibility of the subsurface was kept constant at 400×10^{-6} SI for all models to highlight the conductivity effect. The sensor configuration described in Section 2 was used. Both synthetic data sets were calculated by eq. (1) and then corrupted with normally distributed random noise. A relative noise level of 1 per cent of the modelled response in addition to a systematic bucking error of 1 ppm of the primary field was added to the in-phase and quadrature data of each frequency. We recovered half-space conductivity and susceptibility simultaneously and used these values as a starting model for the 1-D inversions.

The first pseudo-2-D model shown in Fig. 6 represents a 1 m thick conductive layer of 2 S m^{-1} conductivity at 1 m sediment depth embedded in a resistive environment of 0.1 S m^{-1} conductivity. This model is meant to reveal resolution abilities and limitations of roughness penalizing inversion to recover sharp layer boundaries.

Figs 7(a) and (b) show the half-space inversion results for the noisy data (solid line) and noise-free data (dashed line). The relative standard deviation of half-space conductivity recovered from the noisy data is 8 per cent of the conductivity recovered from noise-free data, while the recovered susceptibility models have a standard deviation of only 1 per cent of the noise-free susceptibility models. The higher uncertainty of the half-space conductivity can be explained by the relatively low subsurface conductivity, resulting

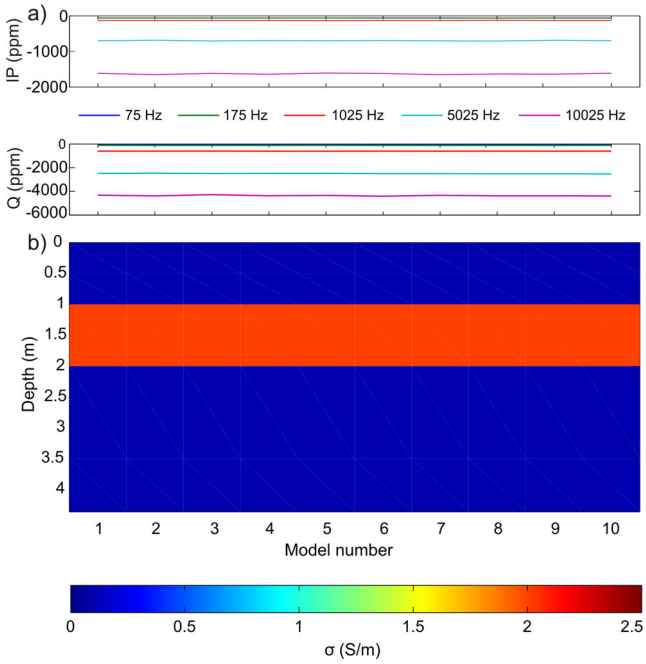

Figure 6. (a) In-phase and quadrature values of the forward response of the synthetic models (b), considering sea water conductivity of 4.4 S m^{-1} and constant subsurface susceptibility of -9×10^{-6} SI.

in total sensitivities to conductivity that are lower than those to susceptibility are. It can also be seen, that the susceptibility recovered from the noisy and noise-free data slightly undershoots true susceptibility.

Fig. 7(c) shows the conductivity models obtained from 1-D inversion with only vertical smoothing constraints. It can be seen that the random noise in the data leads to significant differences between the models along the profile and to an unsteady 2-D representation. Furthermore, the layer boundaries are very fuzzy. Inclusion of lateral constraints (Fig. 7d) improves the vertical resolution and produces more consistent models, so that the structure of the true model is represented reasonably well. Nevertheless, both inversions underestimate the conductivity of the conductive layer. The grey and the black lines in Figs 7(c) and (d) indicate two different measures of DOI. The grey line represents the DOI using the absolute reference threshold value explained in Section 3.1. In contrast, the black line indicates a relative DOI, namely the depth above which the sediments comprise 95 per cent of the cumulated sensitivity of the respective model. For both measures the sensitivities were calculated from the actual inversion output. The fact that the relative DOI lies deeper than the absolute DOI indicates that the cumulated sensitivity for this model here is significantly lower than for the reference model. This is due to the low conductivity of the uppermost layer.

The second model (Fig. 8) represents a clayey overburden covering highly compacted low-porous sediments, a common geological setting on clastic shelves. The thickness of the clay layer decreases towards the centre. The conductivity of the clay layer decreases gradually with depth, representing pore space reduction due to compaction. In comparison to the first model the second model changes laterally as well as vertically and hence offers the possibility to investigate the interaction of lateral and vertical constraints.

The inversion results of the second synthetic data set are represented in Fig. 9. Due to the higher conductivities and therefore

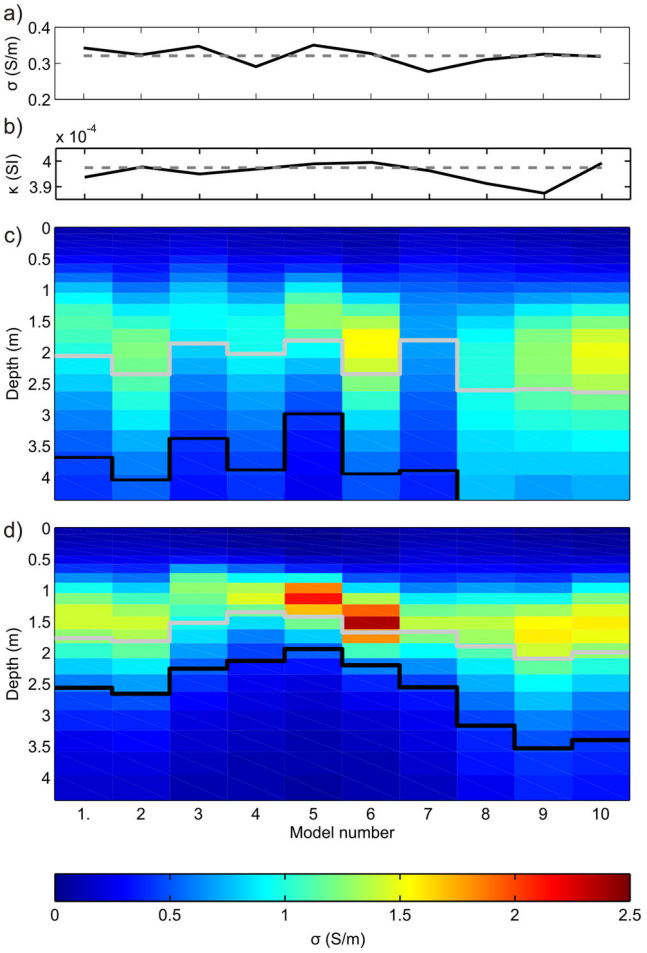

Figure 7. Inversion results for the models given in Fig. 6: (a) Half-space inversion results of subsurface conductivity and (b) susceptibility, considering noisy (dashed lines) and noise-free data (solid-lines). (c) 1-D inversion results with only vertical smoothing constraints and (d) pseudo 2-D inversion results considering vertical and lateral constraints. Grey and black line indicate absolute, respectively relative measures of DOI.

higher sensitivities, the effect of the noise on the recovered conductivity is much lower than it is in the previous data set.

From the inversion of the noise-free data (dashed line) it can be seen that the recovered half-space susceptibility shows the same trend as the conductivity. Hence, the susceptibility models are influenced by the conductivity model. However, this influence is less than the effect of noise in the data. It also appears that the recovered half-space susceptibility values slightly exceed the susceptibility of the true model. Since the vertical conductivity transitions in the second example are much smoother than in the first example, the 1-D inversion output is less affected by unwanted smearing of the smoothness constraints. Consequently, both 1-D inversions recover the structure of the true models well. The improvement by adding lateral constraints to the inversion is not as significant as in the first example. Nevertheless, the models recovered with lateral constraints represent the symmetry of the true model more accurately. The 1-D conductivity distributions are recovered most precisely at the outer models where the conductivity transitions are smooth. The thin conductive layer in the two middle models can not be properly resolved and is smeared. Both, the absolute and relative DOI decreases where the thickness of the underlying low

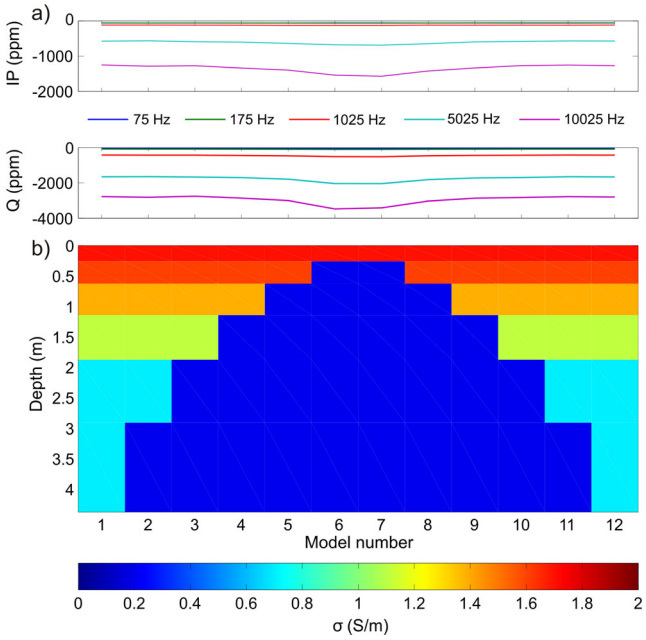

Figure 8. (a) In-phase and quadrature values of the forward response of the synthetic models (b), considering sea water conductivity of 4.4 S m^{-1} and constant subsurface susceptibility of -9×10^{-6} SI.

conductive sediment increases. Additionally, the conductive surface layer shifts the relative DOI to shallower depths.

To demonstrate the relevance of susceptibility information to recover reliable conductivity models, the synthetic data set shown in Fig. 6(a) was inverted again for 1-D conductive, non-magnetic models. It is clear from our sensitivity analyses (Figs 3–5) that even for a moderately susceptible subsurface and high frequencies the in-phase components are significantly influenced by susceptibility. As Farquharson *et al.* (2003) discussed in detail, it is impossible to invert in-phase components with remarkable susceptibility effects for conductive, but non-susceptible, models. Hence, if susceptibility information is not available only the quadrature components can be inverted. Fig. 10 shows the results of inverting only the quadrature components of the data shown in Fig. 6(a) to recover 1-D conductivity assuming a non-magnetic subsurface. The same vertical and lateral constraint as for inversion results in Fig. 7(d) were used. It can be seen that the conductive horizon could not be properly reconstructed. As already illustrated in Fig. 3 the in-phase components provide substantial conductivity-depth information. A lack of this information reduces the capability of the inversion to determine the vertical conductivity structure. Thus, the susceptibility recovered from half-space inversion is not only complementary information; making it possible to incorporate the in-phase components it also improves the results of the 1-D conductivity inversion.

6 ACQUISITION AND CALIBRATION OF FIELD DATA

6.1 EM profiler

EM data acquisition has been realized with the recently developed MARUM NERIDIS III system (NERItic DIScoverer; Fig. 11), a successor model to the EM profiler NERIDIS II described in Müller *et al.* (2012). NERIDIS III is a multisensor bottom towed profiler equipped with a marinized CLEM sensor based on the commercial GEM-3 system (Won *et al.* 1997). EM data were recorded at five

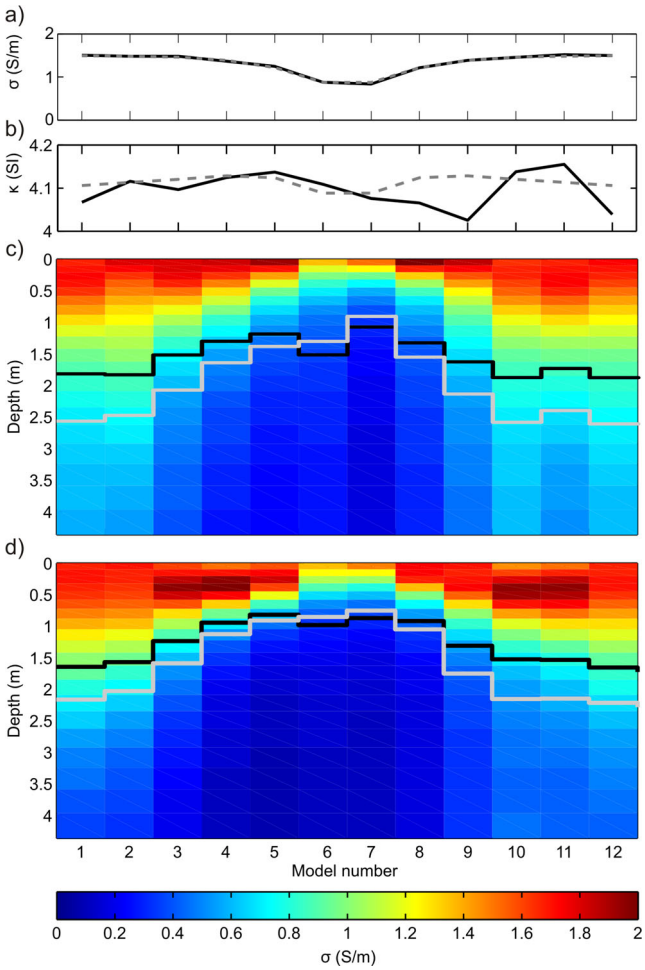

Figure 9. Inversion results for the models defined in Fig. 8: (a) half-space inversion results of subsurface conductivity and (b) susceptibility, considering noisy (dashed lines) and noise-free data (solid-lines). (c) 1-D inversion results with only vertical smoothing constraints and (d) pseudo-2-D inversion results considering vertical and lateral constraints. Grey and black line indicate absolute, respectively relative measures of DOI.

operation frequencies of 75, 175, 1025, 5025 and 10 025 Hz with a sampling rate of 25 Hz. Sea water conductivity was measured by a conductivity temperature depth (CTD) probe embedded in the profiler and used as upper half-space conductivity in our modelling and inversion schemes. CTD conductivity together with temperature also yields information on sea water salinity indicating changes in sea water masses. The depth information is used for high-resolution along-track bathymetry. The EM measurements with the given sensor setup demand a permanent ground contact of the profiler (Müller *et al.* 2012), which can be maintained at tow speeds of up to four knots at a tow angle of 20°. The relative position of the profiler behind the tow ship is determined by triangulation of CTD water depth and the length of the tow rope.

6.2 Data calibration

In theory a CLEM sensor should measure only the secondary EM field as described by eq. (1). In practice, the sensor additionally measures a superimposed residual primary field B due to incomplete bucking. This residual field can be split into two components. The first is owed to the sensor configuration and can be calculated by means of known sensor settings (coil radii and number of turns)

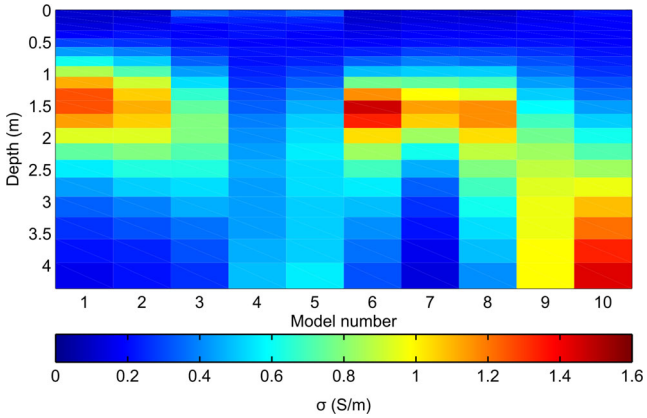

Figure 10. Results of inverting only the quadrature components of the data shown in Fig. 6(a) for 1-D conductivity, assuming a non-magnetic subsurface.

and upper half-space conductivity. The second component is a bias term which comprises all static offsets and dynamic shifts of the primary field signal. Fig. 12 shows measured EM data and the theoretical residual primary field during a descent in the water column for 75 and 1025 Hz. The water conductivity is decreasing from low to high data point numbers. One can see strong discrepancies between the measured and calculated data in the in-phase as well as quadrature component. The residuals between theoretical data and measured data (Figs 12c and d) indicate that there is both a constant off-set and a systematic trend in the errors. This becomes clearer when we plot measured water column data B_{EM} against CTD-based calculated data B_{CTD} (Fig. 13). In this representation a linear relation between the amplitudes and the phases is observable. Fig. 14 shows the same data as Fig. 12 after calibration. It can be seen that the calculated data incorporating the calibration terms match the measured data well. Most likely, a combination of different factors is responsible for these data errors and their source is not yet completely understood. Nevertheless, there are three main causes for the observed systematic errors.

(i) We noticed that the ferrite calibration we applied to the instrument is very sensitive to ambient noise and the location of the calibration ferrite core. It is therefore likely that the initial land calibration carried out before every survey was imprecise.

(ii) The EM data are normalized by the primary field of the transmitter coil measured with a reference coil. This value is scaled to equal the primary field at the receiver coil. The scaling factor is a factory determined scalar value, which is only valid for land applications and must be adapted for marine applications on ambient conductivity and signal frequency.

(iii) Even though the use of conductive metal in the NERIDIS III platform was kept as low as technically possible, some indispensable metallic parts probably caused some interference with the EM field.

To enable inversion and quantitative interpretation of the EM data even in the presence of intrinsic system bias, we developed a calibration scheme which includes the following steps:

(1) Starting with the raw data, standard techniques to reduce random noise in the data were applied (here we used a running-mean filter with a window length of 10 data points equivalent to 0.4 s or 1 m propagation).

(2) The primary EM response was then calibrated by comparing the observed EM data at different depth in the water column during descent and lift of the profiler with predicted values calculated

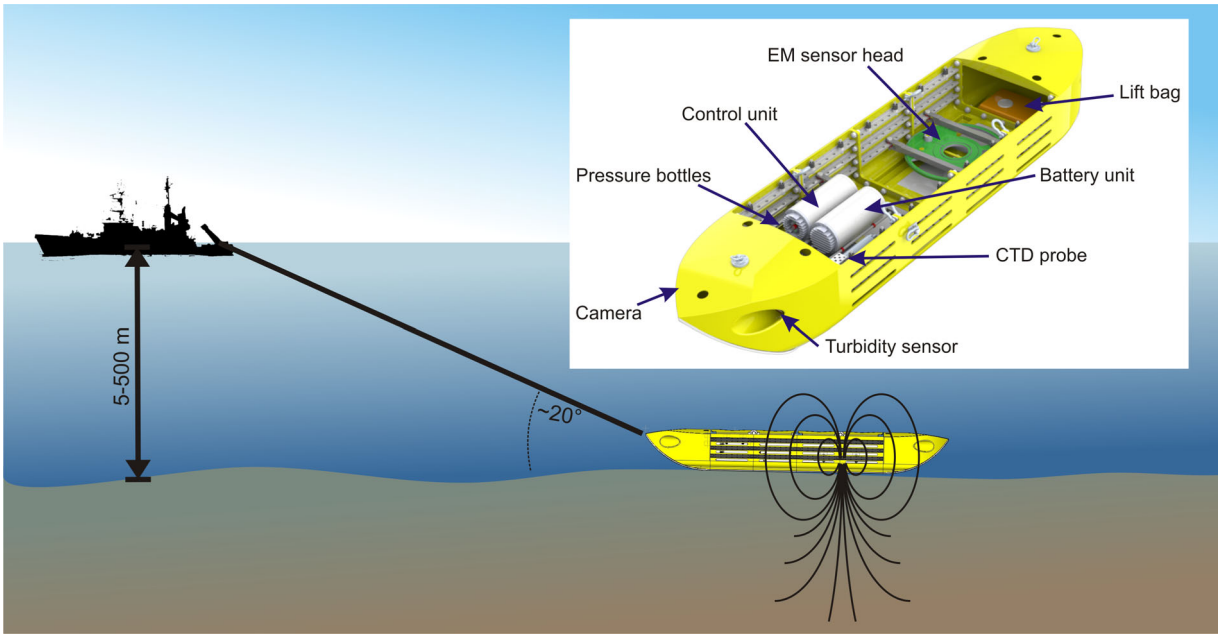

Figure 11. NERIDIS III setup: the hull (length: 5.2 m; width: 1.2 m; height: 0.8 m) is made of non-conductive non-magnetic fiberglass. The closeup shows the interior of the profiler (without covers) with all measuring instruments (CLEM sensor, CTD probe, turbidity sensor). The battery unit (two 40 Ah lithium ion battery packs) is designed for up to 12 hr mission durations. Two lift bags, autonomously filled with compressed air, bring the profiler back to the sea surface in the event of loss of communication.

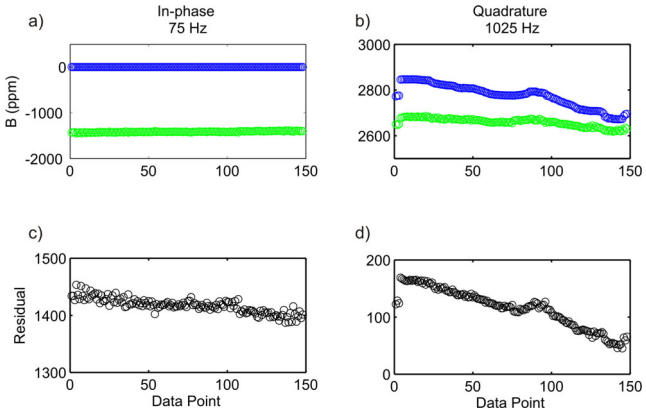

Figure 12. EM data (green circles) for different sea water conductivities measured during descent of the profiler together with corresponding CTD-based calculated EM data (blue circles). (a) 75 Hz in-phase component, (b) 1025 Hz quadrature component, (c) and (d) residuals.

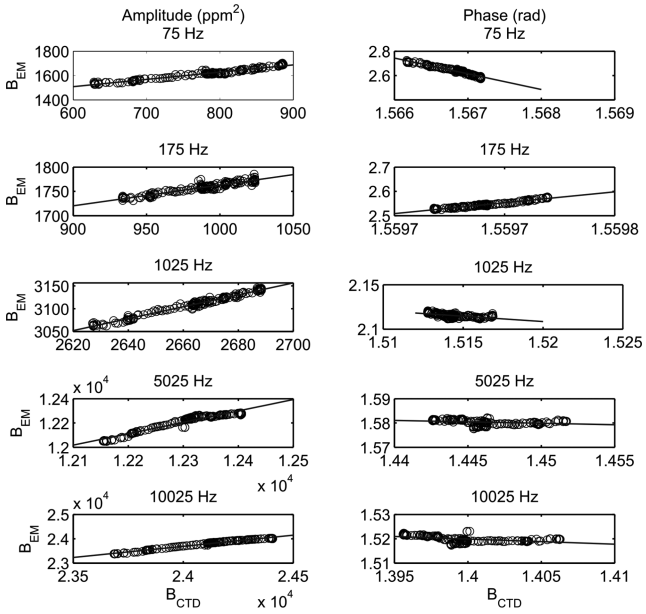

Figure 13. EM data measured with the EMI sensor in the water column versus calculated EM primary filed data (circles); left-hand column: amplitudes, right-hand column: phases. Lines model linear trend.

from CTD conductivities and a water susceptibility of -9×10^{-6} SI. Using the conductivity depth variations in the water column, primary field calibration parameters were determined through linear regression for amplitude and phase separately.

(3) These calculated calibration parameters were used to determine the primary field from the CTD conductivity, which was then removed from the EM data. Thereafter, the secondary EM field was isolated.

(4) The secondary EM field was controlled and eventually calibrated using ground truth data. For this purpose surface samples were taken with a short (80 cm) gravity corer at several locations along the EM profiles. Electric conductivity was measured directly on board the research vessel with a hand-held direct current probe with miniaturized four-electrode-in-line Wenner configuration with 4 mm electrode spacing. Susceptibility was determined with a laboratory susceptometer.

A detailed description of the calibration procedure is given in the Appendix A.

7 NW IBERIAN SHELF STUDY

The exemplary field EM data presented here was collected on the Northwest Iberian continental shelf. Müller *et al.* (2012) have demonstrated the eminent potential of benthic EM profiling to classify and characterize the prevailing sediment facies in this study area. They were able to identify the major facies units based on

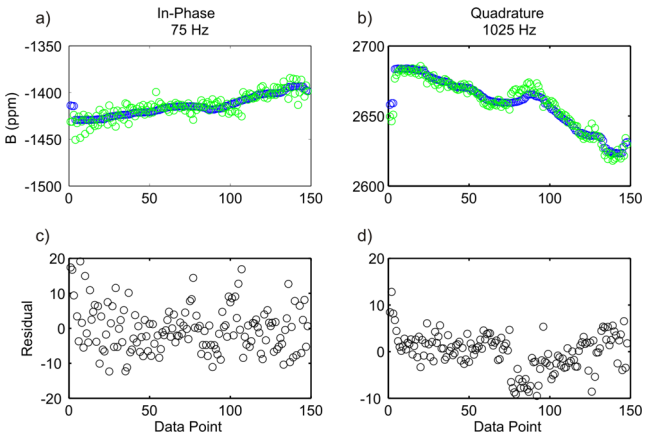

Figure 14. Measured EM data (green circles) and calculated EM data after calibration (blue circles). (a) 75 Hz in-phase component, (b) 1025 Hz quadrature component, (c) and (d) respective residuals.

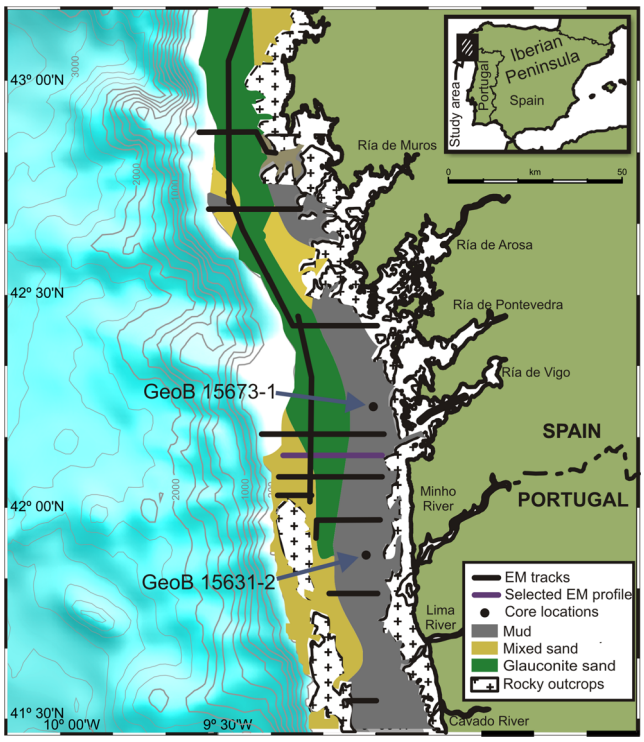

Figure 15. NW Iberian shelf. Colours indicate sediment facies, black lines indicate EM profiles from RV Poseidon cruise P366/3 and RV Meteor cruise M84/4b, black dotes indicate core locations. Modified from Lantzsch *et al.* (2010).

EM conductivity and susceptibility data recovered from half-space inversion. Their results clearly correlate with sample based sedimentological facies distribution (Dias *et al.* 2002; Lantzsch *et al.* 2010). In particular, the well-known mid-shelf mud depocentre is identified by high conductivity and magnetic susceptibility. A further prominent finding is a subaqueous dune field located at mid shelf. Fig. 15 provides an overview of the major facies units after Lantzsch *et al.* (2010) and all presently existing EM profiles of the study area. While the internal structure of the mud depocentre has not been investigated in detail yet, porosity logs of gravity cores (Fig. 16) show complex vertical stratification and mixing. Here, 1-D EM inversion is expected to reveal new details about the thickness, composition and vertical stratification of local and regional

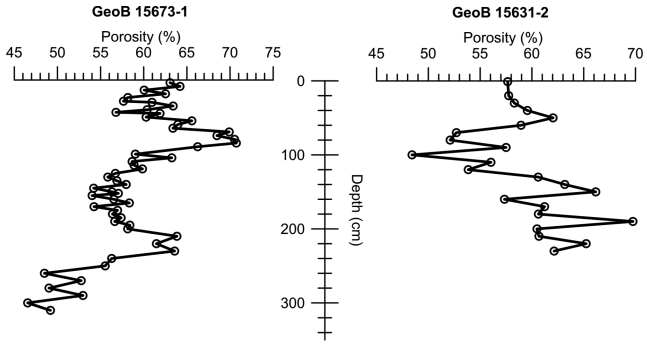

Figure 16. Porosity data from two gravity cores on the GMB (locations are indicated by black dots in Fig. 15).

mud depocentres. The task of a more recent EM profiling in 2011 was to map the dune field in higher detail and to resolve the boundaries and internal structures of the mud depocentre. The long term goal envisages the use of benthic EM profiling to achieve deeper insights into the small and large scale effects and interrelationships of hydro-, sediment- and morphodynamics in this area. After a short introduction to the sedimentary settings of the study area and a description of the EM system used for data we present half-space and 1-D inversion results.

7.1 Sedimentary setting

The NW Iberian shelf is a high energy, low accumulation non-glaciated clastic shelf system (Lantzsch *et al.* 2009a,b) with typical water depths of 80–200 m. The main sediment types, patterns and their distributions were described by, for example, Dias *et al.* (2002), Corredeira *et al.* (2009) and Lantzsch *et al.* (2010). A high input of fine fluviogenic sediments originating mainly from the Duoro River has led to the formation of a well defined 50-km-long and 2–3-km-wide coast-parallel mud depocentre (Dias *et al.* 2002). This so-called 'Galicia Mud Belt (GMB)' (Lantzsch *et al.* 2009b) is located mid-shelf, north of the Minho River estuary at 110–120 m water depth and made up of 90 per cent silty and clayey material (Dias *et al.* 2002). Seawards the GMB is bordered by relict sediments and massive glauconite formations. This glaucony facies consists of up to 50 per cent paramagnetic glaucony (Odin & Lamboy 1988). On the outer shelf, a mixed sand facies consisting mainly of carbonate microfossil fragments, quartz and mica, has been identified (Lantzsch *et al.* 2010). A budget analysis by Oberle *et al.* (2014) showed that more than 60 per cent of the original fluvial input has been transported off shelf.

7.2 Half-space inversion of field data

Fig. 17 shows the apparent conductivity and apparent susceptibility reconstructed by half-space inversion as explained in Section 4.1. Porosities and susceptibilities obtained from surface samples are shown by symbols. Surface porosities were obtained from wet and dry weighing of samples from a depth interval of 2–4 cm. Surface susceptibility was measured in 2 cm intervals with a 'KappaBridge Susceptibility Meter'. The mean values of the uppermost 10 cm are shown.

The mud facies located between kilometre 0 and 7 is characterized by high conductivity of up to ≈1.2 S/m and relatively high susceptibility of up to ≈500 × 10^{-6} SI units. High values of both parameters are associated with a high content of fines. Fine sediments tend to have higher porosities due to the card house fabric

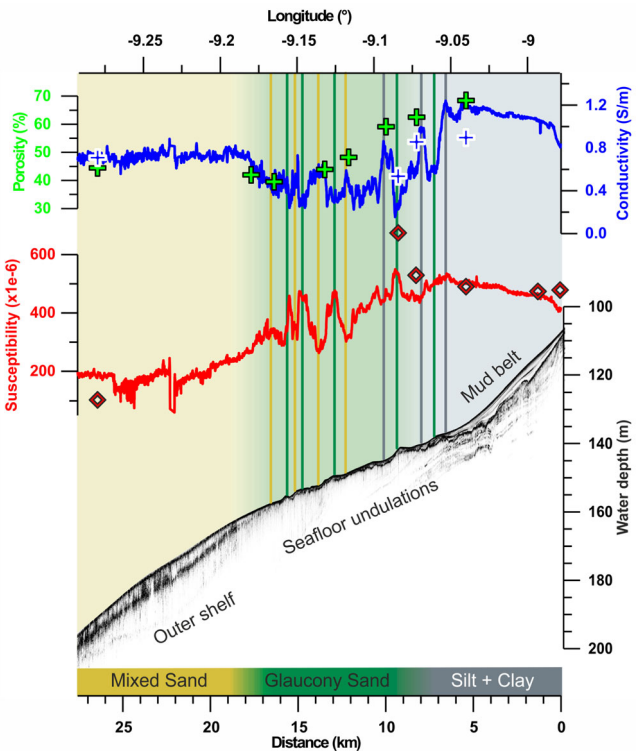

Figure 17. Top panel: half-space inversion results together with ground truth data. The blue line indicates apparent conductivity, red line the apparent susceptibility. Blue crosses, green crosses and red diamonds indicate surface sample conductivities, porosities and susceptibilities, respectively. Vertical lines indicate sediment crests and troughs. Line colour and background colour indicate particular sediment facies. Bottom panel: seismo-acoustic image derived from the RV Meteor on-board sediment echosounder.

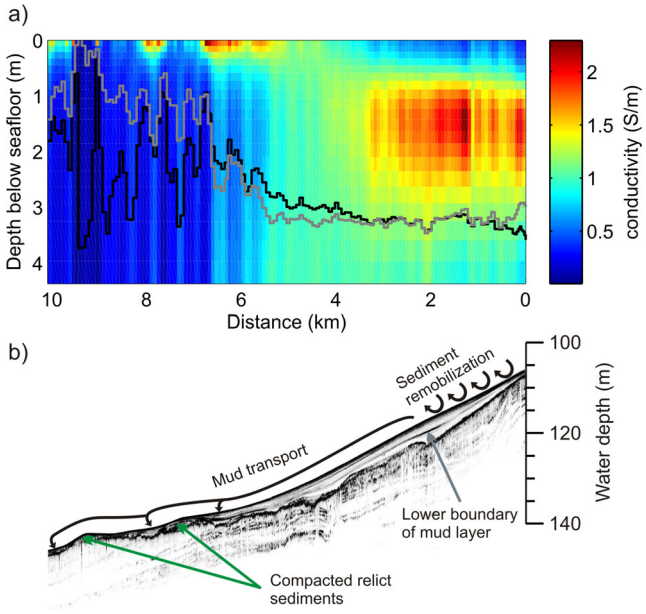

Figure 18. (a) Pseudo 2-D model from vertically and laterally constraint 1-D inversion, grey and black line indicate absolute, respectively relative measures of DOI. (b) Seismo-acoustic image derived from the RV Meteor on-board sediment echosounder.

of clay minerals, which corresponds to high conductivity values. Additionally, magnetic minerals are expected to enrich in the fine fraction (Booth *et al.* 2005), due to their usually fine crystal size in their magmatic parent rocks (Müller *et al.* 2011). Notice the slight increase from east to west of both conductivity and susceptibility, which suggests an accumulation of fines at the western edge of the mud belt.

The adjacent glaucony sand facies (≈kilometre 8–18) is characterized by depth undulations with a 2–3 km crest interval and a comparably low relief of less than 3 m. These undulations can be precisely detected with the NERIDIS III internal CTD probe. Hydroacoustic sections indicate that the depth undulations are induced by dipping regressive sediment substructures. The crests of these structures are characterized by susceptibility highs and conductivity lows. The low conductivity can be explained by a high degree of compaction of these relict sediments, resulting in low porosity. The high susceptibility represents a relatively high content of paramagnetic glaucony. Porosities in the troughs are generally higher, while susceptibilities are lower than on the crests. Both are decreasing from east to west, which suggests a change in the trough infill from finer to coarser material. The mixed carbonate and quartz sand facies on the outer shelf possesses low susceptibility and intermediate conductivity.

The apparent conductivity obtained form half-space inversion shows the same pattern as surface sample porosity. Apparent susceptibility is generally in good agreement with sample susceptibility. Deviation of individual measurements can be explained by the different DOI of EM and sample susceptibility and by discrepancies between the EM profiler and core locations. Both apparent conductivity and susceptibility agree with previous EM measurements on the NW Iberian shelf (Müller *et al.* 2012). At this stage of data processing, the general problem of interpreting apparent half-space values becomes obvious: additional information is needed to distinguish between compositional changes of seafloor sediments (in the case of a homogeneous half-space) and variations in layer thickness (in the case of stratified contrasting sediments). This problem can be overcome by 1-D inversion.

7.3 1-D inversion of field data

1-D inversion of this shelf profile was carried out using vertical and lateral constraints according to Section 4.2. The lateral constraints were chosen to be twice the vertical constraints. The lower half-space was discretized into 20 layers with increasing thickness from 0.1 to 0.4 m. Fig. 18 shows a pseudo 2-D section from the same profile as before but restricted to kilometre 0–10, representing the GMB and the transition to the glaucony sand facies. The 2-D representation was obtained from 1-D models that were stitched together. The mean distance between the 1-D models is ≈70 m, which offers an adequate resolution for the sedimentary structures under investigation.

The highly compacted relict sediments between kilometre 6.2 and 10 are represented by a very low conductivity and appear as homogeneous sediment body. These low conductivities produce weak secondary EM fields resulting also in low sensitivities. Hence, the absolute DOI decreases to less than 1 m. At the GMB, it can be seen that the westwards increase in conductivity suggested by the half-space values is confined to the topmost sediments, which implies that the apparent conductivity recovered from half-space inversion is almost purely controlled by shallow sediments. The most conductive sediment is found at a depth of approximately 1–1.5 m below the seafloor, between kilometre 0 and 3, covered by a less conductive drape. These observations are supported from the porosity core data shown in Fig. 16, where the highest porosities are found in

0.84 and 1.9 m depth for core GeoB 15631-2 and GeoB 15673-1, respectively. The seismo-acoustic image (Fig. 18b) cannot resolve the uppermost metre due to the high reflectivity of the seafloor, which produces a wide bottom reflection covering the topmost layers. Nevertheless, the lower boundary of the highly conductive mud layer is clearly visible.

The vertical stratification with upwards coarsening of the GMB sediments revealed by the 1-D EM models reflects the significant present-day change of sedimentary processes by anthropogenic influences as described by Dias *et al.* (2002). It is assumed that the sediment supply towards the shelf has been significantly reduced as a result of damming the rivers. Hence, the GMB can now be mainly considered sediment source rather than sink. The fines of the uppermost GMB layers are frequently remobilized during storm events. The fine fraction, once resuspended, is transported westwards and trapped at the lee sides of the sediment ridges, where bottom current velocities are reduced. This winnowing effect leads to a coarsening of the sediments at the shallower area of the GMB and to an accumulation of fine sediments at morphological lows as localized small mud depocentres.

8 CONCLUSIONS

EM profiling with a multifrequency CLEM sensor is a new, rapid method of resolving lateral and vertical distributions of surficial marine sediment facies. We have demonstrated that simultaneous half-space inversion of marine CLEM data recovers reliable magnetic susceptibility and electric conductivity values over a range of geological settings. Furthermore, the frequency and phase dependent conductivity effect enables the reconstruction of vertical conductivity distributions. A 1-D inversion algorithm using susceptibility values recovered from prior half-space inversion was presented. It uses vertical smoothness constraints, which blur sharp layer boundaries. By adding lateral constraints and allowing more vertical variability, we can significantly enhance the depth resolution. Tests on synthetic and field data showed that, depending on geological conditions, reliable models can be recovered down to approximately 3-m-depth below seafloor. The step from 1-D to multidimensional inversion is still challenging in EM profiling. The narrow footprint of CLEM methods demands a very dense measurement grid to provide sensitivity overlapping between adjacent soundings. Consequently, for large study areas of several square kilometres one needs hundreds of thousands of measurements. For such an amount of data multidimensional inversion is not feasible at reasonable computation costs. Spatial constraint inversion is computationally much cheaper and therefore the best compromise to create pseudo 2- or 3-D models. The field data at the NW Iberian Shelf presented here was corrupted by significant static and dynamic shifts, which had to be removed before inversion. We developed a calibration scheme that successively calibrates the primary and secondary EM field. After successful calibration of the field data, the inversion results offer encouraging insights into the local sedimentology, revealing facies distributions and vertical stratification of sediment bodies.

ACKNOWLEDGEMENTS

The authors would like to thank Christian Hilgenfeldt (Marine Geophysics Group, University of Bremen), who was mainly responsible for the technical implementation of the NERIDIS III system. We further thank captain and crew of RV Meteor cruise *M*84/4. BB, HM and FO were funded through DFG-Research Center/Cluster of Excellence 'The Ocean in the Earth System'. This work was part of MARUM Research Area SD investigating sediment dynamics between the coasts, shelves and continental slopes. BB and FO were supported by GLOMAR – Bremen International School for Marine Sciences. Finally, we would like to thank the two reviewers Andrej Swidinsky and Colin Farquharson for their helpful comments and suggestions that improved this manuscript.

REFERENCES

Auken, E. & Christiansen, A.V., 2004. Layered and laterally constrained 2D inversion of resistivity data, *Geophysics,* **69**(3), 752–761.

Auken, E., Pellerin, L., Christensen, N.B. & Sørensen, K., 2006. A survey of current trends in near-surface electrical and electromagnetic methods, *Geophysics,* **71**(5), G249–G260.

Beard, L. & Nyquist, J., 1998. Simultaneous inversion of airborne electromagnetic data for resistivity and magnetic permeability, *Geophysics,* **63**(5), 1556–1564.

Bongiovanni, M., Bonomo, N., de la Vega, M., Martino, L. & Osella, A., 2008. Rapid evaluation of multifrequency EMI data to characterize buried structures at a historical Jesuit Mission in Argentina, *J. appl. Geophys.,* **64**(1–2), 37–46.

Booth, C., Walden, J., Neal, A. & Smith, J., 2005. Use of mineral magnetic concentration data as a particle size proxy: a case study using marine, estuarine and fluvial sediments in the Carmarthen Bay Area, South Wales, U.K., *Sci. Total Environ.,* **347**(1–3), 241–253.

Boyce, R., 1968. Electrical resistivity of modern marine sediments from the Bering Sea, *J. geophys. Res.,* **73**(14), 4759–4766.

Butler, K.E., 2009. Trends in waterborne electrical and EM induction methods for high resolution sub-bottom imaging, *Near Surf. Geophys.,* **7**, 241–246.

Carcione, J.M., Seriani, G. & Gei, D., 2003. Acoustic and electromagnetic properties of soils saturated with salt water and NAPL, *J. appl. Geophys.,* **52**(4), 177–191.

Cheesman, S.J., Edwards, R.N. & Law, L.K., 1990. A test of a short-baseline sea-floor transient electromagnetic system, *Geophys. J. Int.,* **103**(2), 431–437.

Christiansen, A.V. & Auken, E., 2012. A global measure for depth of investigation, *Geophysics,* **77**(4), WB171–WB177.

Corredeira, C., Araújo, M., Gouveia, A. & Jouanneau, J.-M., 2009. Sediments of Galician Continental Shelf: elemental composition and accumulation rates, *J. Radioanal. Nucl. Chem.,* **281**(2), 265–268.

Deszcz-Pan, M., Fitterman, D. & Labson, V., 1998. Reduction of inversion errors in helicopter em data using auxiliary information, *Explor. Geophys.,* **29**(2), 142–146.

Dias, J.M.A. *et al.*, 2002. Present day sedimentary processes on the northern Iberian shelf, *Prog. Oceanogr.,* **52**(2–4), 249–259.

Evans, R.L., 2001. Measuring the shallow porosity structure of sediments on the continental shelf: a comparison of an electromagnetic approach with cores and acoustic backscatter, *J. geophys. Res.,* **106**(C11), 27 047–27 060.

Farquharson, C.G., Oldenburg, D.W. & Routh, P.S., 2003. Simultaneous 1D inversion of loop-loop electromagnetic data for magnetic susceptibility and electrical conductivity, *Geophysics,* **68**(6), 1857–1869.

Huang, H. & Fraser, D.C., 2003. Inversion of helicopter electromagnetic data to a magnetic conductive layered Earth, *Geophysics,* **68**(4), 1211–1223.

Huang, H. & Won, I., 2000. Conductivity and susceptibility mapping using broadband electromagnetic sensors, *J. Environ. Eng. Geophys.,* **5**(4), 31–41.

Huang, H. & Won, I.J., 2003. Detecting metal objects in magnetic environments using a broadband electromagnetic method, *Geophysics,* **68**(6), 1877–1887.

Juhl Tølbøll, R. & Bøie Christensen, N., 2006. Robust 1D inversion and analysis of helicopter electromagnetic (HEM) data, *Geophysics,* **71**(2), G53–G62.

Lantzsch, H., Hanebuth, T.J. & Bender, V.B., 2009a. Holocene evolution of mud depocentres on a high-energy, low-accumulation shelf (NW Iberia), *Quater. Res.,* **72**(3), 325–336.
Lantzsch, H., Hanebuth, T.J., Bender, V.B. & Krastel, S., 2009b. Sedimentary architecture of a low-accumulation shelf since the Late Pleistocene (NW Iberia), *Mar. Geol.,* **259**(1–4), 47–58.
Lantzsch, H., Hanebuth, T.J. & Henrich, R., 2010. Sediment recycling and adjustment of deposition during deglacial drowning of a low-accumulation shelf (NW Iberia), *Continent. Shelf Res.,* **30**(15), 1665–1679.
Ley-Cooper, Y. & Macnae, J., 2007. Amplitude and phase correction of helicopter EM data, *Geophysics,* **72**(3), F119–F126.
Martinelli, P. & Duplaá, M.C., 2008. Laterally filtered 1D inversions of small-loop, frequency-domain EMI data from a chemical waste site, *Geophysics,* **73**(4), F143–F149.
Minsley, B.J., Smith, B.D., Hammack, R., Sams, J.I. & Veloski, G., 2012. Calibration and filtering strategies for frequency domain electromagnetic data, *J. appl. Geophys.,* **80**(0), 56–66.
Mitsuhata, Y. & Imasato, T., 2009. On-site bias noise correction in multi-frequency slingram-type electromagnetic induction measurements, *J. Environ. Eng. Geophys.,* **14**(4), 179–188.
Müller, H., von Dobeneck, T., Nehmiz, W. & Hamer, K., 2011. Near-surface electromagnetic, rock magnetic, and geochemical fingerprinting of submarine freshwater seepage at Eckernförde Bay (SW Baltic Sea), *Geo-Mar. Lett.,* **31**(2), 123–140.
Müller, H., von Dobeneck, T., Hilgenfeldt, C., SanFilipo, B., Rey, D. & Rubio, B., 2012. Mapping the magnetic susceptibility and electric conductivity of marine surficial sediments by benthic EM profiling, *Geophysics,* **77**(1), E43–E56.
Oberle, F.K., Hanebuth, T.J., Baasch, B. & Schwenk, T., 2014. Volumetric budget calculation of sediment and carbon storage and export for a late holocene mid-shelf mudbelt system (NW Iberia), *Continent. Shelf Res.,* **76**(0), 12–24.
Odin, G. & Lamboy, M., 1988. Glaucony from the margin off northwestern spain, in *Green Marine Clays,* pp. 249–275, ed. Odin, G., Elsevier.
Reid, J. & Bishop, J., 2004. Post-processing calibration of frequency-domain electromagnetic data for sea-ice thickness measurements, *Explor. Geophys.,* **35**(4), 283–287.
Sasaki, Y., Son, J., Kim, C. & Kim, J., 2008. Resistivity and offset error estimations for the small-loop electromagnetic method, *Geophysics,* **73**(3), F91–F95.
Sasaki, Y., Kim, J. & Cho, S., 2010. Multidimensional inversion of loop-loop frequency-domain em data for resistivity and magnetic susceptibility, *Geophysics,* **75**(6), F213–F223.
Scott, W.R., 2011. Calibration technique for broadband electromagnetic induction sensors, in *IEEE International Geoscience and Remote Sensing Symposium,* Vancouver, BC, pp. 59–62.
Siemon, B., Auken, E. & Christiansen, A.V., 2009. Laterally constrained inversion of helicopter-borne frequency-domain electromagnetic data, *J. appl. Geophys.,* **67**(3), 259–268.
Swidinsky, A., Hölz, S. & Jegen, M., 2012. On mapping seafloor mineral deposits with central loop transient electromagnetics, *Geophysics,* **77**(3), E171–E184.
Tikhonov, ï.N. & Arsenin, V.Y., 1977. *Solutions of Ill-Posed Problems,* Halsted Press.
Ward, S.H. & Hohmann, G.W., 1988. Electromagnetic theory for geophysical applications, in *Electromagnetic Methods in Applied Geophysics,* pp. 30–311, ed. Nabighian, M.N., SEG.
Won, I., 2003. Small frequency-domain electromagnetic induction sensors, *Leading Edge,* **22**(4), 320–322.
Won, I. & Huang, H., 2004. Magnetometers and electro-magnetomenters, *Leading Edge,* **23**(5), 448–451.
Won, I., Keiswetter, D., Hanson, D., Novikova, E. & Hall, T., 1997. GEM-3: a monostatic broadband electromagnetic induction sensor, *J. Environ. Eng. Geophys.,* **2**(1), 53–64.
Zhang, Z. & Oldenburg, D.W., 1999. Simultaneous reconstruction of 1-D susceptibility and conductivity from electromagnetic data, *Geophysics,* **64**(1), 33–47.

APPENDIX A: CALIBRATION PROCEDURE

Assuming a linear relationship between the observed data $d_{\rm obs}$ and theoretical data $d_{\rm cal}$ calculated for known model parameters, the aim of the calibration is to find both multiplicative and additive calibration terms that minimize the difference between the left- and right-hand side of the following equation (Deszcz-Pan *et al.* 1998; Reid & Bishop 2004; Minsley *et al.* 2012):

$$d_{\rm obs}(f) = Q(f)[d_{\rm cal}(f) + B(f)], \tag{A1}$$

where f is the frequency, Q is a complex and frequency dependent gain factor and B is a complex and frequency dependent bias term. The additive bias term mainly comprises incomplete bucking of the primary EM field response caused by the mutual coupling between the receiver and transmitter coil. For marine measurements, the bias term becomes dependent of water conductivity, and therefore changes with sea water temperature and salinity. Assuming that the sensor is land-calibrated in such a way that B vanishes in air, the theoretical value for B in water is then the difference of the whole-space EM responses in water $U_{p,\,\rm w}$ and air $U_{p,\,0}$:

$$B = \underbrace{\frac{2R_t^2}{R_r}\int_0^\infty G\frac{\lambda}{u_{\rm w}}\,\partial\lambda}_{U_{p,\rm w}} - \underbrace{\frac{2R_t^2}{R_r}\int_0^\infty G\,\partial\lambda}_{U_{p,0}}\ , \tag{A2}$$

with

$$G = \left[J_1(\lambda R_t) - \frac{n_b R_b}{n_t R_t} J_1(\lambda R_r)\right]. \tag{A3}$$

The geometric term G accounts for the two reverse EM fields of the bucking coil with radius R_b and number of turns n_b and the transmitter coil with radius R_t and number of turns n_b at the receiver coil with the Radius R_r. J_1 is the Bessel function of first kind and order, and λ is the Hankel transformation parameter. See appendix of Müller *et al.* (2012) for further explanation. We can calculate theoretical values for $B_{\rm CTD}$ taking the sea water conductivity from the CTD probe of NERDIS III and water susceptibility of -9×10^{-6} SI. The observed EM data in the water column $B_{\rm EM}$ are compared with predicted values $B_{\rm CTD}$. Introducing the complex calibration parameters A and C yields

$$B_{\rm EM} = Q(A \cdot B_{\rm CTD} + C), \tag{A4}$$

we can rewrite this as follows:

$$B_{\rm EM} = F \cdot B_{\rm CTD} + D, \tag{A5}$$

with $F = Q \cdot A$ and $D = Q \cdot C$. The parameters F and D can be determined through linear regression for amplitude and phase separately. In the next step we used these calculated calibration parameters to determine B from the CTD conductivity and removed it from the EM data. Thereafter, the scattered EM field U is isolated and eq. (A1) reduces to

$$U_{\rm EM} = Q \cdot U_{\rm cal}, \tag{A6}$$

where $U_{\rm EM}$ is the measured EM scatter field and $U_{\rm cal}$ is the theoretical EM scatter field. To calculate the theoretical EM response of the seafloor from eq. (1), ground truth data are required. After $U_{\rm cal}$ is calculated the multiplicative calibration term Q can be determined in the same way as F and D.

Chapter 3

Determination of grain-size characteristics from electromagnetic seabed mapping data: A NW Iberian shelf study

Abstract

The electric conductivity and magnetic susceptibility of sediments are fundamental parameters in environmental geophysics. Both can be determined from marine electromagnetic profiling, a novel, fast and non-invasive seafloor mapping technique. Here we present statistical evidence that electric conductivity and magnetic susceptibility can help to determine physical grain-size characteristics (size, sorting and mud content) of marine surficial sediments. Electromagnetic data acquired with the bottom-towed electromagnetic profiler MARUM NERIDIS III were analysed and compared with grain-size data from 33 samples across the NW Iberian continental shelf. A negative correlation between mean grain size and conductivity ($R = -0.79$) as well as mean grain size and susceptibility ($R = -0.78$) was found. Simple and multiple linear regression analyses were carried out to predict mean grain-size, mud content and the standard deviation of the grain-size distribution from conductivity and susceptibility. The comparison of both methods showed that multiple linear regression models predict the grain-size distribution characteristics better than the simple models. This exemplary study demonstrates that electromagnetic benthic profiling is capable to estimate mean grain-size, sorting and mud content of marine surficial sediments at a very high significance level. Transfer functions can be calibrated using grains-size data from a few reference samples and extrapolated along shelf-wide survey lines. This study suggests that electromagnetic benthic profiling should play a larger role for coastal zone management, seafloor contamination and sediment provenance studies in worldwide continental shelf systems.

3.1 Introduction

Coastal and shelf regions belong to the most economically important as well as to the most environmentally stressed marine areas on earth. For both, the exploitation and the preservation of these areas, a detailed knowledge of the seabed composition has become increasingly important. The grain-size distribution is probably the most important textural attribute of marine sediments. It is conventionally determined by taking and analysing sediment samples, which is time consuming, expensive and limited in spatial coverage. To comply with the increasing demand on seabed information the development of remote techniques to predict grain-size characteristics and thus to reduce the number of seafloor sediment samples is vital. Acoustic systems, especially multi-beam echo-sounders (MBES), have been the methods of choice for remote shallow seabed exploration for the last decades. Mainly used for bathymetric measurements they are also powerful tools for sediment characterisation (e.g. Fonseca and Mayer 2007; Fonseca et al. 2009; Hellequin et al. 2003; Huang et al. 2012, 2013, 2014; Lamarche et al. 2011; Siemes et al. 2010). Nevertheless, the quantitative analysis of acoustic backscatter data is still challenging (Lamarche et al. 2011), especially the discrimination between sediment surface and volume processes. In contrast, electromagnetic (EM) data offer quantitative measures of bulk sediment properties. EM induction methods have been frequently used in the past to characterise soils and sediments on land because they permit a non-destructive, fast, and relatively inexpensive data acquisition. Therefore, the development of EM systems to investigate the seafloor has received increased attention over the past decades. Pioneering work was done by Cheesman et al. (1990) who developed one of the first towed marine EM systems to map the near-surface electrical conductivity. Evans (2001) validated porosities estimates derived from the same EM system through a comparison with core data. Müller et al. (2011) and Szpak et al. (2012) detected freshwater respectively gas seepage at marine pockmarks with EM systems. Swidinsky et al. (2012) investigated a transient central loop EM method for the exploration of massive sulphide deposits. Müller et al. (2012) developed an EM profiling technique using a frequency domain concentric EM sensor. The latter method has the advantage being able to recover the magnetic susceptibility of the seafloor in addition to the electric conductivity. They also showed that both parameters offer complementary information about the seafloor sediments. Based on these studies Baasch et al. (2015) provided calibration and inversion methods to simultaneously reconstruct electric conductivity and magnetic

susceptibility from marine EM data. In marine environments, the electric conductivity of sediment grains is generally negligible compared to the conductive saltwater in the pore space. Under such conditions, sediment electric conductivity can be considered as a function of pore-water content and tortuosity. In fully water-saturated sediments the water content corresponds to porosity. The conductivity-porosity relationship has been investigated for many years. Several empirical or semi-empirical formulas have been developed to describe this relation. The most common one is Archie's law (Archie 1942), given by $\sigma_s = 1/a \cdot \sigma_w \cdot \Phi^m$, where σ_s and σ_w are the electric conductivity of the sediment and the water, respectively, Φ is the porosity. Parameter a and exponent m account for permeability and compaction of the sediment and need to be empirically determined. The porosity itself depends on the sediment's closeness of packing, which is controlled by shape, compaction and sorting of the sediment particles (Rogers and Head 1961) and is hence related to the grain-size distribution. The magnetic susceptibility of water (typically -9×10^{-6}) is very small compared to that of sediment grains (typically between 10×10^{-5} and 10×10^{-3} for clastic marine sediments). Consequently, susceptibility is mainly controlled by the mineralogical composition of the sediment. Magnetic properties prove to correlate with grain size in many different environments and have been used as particle size proxy (e.g Booth et al. 2005; Oldfield et al. 1985). Ferrimagnetic iron minerals enrich particularly in the fine fraction of marine sediments due to their usually fine crystal size in their magmatic parent rocks and can hence be used as a proxy for terrigenous mud content (Müller et al. 2012). The above cited studies suggest that electric conductivity and magnetic susceptibility are suitable particle size proxies. However, no studies exist that combine electric conductivity and magnetic susceptibility data to predict textural sediment properties, neither on land nor in marine environments. To determine if such an approach is feasible we need to understand (1) which parameters influence the relationship between EM and textural sediment properties, (2) how these relationships vary for different sediment types and (3) whether multiple models combining conductivity and susceptibility predict textural properties better than models using only one of both parameters. We therefore investigate the relationship of EM and grain-size properties by correlation analyses between EM profiling data and surface samples collected at 33 different locations across the NW Iberian continental shelf. Three different statistical attributes are used to describe the grain-size distribution, namely mean grain-size, mud content and standard deviation as a measure of the sediment sorting. This selection is based on previous studies by Müller

et al. (2011, 2012) and Baasch et al. (2015) suggesting a linkage between EM data, mud content and sediment sorting.

3.1.1 Study area

The NW Iberian continental shelf extends over a 200-km-long and 30-50-km-wide area between Cape Finisterre 43°N) and the Douro River mouth 41°N. It is a typical example of a low accumulation non-glaciated clastic shelf system (Lantzsch et al. 2009a,b) seasonally exposed to high-energetic hydrodynamic conditions (Oberle et al. 2014b). Sediment transport and distribution of fine-grained fluviogenic sediments are controlled by winter storms, longshore currents and the geomorphology of the shelf. Additionally, anthropogenic activities, in particular bottom trawling and dredging (Oberle et al. 2016a,b), influence the sediment distribution on the NW Iberian shelf. Detailed descriptions of the general sedimentary setting can be found in e.g. Corredeira et al. (2009), Dias et al. (2002), and Lantzsch et al. (2010). One of the most prominent sediment features is a coast-parallel, 50-km-long and 2-3-km-wide mid-shelf mud depocentre (Dias et al. 2002). This so called 'Galicia Mud Belt' (Lantzsch et al. 2009b) was formed by re-suspended fine material originating from fluvial sediment input mainly from the Douro River. Recent studies suggest that 60 per cent of this fluvial material has been transported off-shelf (Oberle et al. 2014a). During transport, finer material accumulates in morphological traps (e.g. troughs of sediment dunes /ripples) along the pathways (Baasch et al. 2015). Lantzsch et al. (2010) applied a fuzzy c-means clustering technique on the results of a microscopic component analysis to define the main sediments facies. They described three facies classes, a mixed-sand facies, a glaucony-sand facies and a mud facies. The spatial distribution of these sediment facies is shown in Fig. 3.1. The mixed-sand facies consists mainly of carbonate microfossil fragments, quartz and mica (Lantzsch et al. 2010). The glaucony-sand facies is characterised by a high amount of up to 50 per cent paramagnetic glaucony (Odin and Lamboy 1988) and the mud facies has a high amount of mud (silt and clay) of up to 90 per cent at the centre of the Galicia Mud Belt. Acoustic and EM measurements showed that these main sediment facies merge in complex transition zones characterized by morphological driven and selective sediment transport (Baasch et al. 2015). It is due to these different sediment types, compositions and origins that this study area offers an adequate variety of sediments to test the EM-data-grain-size-relationship under different environmental conditions.

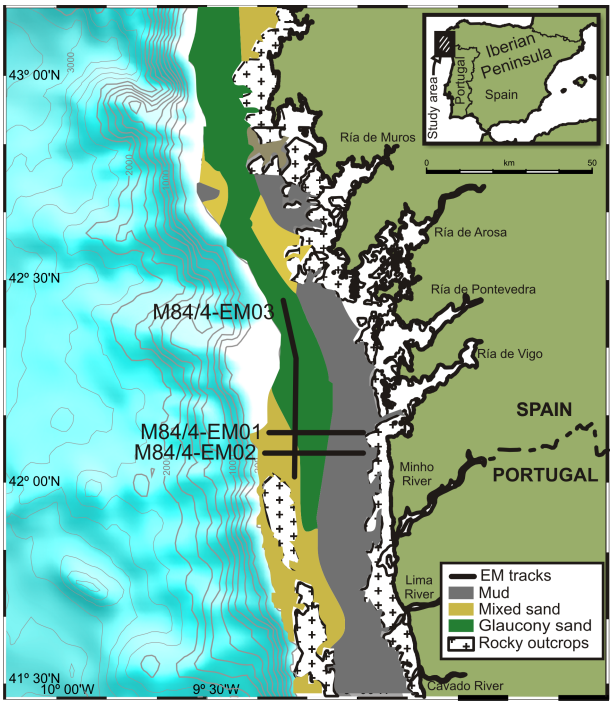

Figure 3.1: NW Iberian shelf. Colours indicate sediment facies, black lines indicate EM profiles from RV Meteor cruise M84/4b. Modified from Lantzsch et al. (2010).

3.2 Materials and methods

3.2.1 Grain-size analysis

Sediment samples were taken at 105 different locations across the NW Iberian shelf (Hanebuth et al. 2012) during the Meteor cruise M84/4. 33 of these locations fall directly onto the three here presented EM profiles. A Rumohr corer (100-cm-long gravity corer), a grab sampler and a box corer were used for the sampling. The recovered cores had a length between 10 cm and 70 cm depending on the coring device and sediment texture. The cores were sub-sampled every 10 cm to 20 cm based on visual inspection. grain-size analyses were carried out with the Coulter LS 200 laser particle seizer. The volume distribution was divided in 92 logarithmically spaced size classes ranging from 0.39 to 2000 μm. No particles larger than 2 mm (gravel) were present. The three following statistics of the grain-size distribution are used in this study:

- Geometric mean grain-size
- Geometric standard deviation

- Mud (clay and silt) content, i.e. the accumulated distribution of the grain-size classes ranging from 0.38 to 63.41 μm.

For the regression analyses mean grain size and standard deviation were converted into ϕ (phi) scale using the equations $\phi = \log_2([mean\ grain\ size\ in\ \mu m]/1000)$ and $\delta\phi = \log_2([standard\ deviation\ in\ \mu m])$, respectively. Note that here ϕ has an opposite sign compared to the standard inverted ϕ-scale (Wentworth 1922). Hence, a positive correlation with mean grain size means an increase of the respective variable with increasing mean grain size. The arithmetic mean for each statistical value was calculated from all samples at each location and used as representative value for the respective sample location.

3.2.2 Marine electromagnetic profiling

The principles of marine EM profiling are described by Müller et al. (2012) and Baasch et al. (2015) and will only be briefly dealt with in this paper. Here we use an EM data set which has been collected along three profiles across the NW Iberian shelf partially published by Baasch et al. (2015). The measurements were carried out with the new benthic EM Profiler MARUM-NERIDIS III (Baasch et al. 2015; Kulgemeyer et al. 2016). This system uses a frequency domain EMI sensor customized for near-surface coastal and marine sediment investigations. The EMI sensor is located in a non-conductive, non-magnetic profiler sled that is towed on the seafloor ensuring a constant distance between the sensor and the ground. The EMI sensor acquires continuous data along the ship track with a sampling rate of 25 Hz providing a very high spatial resolution. Measurements at up to ten different frequencies (five used for this study) enable a clear distinction between the conductivity and susceptibility related complex-valued earth response. Its imaginary part or quadrature component is mainly a measure of conductivity while magnetic susceptibility causes a frequency independent shift of the real part (in-phase component) as long as superparamagnetic particles can be ignored. The sensitivity of the in-phase component to conductivity decreases towards lower frequencies so that the in-phase component at very low frequencies is almost solely controlled by magnetic susceptibility. Calibration of the EM data follows the primary and secondary field calibration and inversion method given in Baasch et al. (2015), that can be summarized by the following steps: (1) Instrument related bias was removed by calibrating the EM data from water conductivity measured with a conductivity-temperature-depth (CTD) probe attached to the profiler and (2) from conductivity and susceptibility ground-truth data measured on the

collected sediment samples. Electric conductivity was measured with a hand-held direct current probe with miniaturized four-electrode-in-line Wenner configuration and 4 mm electrode spacing. Susceptibility was determined with a laboratory susceptometer. (3) A half-space inversion approach was used to recover electric conductivity and magnetic susceptibility from the EM data. Baasch et al. (2015) showed that inverting multifrequency EM data simultaneously for conductivity and susceptibility offers reliable results over a data range that is representative for most geological settings. The advantage of the simultaneous inversion is that it is more robust towards an inaccurate starting model than cascaded approaches. The drawback of simultaneous inversion is that different depth ranges are illuminated for conductivity and susceptibility. Under normal marine conditions, the depth of investigation for conductivity can be up to five times higher than for susceptibility. To overcome this issue we applied an additional inversion step. In the first step in-phase and quadrature values of all five frequencies were inverted simultaneously for conductivity and susceptibility. In the second step an inversion was performed separately for conductivity and susceptibility. Only the high frequency quadrature response was used to recover conductivity and the low-frequency in-phase response for susceptibility inversion incorporating the simultaneous inversion results as a priory information. The reconstructed conductivity and susceptibility data then represent the same depth range of a few tens of centimetres below the seafloor.

3.2.3 Regression analysis

Simple linear regression

Simple linear regression analyses were carried out for all combinations of the variables electric conductivity, magnetic susceptibility, mean grain size, mud content and standard deviation. The Pearson product-moment correlation coefficient (R) and the coefficient of determination (R^2) were used as a measure of the linear correlation between two variables and the goodness of fit between the measured and predicted data. Here, the coefficient of determination is the square of the correlation coefficient, because we only investigate univariate linear regressions. The significance of the correlations was investigated using F-tests studying the hypothesis that there is no linear regression relationship between the respective variables (e.g. Swan and Sandilands 1995). The corresponding p-values range from 0 to 1, where a p-value smaller than 0.05 indicates that the linear correlation is significant at the 5 per cent significance level.

Multiple linear regression

Multiple linear regression analysis was performed using conductivity σ and susceptibility κ together as predictor variables. The theoretical model is

$$\hat{y} = b_0 + b_\sigma \cdot \sigma + b_\kappa \cdot \kappa + \epsilon \ , \tag{3.1}$$

where the response variable $\hat{y}$ represents the grain-size property of interest (mean grain size, mud content and standard deviation), b_0, b_σ, b_κ represent the empirical regression model coefficients estimated by linear least squares and ϵ is an error term. The root-mean-square error (RMSE) and the coefficient of variation of the RMSE were used to measure the difference between the n observed and predicted values, y_i and $\hat{y}_i$, respectively. The coefficient of variation of the RMSE is defined as

$$\mathrm{CV(RMSE)} = \frac{\mathrm{RMSE}}{\bar{y}} = \frac{\sqrt{1/n \sum_i (y_i - \hat{y}_i)^2}}{\bar{y}} \ , \tag{3.2}$$

where $\bar{y}$ is the mean of the observed data. Note that for the calculation of the coefficient of variation the mean grain-size and standard deviation were back-transformed from ϕ-scale to μm, so that they can only take non-negative values. The adjusted coefficient of determination ($\bar{R}^2$) was calculated to compare the simple with multiple linear regressions. It is given by

$$\bar{R}^2 = \frac{\sum_i (y_i - \hat{y}_i)/(n-m-1)}{\sum_i (y_i - \bar{y})/(n-1)} \ , \tag{3.3}$$

where m is the number of predictor variables. Unlike the (unadjusted) coefficient of determination, the adjusted coefficient of determination accounts for the number of predictor variables and hence increases only if an extra added term improves the model more than any random term would do. The adjusted coefficient of determination is always smaller than or equal to the coefficient of determination.

3.3 Results and discussion

3.3.1 Grain-size analysis

For our studies we assigned each sediment sample to one of the three sediment facies defined by Lantzsch et al. (2010). Note, that this classification is solely based on the sample location and not on own sedimentological analyses. We therefore speak of Mud Area, Glaucony Sand Area and Mixed Sand Area to denominate the three sample groups according to the facies names in Lantzsch et al. (2010). The extents of

these areas are shown in Fig. 3.1. Grain-size measurements of the sediment samples reveal predominately homogeneous medium to coarse silts and fine sands with no or low content of coarse sands (Fig. 3.2). Sediments from the Mixed Sand Area on the outer shelf show unimodal sediment distributions with a distinct, narrow peak around the average mean grain size of 81.65 μm ($\phi = -3.16$). The standard deviation is generally small with an average of 3.56 μm ($\delta\phi = 1.83$). The analysis of Glaucony Sand Area sediments reveals mostly bi-modal sediment distributions with a higher peak in the medium sand fraction and a side peak in the silt fraction. The peak in the medium sand fraction can be attributed to relict sands and glaucony sands while the mud fraction most likely has been transported from the Mud Area. The mud content with an average of 50.85 volume per cent is two-times higher in the Glaucony Sand Area than in the Mixed Sand Area. The samples in the Mud Area have an average mud content of 75.32 per cent with highest values of over 90 per cent. The mean grain size is more than two-times smaller than in the Glaucony Sand Area. Tab. 3.1 summarises the average grain-size distribution characteristics for the different shelf areas.

Table 3.1: Grain-size distribution characteristics for the three different shelf areas. The values in brackets are converted to ϕ-scale.

	Mud Area (7 samples)	Glaucony Sand Area (19 samples)	Mixed Sand Area (7 samples)	Total (33 samples)
∅ Mean grain size [μm (ϕ)]	24.72 (-5.34)	56 (-4.16)	81.65 (-3.16)	54.78 (-4.19)
∅ Mud content [Vol. %]	75.32	50.85	23.78	50.3
∅ Standard deviation [μm (ϕ)]	3.59 (1.84)	5.04 (2.33)	3.56 (1.83)	4.47 (2.16)

3.3.2 Marine EM profiling

Electric conductivity and magnetic susceptibility obtained from half-space inversion of the EM data show relationships to mean grain size, mud content and standard deviation calculated from surface samples' grain-size distributions on all three profiles (Fig. 3.3). The granulometric data of profile M84/4-EM01 clearly show how mud content is increasing and mean grain size is decreasing from the outer shelf to the mid-shelf mud belt. The standard deviation is generally lower in the Mixed Sand Area on the outer shelf than on the mud belt. The magnetic susceptibility distinctly follows the main trend of the mud content with high values on the inner shelf (east) and the lowest values on the outer shelf (western) part. The electric conductivity is similarly related to the mud content in the Mud Area but shows an opposite relation on the outer shelf where mud content and standard deviation are low. In the Glaucony Sand Area,

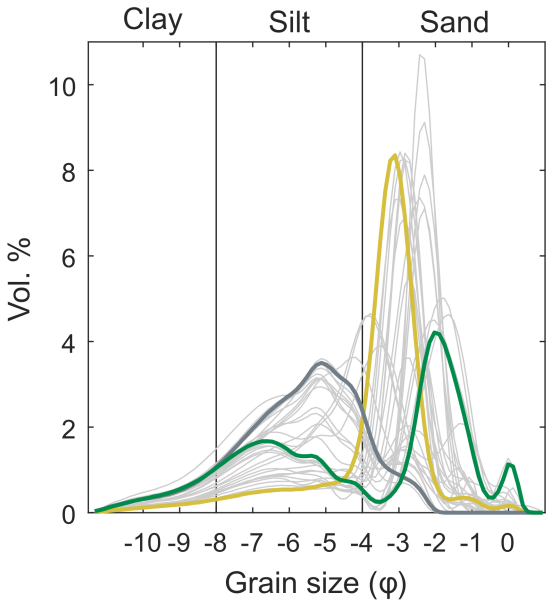

Figure 3.2: Grain-size distributions from the 33 surface samples. The thicker grey, green and yellow lines represent the grain-size distributions of cores 15649-1 (Mud Area), 15696-1 (Glaucony Sand Area) and 15634-1 (Mixed Sand Area), respectively. Note that the ϕ-scale here is inverted compared to the Wentworth ϕ-scale.

conductivity and susceptibility show inverse variations. This Glaucony Sand Area has characteristic sediment dune structures with 2-3 km wave lengths and comparably small elevations of less than 3 m. Müller et al. (2012) explained the high susceptibility and low conductivity at the crests by relatively higher paramagnetic glaucony content and higher compaction, hence lower porosity. Baasch et al. (2015) could show that the higher conductivity in the troughs correlates with higher mud content. The data from profile M84/4-EM02 show the same pattern as from profile M84/4-EM01, a general decrease of susceptibility from East to West with high conductivity in the Mud Area, the lowest conductivity at the western edge of the Glaucony Sand Area and moderate conductivity in the Mixed Sand Area on the outer shelf. Compared to Profile M84/4-EM01 the extension of the Glaucony Sand Area is smaller. Profile M84/4-EM03 runs in a North-South direction on the outer shelf parallel to the coast line crossing several morphological features. At the northern part in the Glaucony Sand Area, the rough seabed topography together with the very low conductivity suggests that only a very thin layer of recent sediments covers the bedrock. Peaks in susceptibility correspond with highs in the mud content (besides the northernmost sample) and low susceptibility with a higher sorting coefficient. Nevertheless, the moderate variations of the grain-size measures may not fully explain the significant susceptibility changes.

In this area, the paramagnetic glaucony controls the magnetic susceptibility in the absence of fine sediments from the mud-belt. Weakly magnetic mixed sand deposits in the troughs cause a serious drop in magnetic susceptibility, while the sediment porosity is only gently increasing between glaucony crests and mixed sand troughs. Towards the south profile M84/4-EM03 crosses a canyon. From the north to the south-end of the canyon's trough mean grain size is decreasing and conductivity is constantly increasing, whilst susceptibility is decreasing. This asymmetric sediment distribution across the canyon corresponds to the local hydrodynamic regime with a northward-directed sediment transport. Fine sediments are transported from the south and accumulate under hydrodynamically calmer conditions at the slip-off slope of the canyon (indicated by a slight bulge in the porosity curve). Sediments on the northern flank are characterized by glaucony sands that are indicative for a non-accumulating or erosional system caused by strong hydrodynamic forces. In the southernmost part conductivity and susceptibility values show little variance and are at the same data level as the mixed sand outer shelf sediments of cross-cutting profiles M84/4-EM01 and M84/4-EM02.

3.3.3 Linear regression analysis

Simple linear regression

The linear regression analyses were carried for all 33 sediment samples together as well as for each sediment facies area separately (Tab. 3.2). Taking all samples into account significant correlations were found between conductivity and all three grain-size measures mean grain size, mud content and standard deviation (Fig. 3.4). Conductivity correlates most strongly with standard deviation ($R = -0.79$) and mean grain size ($R = -0.79$) followed by mud content ($R = 0.68$). In contrast, susceptibility has the strongest correlation with mud content ($R = 0.85$) followed by mean grain size ($R = -0.78$). No correlation ($R = 0.1$) exists between susceptibility and standard deviation if all sample locations are taken into account. It can be seen that opposed trends exist for this relationship in the different facies areas (Fig. 3.4b, bottom). Analysing the facies areas separately reveals that the correlations between the different parameter vary substantially between facies areas. Conductivity and susceptibility show significant positive correlation in the Mud Area and Glaucony Sand Area. The highest correlation ($R = 0.84$) exists in the Mud Area where both conductivity and susceptibility strongly correlate with mud content and strongly negatively with mean grain size and standard deviation. Conductivity is negatively correlated ($R = -0.8$)

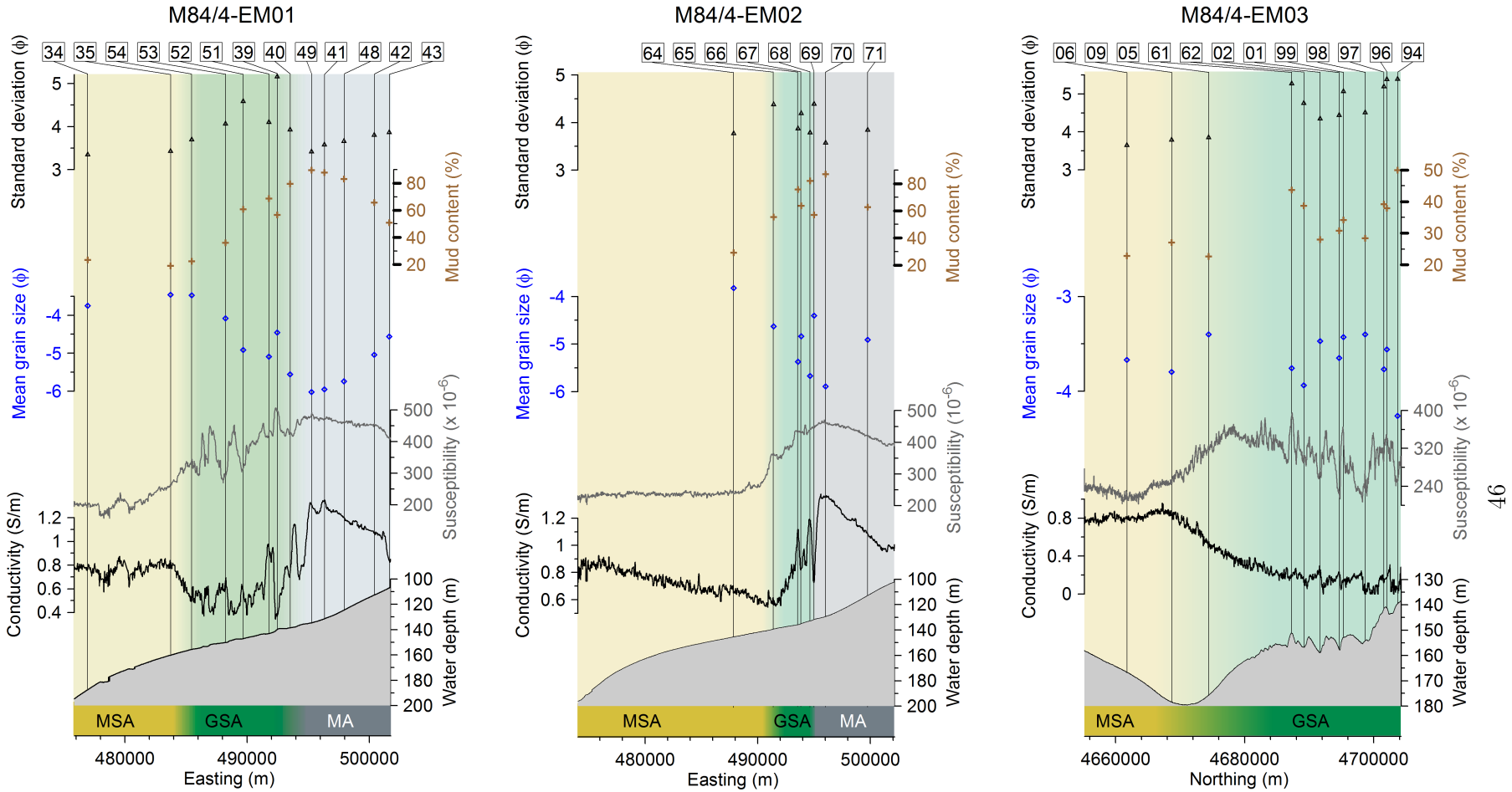

Figure 3.3: Electric conductivity (black line) and magnetic susceptibility (grey line) together with statistical grain-size distribution measures from surface samples of profiles M84/4-EM01 (left), M84/4-EM02 (middle) and M84/4-EM03 (right). Black triangles, brown crosses and blue diamonds indicate standard deviation, mud content and mean grain size, respectively. The background colours indicate particular sediment areas: Mud Area (MA), Glaucony Sand Area (GSA), Mixed Sand Area (MSA). Numbers on top represent the two last digits of the GeoB core coring sites.

to susceptibility in the Mixed Sand Area, where correlations across all attributes are generally weaker. It is also the only facies area with no significant correlations between conductivity and mean grain size ($R = -0.54$), conductivity and mud content ($R = 0.003$), as well as between susceptibility and mud content ($R = -0.26$). In contrast to the other areas, susceptibility correlates positively ($R = 0.77$) with mean grain size. This indicates the existence of para-magnetic glaucony minerals, which are often coarser than quartz grains (Odin and Lamboy 1988). There is no correlation between the standard deviation and any other attribute in the Mixed Sand Area. The Glaucony Sand Area, which lies spatially between the Mud Area and Mixed Sand Area, is also in terms of mean grain size and mud content in an intermediate position. There, the correlation between conductivity and susceptibility is the weakest of all three sediment facies ($R = 0.66$) but still significant ($p = 0.002$). According to that, conductivity and susceptibility correlate differently strong with the grain-size attributes. Conductivity correlates strongly with mean grain size (R = -0.88), mud content ($R = 0.85$) and standard deviation ($R = -0.8$) whereas a weaker correlation ($R = -0.65$) exists between susceptibility and mean grain size and no significant correlation ($R = -0.27$) is observed between susceptibility and standard deviation. The lower correlations between susceptibility and textural sediment properties in this area can be related to the abundance of glaucony minerals, which predominantly controls the sediment susceptibility in this area. Hence, this effect is masking the influence of clay content on susceptibility.

Multiple linear regression

In the multiple linear regression analyses conductivity and susceptibility were used simultaneously as predictor variables. The results show that strong significant correlations exist between the observed and predicted data for mean grain size, mud content and standard deviation in the Mud Area and Glaucony Sand Area (Tab. 3.3). Prediction of the grain-size parameters is most accurate in the Mud Area with RMSEs below 10 per cent of the mean values for each sediment parameter. In the Mixed Sand Area a relatively strong correlation can be found between observed and predicted mean grain size, however the corresponding p-value of 0.155 suggests that this correlation is insignificant. The predictive models for the two other parameters mud content and standard deviation are insignificant in the Mixed Sand Area. Nevertheless, the low RMSEs indicate that the coefficients of determination and the according F-tests underestimate the prediction capabilities of multiple linear regression models in this area due to the low variance of the grain-size parameters. It can be seen from the

Table 3.2: Correlation matrix showing the Pearson product-moment correlation coefficient (R) for electric conductivity (σ), magnetic susceptibility (κ), mean grain size (ϕ), mud content (MC) and standard deviation ($\delta\phi$). Italic type, bold type and italic and bold type combined indicate statistical significance, strong statistical significance and very strong statistical significance of the correlation, respectively.

	σ	κ	ϕ	MC	$\delta\phi$
			All 33 samples		
σ	1	***0.56***	***-0.79***	***0.68***	***-0.79***
κ	***0.56***	1	***-0.78***	***0.85***	-0.1
ϕ	***-0.79***	***-0.78***	1	***-0.98***	*0.38*
MC	***0.68***	***0.85***	***-0.98***	1	-0.2
$\delta\phi$	***-0.79***	-0.1	*0.38*	-0.2	1
			Mud Area (7 samples)		
σ	1	*0.84*	***-0.96***	***0.97***	*-0.86*
κ	*0.84*	1	**-0.91**	**0.91**	**-0.9**
ϕ	***-0.96***	**-0.91**	1	***-1***	**0.93**
MC	***0.97***	**0.91**	***-0.998***	1	**-0.92**
$\delta\phi$	*-0.86*	**-0.9**	**0.93**	**-0.92**	1
			Glaucony Sand Area (19 samples)		
σ	1	**0.66**	***-0.88***	***0.85***	***-0.8***
κ	**0.66**	1 (1)	**-0.65**	***0.75***	-0.27
ϕ	***-0.88***	**-0.65**	1	***-0.98***	**0.64**
MC	***0.85***	***0.75***	***-0.98***	1	*-0.53*
$\delta\phi$	***-0.8***	-0.27	**0.64**	*-0.53*	1
			Mixed Sand Area (7 samples)		
σ	1	*-0.8*	-0.54	0.003	-0.49
κ	*-0.8*	1	*0.77*	-0.26	0.54
ϕ	-0.54	*0.77*	1	*-0.79*	0.02
MC	0.003	-0.26	*-0.79*	1	0.53
$\delta\phi$	-0.49	0.54	0.02	0.53	1

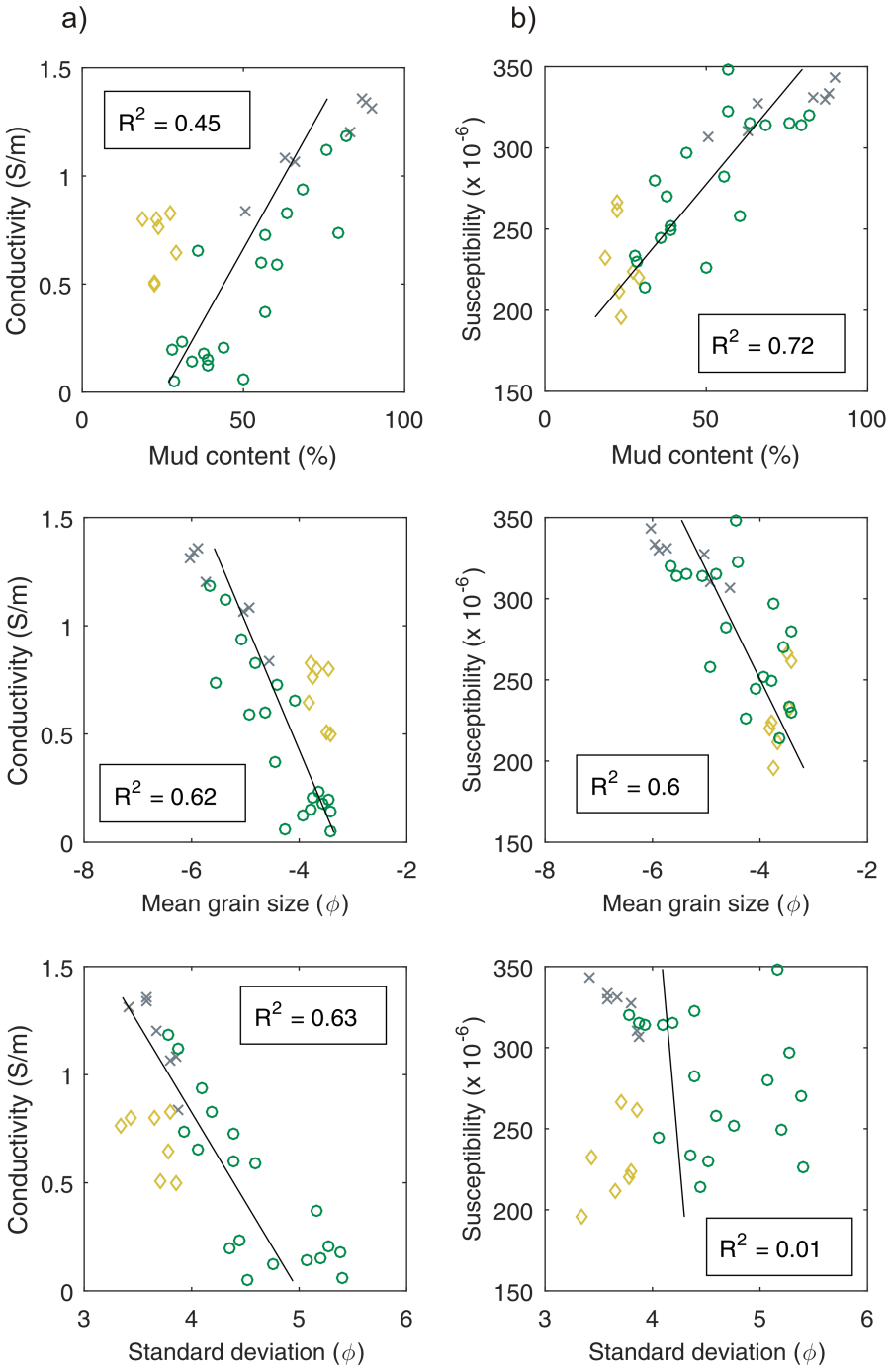

Figure 3.4: Conductivity (a) and susceptibility (b) versus grain-size data. Grey crosses, green circles and yellow diamonds indicate samples from the Mud Area, the Glaucony Sand Area and the Mixed Sand Area, respectively. Black lines represent the linear fits. Text boxes display the coefficient of determination (R^2).

regression coefficients (Tab. 3.3) that the linear models vary substantially between facies areas. This means that developing a model in a specific area only and then predicting grain-size properties from another area is likely to fail. In contrast, the global model (Fig. 3.5a), which takes all samples into account, shows a good fit for all three grain-size parameters. Nevertheless, a better fit could be achieved using a segmented regression combining the local models (Fig. 3.5b) determined for each facies area separately. Our analysis showed that the adjusted coefficients of determination of the multiple linear regression are generally higher than the coefficients of determination of the simple linear regression. This suggests that the multiple linear regression approach is superior regarding the grain-size attribute prediction.

3.4 Conclusions

EM profiling is a novel rapid geophysical method to measure the electric conductivity and magnetic susceptibility of the seabed. Both parameters can be used to differentiate and classify facies types of surficial shelf sediments. EM profiling data along three profiles across the NW Iberian shelf were analysed and compared with grain-size distributions of sediment samples from 33 locations. We have demonstrated that significant correlations exist between conductivity, susceptibility and the grain-size distribution characteristics mean grain size, mud content and standard deviation for sediments with a considerable amount of silt and clay (mud content $\geq$ 50 per cent). Our analyses suggest that the relationship between EM and grain-size characteristics is stronger in areas with high mud content and high sediment heterogeneity. We showed that the linear models obtained from multiple linear regression using conductivity and susceptibility together predict the grain-size distribution characteristics better than simple linear regression using either conductivity or susceptibility alone. Therefore, EM profiling methods measuring the electric conductivity and magnetic susceptibility simultaneously are better suited for sediment grain-size characterisation than methods which measure only one of the two properties. We also found out that the linear predictive models vary between sediment facies areas. We therefore suggest to use the EM data to classify or cluster the sediments first and then take sediment samples for all sediment classes accordingly. Clustering also allows to perform segmented linear regression creating predictive models for each cluster separately. Using such an approach, we could show that mean grain-size, sorting and mud content of marine surficial sediments can be predicted from benthic EM profiling at a very high significance level. However, to fully exploit the grain-size prediction capabilities of

Table 3.3: Statistics from the multiple regression analyses.

	Global model (33 samples)			Mud Area (7 samples)			Glaucony Sand Area (19 samples)			Mixed Sand Area (19 samples)			Local models (33 samples)		
	ϕ	MC	$\delta\phi$	ϕ	MC	$\delta\phi$	ϕ	MC	$\delta\phi$	ϕ	MC	$\delta\phi$	ϕ	MC	$\delta\phi$
b_0	-2.001	-21.041	4.056	0.648	-78.25	5.818	-3.155	10.291	4.228	-4.623	44.812	3.4024			
b_σ	-1.108	16.175	-1.64	-2.058	56.013	-0.307	-1.621	29.689	-1.596	0.252	-13.264	-0.217			
b_κ	-4661	1.69e05	3453	-8140	1.94e05	-3931	-1113	73930	3099	3163	-45416	1528			
R^2	0.783	0.772	0.809	0.958	0.971	0.855	0.785	0.786	0.758	0.606	0.181	0.305	0.905	0.922	0.883
Adjusted R^2	0.769	0.757	0.796	0.937	0.956	0.783	0.758	0.759	0.728	0.409	-0.229	-0.0423	0.898	0.917	0.876
p-value	1.09e-10	2.29e-10	1.63e-11	0.00177	0.000849	0.0209	4.58e-06	4.4e-06	1.16e-05	0.155	0.671	0.483	2.28e-17	1.04e-18	5.23e-16
RMSE	0.419	11.1	0.278	0.149	3.2	0.078	0.367	8.59	0.278	0.136	3.7	0.195	0.2649	6.216	0.207
CV(RMSE)	0.313	0.221	0.223	0.094	0.043	0.099	0.232	0.169	0.2	0.069	0.156	0.099	0.187	0.124	0.194

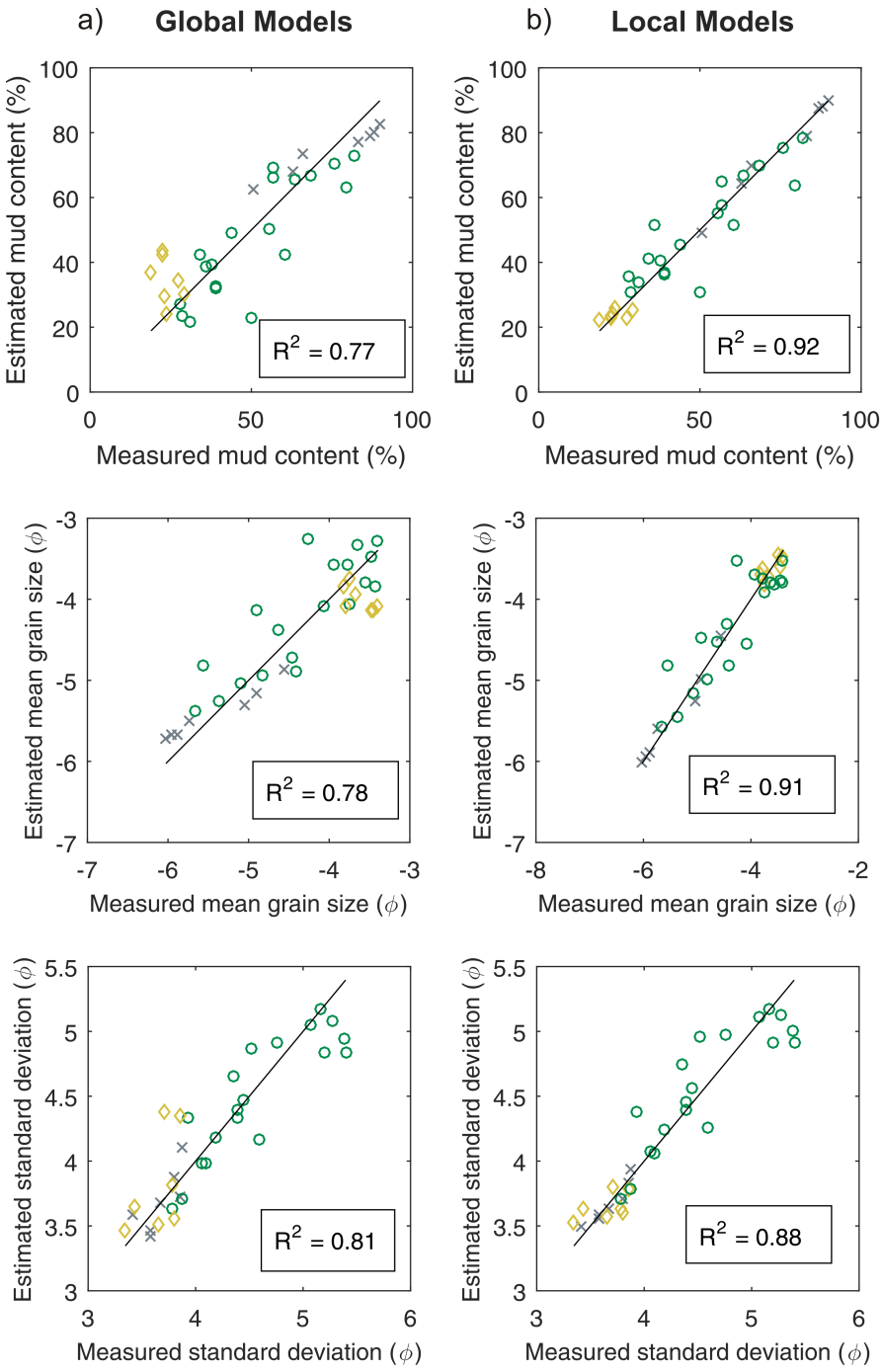

Figure 3.5: Comparison between the grain-size data prediction using global (a) and local (b) multiple linear regression models. Grey crosses, green circles and yellow diamonds indicate samples from the Mud Area, the Glaucony Sand Area and the Mixed Sand Area, respectively. The black line represents a trend with zero intercept and a slope of 1.

the EM data more sophisticated machine learning methods, such as decision trees,

artificial neuronal networks, supported vector machines etc., need to be investigated.

Acknowledgements

We would like to thank captain and crew of RV Meteor cruise M84/4. This work is funded through DFG-Research Center / Cluster of Excellence "The Ocean in the Earth System" and is part of MARUM Research Area SD investigating sediment dynamics between the coasts, shelves and continental slopes. BB would like to thank Inka Meyer for support in the grain-size analyses.

References

Archie, G. (1942). "The electrical resistivity log as an aid in determining some reservoir characteristics". In: *Petroleum Transactions of AIME* 146, pp. 54–62.

Baasch, B., H. Müller, F. K. J. Oberle, and T. von Dobeneck (2015). "Inversion of marine multifrequency electromagnetic profiling data: a new approach to resolve surficial sediment stratification". In: *Geophysical Journal International* 200.1, pp. 438–451. DOI: 10.1093/gji/ggu406.

Booth, C., J. Walden, A. Neal, and J. Smith (2005). "Use of mineral magnetic concentration data as a particle size proxy: A case study using marine, estuarine and fluvial sediments in the Carmarthen Bay area, South Wales, U.K." In: *Science of The Total Environment* 347.1 - 3, pp. 241–253. ISSN: 0048-9697. DOI: http://dx.doi.org/10.1016/j.scitotenv.2004.12.042.

Cheesman, S. J., R. N. Edwards, and L. K. Law (1990). "A test of a short-baseline sea-floor transient electromagnetic system". In: *Geophysical Journal International* 103.2, pp. 431–437. ISSN: 0956540X. DOI: 10.1111/j.1365-246X.1990.tb01782.x.

Corredeira, C., M. F. Araújo, A. Gouveia, and J.-M. Jouanneau (2009). "Sediments of Galician Continental Shelf: elemental composition and accumulation rates". In: *Journal of Radioanalytical and Nuclear Chemistry* 281.2, pp. 265–268. ISSN: 1588-2780. DOI: 10.1007/s10967-009-0106-7.

Dias, J. M. A., J. M. Jouanneau, R. Gonzalez, M. F. Araújo, T. Drago, C. Garcia, A. Oliveira, A. Rodrigues, J. Vitorino, and O. Weber (2002). "Present day sedimentary processes on the northern Iberian shelf". In: *Progress In Oceanography* 52.2-4, pp. 249–259. ISSN: 0079-6611. DOI: DOI:10.1016/S0079-6611(02)00009-5.

Evans, R. L. (2001). "Measuring the shallow porosity structure of sediments on the continental shelf: A comparison of an electromagnetic approach with cores and acoustic backscatter". In: *J. geophys. Res.* 106.C11, pp. 27047–27060. ISSN: 0148-0227.

Fonseca, L. and L. Mayer (2007). "Remote estimation of surficial seafloor properties through the application Angular Range Analysis to multibeam sonar data". In: *Marine Geophysical Researches* 28.2, pp. 119–126. ISSN: 0025-3235. DOI: 10.1007/s11001-007-9019-4.

Fonseca, L., C. Brown, B. Calder, L. Mayer, and Y. Rzhanov (2009). "Angular range analysis of acoustic themes from Stanton Banks Ireland: A link between visual interpretation and multibeam echosounder angular signatures". In: *Applied Acoustics* 70.10, pp. 1298–1304. ISSN: 0003682X. DOI: 10.1016/j.apacoust.2008.09.008.

Hanebuth, T., W. Alekseev, A. Andrade Grande, B. Baasch, K.-H. Baumann, P. Behrens, V. B. Bender, T. von Dobeneck, A. dos S. Marques, T. Frederichs, J. Haberkorn, H. J., C. Hilgenfeldt, J. Just, B. Kokisch, H. Lantzsch, A. Lenhart, A. Lipke, F. Lobo Sánchez, A. Neba Rodíguez, H. Müller, A. Pertovic, I. Rodríguez Germade, S. Roud, A. Schwab, T. Schwenk, I. Voigt, and S. Wenau (2012). "Report and preliminary results of RV Meteor cruise M84/4 GALIOMAR III. Vigo – Vigo, 1st – 28th May, 2011". In: *Berichte aus dem Fachbereich Geowissenschaften*. 283.

Hellequin, L., J.-M. Boucher, and X. Lurton (2003). "Processing of high-frequency multibeam echo sounder data for seafloor characterization". In: *IEEE Journal of Oceanic Engineering* 28.1, pp. 78–89. ISSN: 0364-9059. DOI: 10.1109/JOE.2002.808205.

Huang, Z., S. L. Nichol, J. P. Siwabessy, J. Daniell, and B. P. Brooke (2012). "Predictive modelling of seabed sediment parameters using multibeam acoustic data: a case study on the Carnarvon Shelf, Western Australia". In: *International Journal of Geographical Information Science* 26.2, pp. 283–307. DOI: 10.1080/13658816.2011.590139.

Huang, Z., J. Siwabessy, S. Nichol, T. Anderson, and B. Brooke (2013). "Predictive mapping of seabed cover types using angular response curves of multibeam backscatter data: Testing different feature analysis approaches". In: *Continental Shelf Research* 61-62, pp. 12–22. ISSN: 0278-4343. DOI: http://dx.doi.org/10.1016/j.csr.2013.04.024.

Huang, Z., J. Siwabessy, S. L. Nichol, and B. P. Brooke (2014). "Predictive mapping of seabed substrata using high-resolution multibeam sonar data: A case study from a shelf with complex geomorphology". In: *Marine Geology* 357, pp. 37–52. ISSN: 0025-3227. DOI: http://dx.doi.org/10.1016/j.margeo.2014.07.012.

Kulgemeyer, T., T. von Dobeneck, H. Müller, K. R. Bryan, W. P. de Lange, and C. N. Battershill (2016). "Lithofacies distribution and sediment dynamics on a storm-dominated shelf from combined photographic, acoustic and sedimentological profiling methods (Bay of Plenty, New Zealand)". In: *Marine Geology* 376, pp. 158–174. ISSN: 0025-3227. DOI: http://dx.doi.org/10.1016/j.margeo.2016.03.005.

Lamarche, G., X. Lurton, A.-L. Verdier, and J.-M. Augustin (2011). "Quantitative characterisation of seafloor substrate and bedforms using advanced processing of multibeam backscatter - Application to Cook Strait, New Zealand". In: *Continental Shelf Research* 31.2, Supplement. Geological and Biological Mapping and Characterisation of Benthic Marine Environments, S93–S109. ISSN: 0278-4343. DOI: http://dx.doi.org/10.1016/j.csr.2010.06.001.

Lantzsch, H., T. J. Hanebuth, and V. B. Bender (2009a). "Holocene evolution of mud depocentres on a high-energy, low-accumulation shelf (NW Iberia)". In: *Quaternary Research* 72.3, pp. 325–336. ISSN: 00335894. DOI: 10.1016/j.yqres.2009.07.009.

Lantzsch, H., T. J. Hanebuth, V. B. Bender, and S. Krastel (2009b). "Sedimentary architecture of a low-accumulation shelf since the Late Pleistocene (NW Iberia)". In: *Marine Geology* 259.1-4, pp. 47–58. ISSN: 00253227. DOI: 10.1016/j.margeo.2008.12.008.

Lantzsch, H., T. J. Hanebuth, and R. Henrich (2010). "Sediment recycling and adjustment of deposition during deglacial drowning of a low-accumulation shelf (NW Iberia)". In: *Continental Shelf Research* 30.15, pp. 1665–1679. ISSN: 02784343. DOI: 10.1016/j.csr.2010.06.013.

Müller, H., T. von Dobeneck, W. Nehmiz, and K. Hamer (2011). "Near-surface electromagnetic, rock magnetic, and geochemical fingerprinting of submarine freshwater seepage at Eckernförde Bay (SW Baltic Sea)". English. In: *Geo-Marine Letters* 31.2, pp. 123–140. ISSN: 0276-0460. DOI: 10.1007/s00367-010-0220-0.

Müller, H., T. von Dobeneck, C. Hilgenfeldt, B. SanFilipo, D. Rey, and B. Rubio (2012). "Mapping the magnetic susceptibility and electric conductivity of marine surficial sediments by benthic EM profiling". In: *Geophysics* 77.1, E43–E56. ISSN: 0016-8033. DOI: 10.1190/geo2010-0129.1.

Oberle, F. K., T. J. Hanebuth, B. Baasch, and T. Schwenk (2014a). "Volumetric budget calculation of sediment and carbon storage and export for a late holocene mid-shelf mudbelt

system (NW Iberia)". In: *Continental Shelf Research* 76.0, pp. 12–24. ISSN: 0278-4343. DOI: http://dx.doi.org/10.1016/j.csr.2013.12.012.

Oberle, F. K., C. D. Storlazzi, and T. J. Hanebuth (2014b). "Wave-driven sediment mobilization on a storm-controlled continental shelf (Northwest Iberia)". In: *Journal of Marine Systems* 139, pp. 362–372. ISSN: 0924-7963. DOI: http://dx.doi.org/10.1016/j.jmarsys.2014.07.018.

Oberle, F. K., P. W. Swarzenski, C. M. Reddy, R. K. Nelson, B. Baasch, and T. J. Hanebuth (2016a). "Deciphering the lithological consequences of bottom trawling to sedimentary habitats on the shelf". In: *Journal of Marine Systems* 159, pp. 120–131. ISSN: 0924-7963. DOI: http://dx.doi.org/10.1016/j.jmarsys.2015.12.008.

Oberle, F. K., C. D. Storlazzi, and T. J. Hanebuth (2016b). "What a drag: Quantifying the global impact of chronic bottom trawling on continental shelf sediment". In: *Journal of Marine Systems* 159, pp. 109–119. ISSN: 0924-7963. DOI: http://dx.doi.org/10.1016/j.jmarsys.2015.12.007.

Odin, G. and M. Lamboy (1988). "Glaucony From The Margin off Northwestern Spain". In: *Green Marine Clays*. Ed. by G. Odin. Elsevier, pp. 249–275. DOI: http://dx.doi.org/10.1016/S0070-4571(08)70067-0.

Oldfield, F., B. A. Maher, J. Donoghue, and J. Pierce (1985). "Particle-size related, mineral magnetic source sediment linkages in the Rhode River catchment, Maryland, USA". In: *Journal of the Geological Society* 142.6, pp. 1035–1046. DOI: 10.1144/gsjgs.142.6.1035.

Rogers, J. J. W. and W. B. Head (1961). "Relationships between porosity, median size, and sorting coefficients of synthetic sands". In: *Journal of Sedimentary Research* 31.3, pp. 467–470. ISSN: 1527-1404. DOI: 10.1306/74D70BA5-2B21-11D7-8648000102C1865D.

Siemes, K., M. Snellen, A. R. Amiri-Simkooei, D. G. Simons, and J. P. Hermand (2010). "Predicting Spatial Variability of Sediment Properties From Hydrographic Data for Geoacoustic Inversion". In: *IEEE Journal of Oceanic Engineering* 35.4, pp. 766–778. ISSN: 0364-9059. DOI: 10.1109/JOE.2010.2066711.

Swan, A. and M. Sandilands (1995). *Introduction to Geological Data Analysis*. Wiley. ISBN: 9780632032242.

Swidinsky, A., S. Hölz, and M. Jegen (2012). "On mapping seafloor mineral deposits with central loop transient electromagnetics". In: *Geophysics* 77.3, E171–E184. DOI: 10.1190/geo2011-0242.1.

Szpak, M. T., X. Monteys, S. O'Reilly, A. J. Simpson, X. Garcia, R. L. Evans, C. C. R. Allen, D. J. McNally, D. Courtier-Murias, and B. P. Kelleher (2012). "Geophysical and geochemical survey of a large marine pockmark on the Malin Shelf, Ireland". In: *Geochemistry, Geophysics, Geosystems* 13.1. Q01011. ISSN: 1525-2027. DOI: 10.1029/2011GC003787.

Wentworth, C. K. (1922). "A Scale of Grade and Class Terms for Clastic Sediments". In: *The Journal of Geology* 30.5, pp. 377–392. DOI: 10.1086/622910.

Chapter 4

Predictive modelling of grain-size distributions from marine electromagnetic profiling data using end-member analysis and a radial basis function network

Abstract

In this work we present a new methodology to predict grain-size distributions from geophysical data. Specifically, electric conductivity and magnetic susceptibility of seafloor sediments recovered from electromagnetic profiling data are used to predict grain-size distributions along shelf-wide survey lines. Field data from the NW Iberian shelf are investigated and reveal a strong relation between the electromagnetic properties and grain-size distribution. The here presented workflow combines unsupervised and supervised machine learning techniques. Nonnegative matrix factorisation is used to determine grain-size end-members from sediment surface samples. Four end-members were found which well represent the variety of sediments in the study area. A radial-basis function network modified for prediction of compositional data is then used to estimate the abundances of these end-members from the electromagnetic properties. The end-members together with their predicted abundances are finally back transformed to grain-size distribution. A minimum spatial variation constraint is implemented in the training of the network to avoid overfitting and to respect the spatial distribution of sediment patterns. The predicted models are tested via leave-one-out cross-validation revealing high prediction accuracy ($0.76 \leq R^2 \leq 0.89$). The predicted grain-size distributions represent the well-known sediment facies and patterns on the NW Iberian shelf and give new insights into their distribution, transition and dynamics. This study suggests that electromagnetic benthic profiling in combination with machine learning techniques is a powerful tool to estimate grain-size distribution of marine sediments.

4.1 Introduction

Coastal and shelf areas as transition zone between land and ocean play an important economic role in modern societies, which is reflected in the increasing development of ports, wind farms, oil rigs, pipelines, cable routes etc. For the planning, construction and maintenance of these marine infrastructures accurate information on shallow marine sediments is needed.

The grain-size distribution (GSD) plays a decisive role in terms of sediment characterisation, influencing most of the sediment's physical properties and behaviour. Therefore, its spatial distribution is of high interest for researchers and engineers. Traditional sampling methods to determine grain size (GS) are time-consuming and labour-intensive. This led to an increased interest in fast and less expensive remote seafloor characterisation techniques.

Acoustic methods such as multibeam echo-sounders are the most cost-effective tools to map large seabed areas (Brown et al. 2011). However, acoustic sediment characterisation is still challenging because of the complex relation between the acoustic backscatter and the seabed characteristics. A major remaining issue is the separation of seafloor roughness from sediment properties (e.g. D. R. Jackson and Briggs 1992).

In recent years, electromagnetic methods have been employed as a complementary tool for the estimation of marine sediment properties. Initially developed to investigate deep tectonic features and hydrocarbon reservoirs marine electromagnetic methods have been more and more applied to survey marine near surface sediments (Butler 2009). Most of these systems are designed to recover the electric conductivity (EC) of the seafloor (e.g. Cheesman et al. 1990; Evans 2001; Schwalenberg et al. 2010; Swidinsky et al. 2015) which can be linked to sediment porosity (Archie 1942) and GS (e.g. P. D. Jackson et al. 1978). Müller et al. (2012) developed a frequency domain central loop electromagnetic method for marine applications capable to provide information about magnetic susceptibility (MS) in addition to EC. Magnetic properties have been used as particle size proxy in many different environments (e.g. Booth et al. 2005; Oldfield et al. 1985). Recently, Baasch et al. (2016) showed that MS and EC correlate with mean GS, mud content and sorting of marine sediments and gave evidence that combining both electromagnetic parameters improves the accuracy of GS predictions.

The common problem of all seafloor sensing techniques is how to convert the measured geophysical parameters to qualitative or quantitative sediment characteristics. In seabed as well as terrestrial land cover mapping unsupervised techniques have

been previously used to create attribute classes and maps from geophysical and remote sensing data which could then be linked to geology by means of ground-truth samples (e.g. De and Chakraborty 2009; Eberle et al. 2015; Paasche et al. 2006). More recently supervised techniques based on machine learning became popular for predictive modelling of marine sediment (e.g. Diesing and Stephens 2015; Huang et al. 2012, 2013, 2014). In this case, the models are trained by ground-truth data and then used to predict seafloor properties for the whole survey area.

Previous efforts to predict GS from geophysical data aimed to estimate only fractions of the GSD, e.g. Gravel (%), sand (%), mud (%), mean GS (e.g. Baasch et al. 2016; Heil and Schmidhalter 2012; Huang et al. 2012). Independent prediction of single fractions of the GSD may reveal misleading results because of the compositional character of the GSD. Since the frequencies of the GSD components sum to constant no single GS fraction is free to vary separately from the rest of the total composition. Hence, the prediction of just one or a few GS fractions will always be biased by the remaining fractions. The best solution to overcome this problem is to predict the entire GSD. Following this idea we present a new methodology to predict compositional data from geophysical survey data. Specifically, we predict GSD from electromagnetic profiling data. The training GSDs used for our studies are derived from core samples and contain 92 logarithmically spaced GS classes from 0.38 μm to 2000 μm. Many of these GS classes are insufficiently populated or their abundances do net vary significantly between sediment samples and hence do not carry useful information. It is therefore desirable to reduce the number of predicted variables to the minimum amount necessary to describe the variability of the GSD. In order to achieve this, we employ a low-rank approximation namely a nonnegative matrix factorization (NMF) approach that determines GSD end-members. The aim is then to predict the abundances of these end-members from the electromagnetic data along the survey profiles. The prediction is done by a radial basis function network (RBFN) optimised for prediction of compositional data. The predicted GSD end-member abundances can finally be back transformed to GSD. The here presented workflow to predict GSD from electromagnetic profiling data can be summarised as follows:

1. EC and MS are recovered through inversion of corrected and calibrated electromagnetic profiling data.

2. End-member modelling is applied to the GSDs of sediment samples to reconstruct independent end-members with characteristic GSDs.

3. The relationship between EC, MS and the abundance of each GSD end-member is modelled using a radial basis-function network (RBFN) trained by the EC, MS (input variables) and end-member abundances (output variables) at the sample locations.

4. The established model is then used to predict end-member abundances for each data point along the survey profiles.

5. Finally, a complete GSD for each electromagnetic data point can be reconstructed using the end-members' GSDs and their predicted abundances.

Applying this approach we reconstructed GSDs along three profiles on the NW Iberian shelf validating the potential of electromagnetic profiling for quantitative sediment characterisation.

4.2 Methodology

4.2.1 End-member modelling

In the following we assume that the seafloor sediments are a simple mixture of different sediment types (end-members) and that the GSDs of the sediment samples can be expressed as a linear combination of the GSDs of the end-members. The aim of the end-member unmixing is then to unravel the number of end-members and their compositions (GSDs) from the GSDs of the sediment samples. The mixing model can be written in algebraic form as

$$\mathbf{X} = \mathbf{AS} \ , \tag{4.1}$$

where $\mathbf{X}$ is the $N \times M$ data matrix of M samples and N GS classes. The $L \times M$ matrix $\mathbf{S}$ denotes the frequencies of the N GS classes in the L end-members and $\mathbf{A}$ is a $N \times L$ matrix representing the abundances of the L end-members in each of the M samples. To factor $\mathbf{X}$ in $\mathbf{A}$ and $\mathbf{S}$ we use an unsupervised unmixing approach based on a NMF algorithm using an alternating least squares (ALS) technique. The basic idea of the ALS algorithms is to solve each of the factors $\mathbf{A}$ and $\mathbf{S}$ alternately while keeping the other factor constant (Paatero and Tapper 1994). In the simplest ALS algorithm (e.g. Berry et al. 2006) the matrix $\mathbf{A}$ is initialised first with a random matrix before $\mathbf{S}$ is computed from $\mathbf{X}$ and $\mathbf{A}$ via a simple least-square operation. After the least squares computation of $\mathbf{S}$ all its negative elements are set to zero. Subsequently, $\mathbf{A}$ is computed in the same way from $\mathbf{X}$ and $\mathbf{S}$ and finally all negative

elements in **A** are set to zero, too. The computation of **S** and **A** is repeated until the maximum number of iterations is reached. This simple ALS algorithm is very fast and does not lock elements when they become zero (locking phenomenon), as especially NMF techniques of the multiplicative update class do. Due to the limited number of sediment samples and GS classes, the matrices **A** and **S** are relatively small compared to other disciplines such as e.g. text mining or image processing. Therefore, we can afford a computational more expensive technique than the simple ALS algorithm. Instead of using an ad-hoc enforcement of nonnegativity, we use the nonnegative least squares (NNLS) algorithm of Lawson and Hanson (1995) that properly enforces nonnegativity and is known to converge to a local minimum. We also normalise **S** and **A** in each iteration such that their row-elements sum to one, which is an inherent constraint for compositional data. The method described above offers reliable results without any preconditioning of the data. The number of end-members included in the final mixing model can be found via principle component analysis, goodness-of-fit tests or a-priori knowledge. In general, the goal is to keep the number of components low while maintaining a reasonably good approximation of the input data (Just et al. 2012).

4.2.2 Radial basis function network

A RBFN is a machine learning method belonging to the class of artificial neural networks which uses a radial basis function (RBF) as activation function. RBFNs are used for function approximation, data interpolation or smooth fitting of data. A RBFN generally consists of three layers (Broomhead and Lowe 1988). The first layer is the input layer which only transfers the data to the next layer. The second layer is a hidden layer with a non-linear RBF, the so-called activation function. The third layer is a linear output layer. Its output is given by

$$\hat{y}(\mathbf{x}) = \sum_{i=1}^{M} w_i \varphi\left(\|\mathbf{x} - \mathbf{c}_i\|\right) + p(\mathbf{x}) \ , \tag{4.2}$$

where $\mathbf{x}$ is the input vector, $\varphi\left(\|\mathbf{x}\|\right)$ a RBF, where $\|\cdot\|$ denotes the Euclidean norm, w_i is the weight corresponding to the ith center $\mathbf{c}_i$, a vector of the same size as $\mathbf{x}$, and $p(\mathbf{x})$ is an optional polynomial of low degree, which can be included to model global trends of the data (Billings et al., 2002) and thus enhancing the extrapolation performance of the RBFN. Because of its simple form, smoothness and other advantages the RBF in eq. (4.2) is commonly a Gaussian function. The disadvantage of the Gaussian function is that the spread parameter which controls

the width of the RBF needs to be carefully chosen. If the data density of the input variables is non-uniform, a proper selection of this parameter might be difficult or even impossible. In contrast, a thin-plate spline is a scale independent RBF and thus handles better varying data density (Billings et al. 2002). It is therefore chosen as activation function for our RBFN. A thin-plate spline is a special polyharmonic spline of the form:

$$\varphi\left(\|\mathbf{x}\|\right) = \|\mathbf{x}\|^2 \ln\left(\|\mathbf{x}\|\right) \ . \tag{4.3}$$

Let us now consider the case in which the input to the network is the MS and EC data obtained from the inversion of the electromagnetic profiling data and the output is the abundance of the sediment GSD end-members (Fig. 4.1).

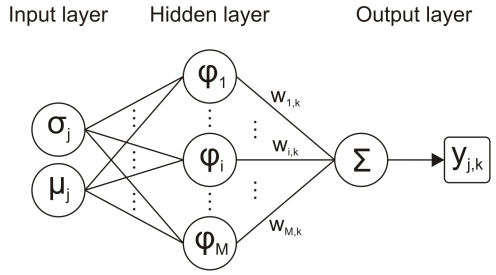

Figure 4.1: RBFN network structure. The jth input layer contains normalised EC and MS values from the jth electromagnetic profiling data point, in the hidden layer EC and MS from the jth data point are connected to EC and MS from the M centres. The output is the abundance of the kth end-member at jth electromagnetic data point.

The input vector elements are normalised to zero mean and unit variance in order to calculate the Euclidean norm in the RBFN's hidden layer. The set of input vectors then have the form $\mathbf{x}_j = \begin{bmatrix} \sigma_j \\ \mu_j \end{bmatrix} (j = 1, \ldots, N)$ with σ_j and μ_j the normalised EC respectively MS values of the jth data point. In this paper a linear polynomial is added to RBF in the hidden layer so that eq. (4.2) can be written as

$$\hat{y}_{j,k}(\mathbf{x}_j) = \sum_{i=1}^{M} w_{i,k} \varphi\left(\|\mathbf{x}_j - \mathbf{c}_i\|\right) + \mathbf{v}_k^T \begin{bmatrix} 1 \\ \mathbf{x}_j \end{bmatrix} \ , \qquad i = 1, 2, \ldots, M,$$
$$j = 1, 2, \ldots, N, \quad k = 1, 2, \ldots, L, \tag{4.4}$$

where $\hat{y}_{j,k}$ is an approximation of the abundance of the kth GS end-member at the jth data point, $w_{i,k}$ links the ith hidden neuron with the kth output neuron

and $\mathbf{v}_k^T = [v_{1,k}, v_{2,k}, v_{3,k}]$ contains the three weights of the linear polynomial at the kth output neuron. The number of output neurons L represents the number of end-members. The centres c_i were chosen to be the normalised EC and MS values at the ith sediment sample location. Theoretically, the training of the RBFN then only involves the estimation of the weights in the output layer. This can be obtained by solving the symmetric, linear system of equations

$$\begin{bmatrix} \boldsymbol{\varphi}_t & \mathbf{C}^T \\ \mathbf{C} & \mathbf{0} \end{bmatrix} \begin{bmatrix} \mathbf{w}_k \\ \mathbf{v}_k \end{bmatrix} = \begin{bmatrix} \mathbf{y}_k \\ \mathbf{0} \end{bmatrix} , \tag{4.5}$$

for each end-member separately, where $\varphi_{j,i} = (\|\mathbf{c}_j - \mathbf{c}_i\|)\,(i = 1, \ldots, M, \quad j = 1, \ldots, M)$ are the components of $\boldsymbol{\varphi}_t$, $\mathbf{C} = \begin{bmatrix} 1 & \cdots & 1 \\ \mathbf{c}_1 & \cdots & \mathbf{c}_M \end{bmatrix}$ and $\mathbf{w}_k$, $\mathbf{v}_k$ are the vectors of weights and $\mathbf{y}_k$ contains the abundances of the kth GSD end-member obtained from the M sediment samples. Eq. (4.5) also fulfils the orthogonality conditions $\sum_{i=1}^{M} w_{i,k} = 0$ and $\sum_{i=1}^{M} w_{i,k}\mathbf{c}_i = \begin{bmatrix} 0 \\ 0 \end{bmatrix}$. Since the number of centres equals the number of input vectors the misfit between the observed and the predicted data will be zero. Considering that the data is contaminated by noise, there is little reason to exactly fit the data. In contrast, it may be desired that the output meets some constraints based on a-priori information. For our analysis it can be assumed that the noise in the electromagnetic data has a higher spatial variation than the signal. Therefore, we included a minimum variation term in the training process, which penalises variations of the predicted end-member abundances of adjacent electromagnetic measurement points. Another reasonable constraint is that the predicted end-member abundances at each data point are positive and sum to one. The sum-to-one constraint requires that the RBFNs of the L end-member abundances are trained together. The training of the weights may then be expressed by a linear least-square problem of the form

$$\min_{\mathbf{u}} \quad \frac{1}{2} \|\boldsymbol{\Phi}_t \mathbf{u} - \mathbf{d}\|_2^2 + \frac{\lambda^2}{2} \|\mathbf{R}\boldsymbol{\Phi}_d \mathbf{u}\|_2^2 , \tag{4.6}$$

such that:

$$\hat{y}_{j,k} \geq 0 \ , \tag{4.7}$$

$$\sum_{k=1}^{L} \hat{y}_{j,k} = 1 \ , \quad j = 1, \ldots, N \tag{4.8}$$

$$\sum_{i=1}^{M} w_{i,k} = 0 \ , \tag{4.9}$$

$$\sum_{i=1}^{M} w_{i,k} \mathbf{c}_i = \begin{bmatrix} 0 \\ 0 \end{bmatrix} \ . \tag{4.10}$$

The first term in eq. (4.6) is a measure of the data misfit, where

$$\mathbf{\Phi}_t = \begin{bmatrix} \boldsymbol{\varphi}_t \mathbf{C}^T & \cdots & 0 \\ \vdots & \ddots & \vdots \\ 0 & \cdots & \boldsymbol{\varphi}_t \mathbf{C}^T \end{bmatrix} \ ,$$

a $(M \cdot L) \times (M \cdot L + 2)$ matrix containing the RBFs of the training data and the centres. The second term contains the minimum variation penalty function, where

$$\mathbf{\Phi}_d = \begin{bmatrix} \boldsymbol{\varphi}_d \mathbf{C}^T & \cdots & 0 \\ \vdots & \ddots & \vdots \\ 0 & \cdots & \boldsymbol{\varphi}_d \mathbf{C}^T \end{bmatrix} \ ,$$

a $(N \cdot L) \times (N \cdot L + 2)$ matrix and $\varphi_{j,i} = \varphi(\|\mathbf{x}_j - \mathbf{c}_i\|)(i = 1, \ldots, M, \quad j = 1, \ldots, N)$ are the components of $\boldsymbol{\varphi}_d$, namely the RBFs connecting each input value with each centre. The vector $\mathbf{u} = \left[\mathbf{w}_1^T, \mathbf{v}_1^T, \ldots, \mathbf{w}_L^T, \mathbf{v}_L^T\right]^T$ contains the weights and hence is subject of the training process and $\mathbf{d} = \left[\mathbf{y}_1^T, \ldots, \mathbf{y}_L^T\right]^T$. The regularisation parameter λ controls the trade-off between minimising the prediction error and the spatial variation of the output. The Matrix $\mathbf{R}$ is a first order finite difference operator. Note that the smoothness constraint is applied to the output data in the spatial domain, namely along the acquisition sail line, rather than in the feature space, which is in our case the MS-EC-plane. The constrained linear least-squares problem described in eqs. (4.6) to (4.10) was solved using the MATLAB optimization toolbox (MATLAB R2015b).

4.3 NW Iberian shelf study

4.3.1 Study area and sedimentary settings

The NW Iberian shelf is a classic example of a low accumulation non-glaciated clastic shelf system (Lantzsch et al. 2009a,b). Its extension reaches from Cape Finisterre in the north (43°N) to the Douro River mouth in the south (41°N). The width of the shelf is relatively narrow increasing from 30 km in the north to 50 km in the south. The shelf break occurs at a water depth of 160-200 m. Sediment transport, deposition and erosion is controlled by riverine discharge, winter storms, longshore currents and the geomorphology of the shelf (e.g. Oberle et al. 2014a,b; Oliveira et al. 2002), as well as anthropogenic activities, in particular bottom trawling and dredging (Oberle et al. 2016a,b). One of the most prominent sedimentary features is the 'Galicia Mud Belt (GMB)' (Lantzsch et al. 2009b), a well-defined 50-km-long and 2-3-km-wide coast-parallel mud depocentre (Dias et al. 2002). The GMB is located mid-shelf, north of the Minho River estuary at 110-120 m water depth. It is made up of 90 per cent fluviogenic silty and clayey material mainly originating from the Douro River (Dias et al. 2002). Seawards the GMB is boarded by glaucony sands consisting of up to 50 per cent paramagnetic glaucony (Odin and Lamboy 1988). On the outer shelf, very fine to fine sands predominate, which consist mainly of carbonate microfossil fragments, quartz and mica (Lantzsch et al. 2010, Fig. 4.2). Previous electromagnetic surveys in this area showed that the main sediment facies could be identified by means of bivariate data analysis of EC and MS (Baasch et al. 2015, 2016; Müller et al. 2012). Specifically, the GMB is identified by high EC and MS, the glaucony-sand facies by high MS and low EC, while the sands on the outer shelf show moderate EC and low MS values.

4.3.2 Electromagnetic measurements

The electromagnetic data used for this study have been recently described in Baasch et al. (2016). The data were acquired during the RV Meteor cruise M84/4b along three profiles, two of them run perpendicular and one parallel to the shore line (Fig. 4.2). The acquisition was carried out with the benthic profiler NERIDIS III developed at MARUM - Center for Marine Environmental Science at the University of Bremen, Germany (Baasch et al. 2015). The profiler is a bottom towed non-conductive, non-magnetic sled carrying a commercial broadband frequency-domain electromagnetic induction sensor (Won et al. 1997) customised for marine operations. The sled is towed on the seafloor ensuring a constant distance between the sensor and the ground

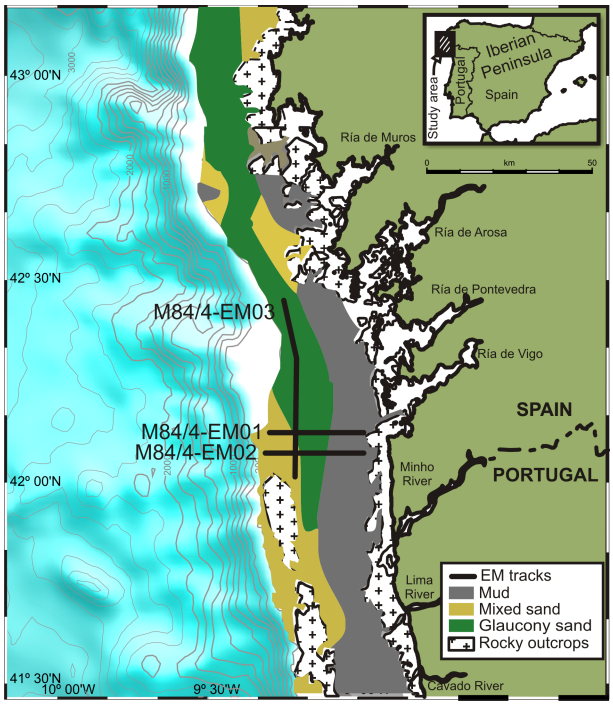

Figure 4.2: NW Iberian shelf. Colours indicate sediment facies, black lines indicate electromagnetic profiles from RV Meteor cruise M84/4b. Profile names are shown next to the lines. Modified from Lantzsch et al. (2010).

of typically 0.2 m. The electromagnetic data were acquired continuously along the ship track with a sampling rate of 25 Hz providing a very high spatial resolution.

The electromagnetic induction sensor consists of three co-axial and coplanar coils, namely source, receiver and bucking coil. The bucking coil cancels out the source transmitted primary field at the receiver coil location such that the receiver only measures the weaker secondary field. The secondary field can be expressed as in-phase and quadrature or out-of-phase component. The quadrature component is dominated by the induction of eddy currents in the conductive subsurface over the entire frequency ranges. In contrast, the low-frequency in-phase response is controlled by the magnetization of the subsurface. With increasing frequencies the influence of induction on the in-phase response increases. While the amplitude of the induction related in-phase and quadrature response increases with increasing frequency (within the frequency ranges considered here), the depth to which sediments influence this response decreases. Since the magnetization of the subsurface is frequency independent the depth of investigation of the related in-phase response is frequency independent, too. The multi-frequency transmitter signal was created by superimposing frequencies of 75, 175, 1025, 5025 and 10025 Hz with a pulse-width modulation technique

(Won et al. 1997).

The EC and MS of the subsurface sediments were reconstructed following a calibration and inversion approach described by (Baasch et al. 2015) and (Baasch et al. 2016), respectively: The electromagnetic data were corrected for instrument related bias by comparing and linear fitting the electromagnetic data measured in the water column to the desired seawater response calculated from seawater EC measured with a conductivity-temperature-depth (CTD) probe attached to the profiler and a constant MS of $-9 \cdot 10^{-6}$. Additionally, the secondary electromagnetic field was similarly calibrated using EC and MS ground-truth data measured on the collected sediment samples. EC was determined with a hand-held direct current probe with miniaturized four-electrode-in-line Wenner configuration and 4 mm electrode spacing. MS was measured with a laboratory susceptometer. To recover EC and MS of similar depth ranges the half-space inversion was performed in three steps: (1) in-phase and quadrature values of all five frequencies were inverted simultaneously for EC and MS. These values were used as a-priori information in the following inversion steps. (2) The high frequency quadrature response was used to recover EC. (3) The low-frequency in-phase response was inverted for MS. The recovered EC and MS are then a function of the sedimentary characteristics of the subsurface to a depth of approximately 0.9 m and 0.5 m, respectively (Müller et al. 2012).

4.3.3 Grains size analysis

During the Meteor cruise M84/4 sediment samples at 105 different locations across the NW Iberian shelf were taken. 33 of these sample locations lie on the three here presented electromagnetic profiles. Sediment sampling was performed using a Rumohr corer (100-cm-long gravity corer), a grab sampler and a box corer. In contrast to a conventional grab sampler and box corer the Rumohr corer allows probing the seafloor without disturbance of the surface sediments. The length of the recovered cores varied between 10 cm and 70 cm depending on sediment texture and coring device. For the GS analysis the cores were sub-sampled every 10 cm to 20 cm based on visual inspection. GS analyses were carried out with the Coulter LS 200 laser particle seizer. The volume distribution was divided in 92 logarithmically spaced size classes ranging from 0.39 to 2000 μm. Particles larger than 2000 μm (gravel) were not present in the sediment samples. The arithmetic mean of the vertical sub-samples at each sample location was taken for every individual GS class to get a single GSD for each sample location. These averaged GSD served as input for the end-member modelling. Three

of the 33 samples have not been considered in the RFBN training due to uncertainties in the sample localisation.

4.4 Results

4.4.1 Grain-size and end-member analysis

GSs of the 33 surface samples presented here have been recently discussed in Baasch et al. (2016). The sediments consist of predominately homogeneous medium to coarse silts and fine to medium sands with no or low content of coarse sands (Fig. 4.3).

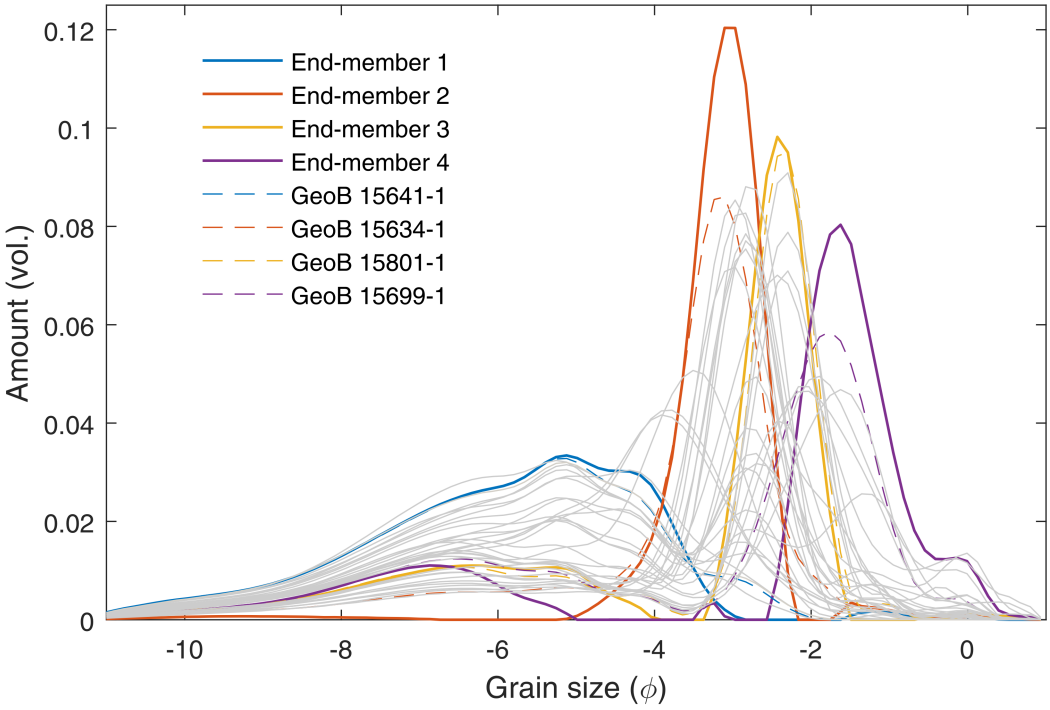

Figure 4.3: GSDs of the 33 surface samples (grey) and the four end-members (coloured solid line). The coloured dashed lines represent the GSDs of sediment samples most similar to the four end-members.

To determine the optimal number of end-members for the factorisation of the GSDs, the Frobenius norm of residuals

$$\|\mathbf{E}(L)\|_F = \|\mathbf{X} - \mathbf{A}(L)\mathbf{S}(L)\|_F \tag{4.11}$$

and the coefficient of determination were calculated and plotted versus the number of end-members L (Fig. 4.4). Naturally, it can be assumed that the points with the highest curvature of both graphs indicate the best compromise between number

of end-members and goodness of fit. In both graphs two distinct corner points are visible. The first occurs at $L = 3$ (point with highest curvature) and the second at $L = 5$. Considering that three end-members explain less than 90 % ($R^2 = 0.85$) of the GSD variance, we only further investigated the four ($R^2 = 0.94$) and five end-member ($R^2 = 0.98$) solutions. It was found out that the RBFN-GSD prediction performed better using the four end-member model. This is mainly because adding a fifth end-member leads to more very small values in the end-member frequency distributions which make the regression less stable. The choice of four end-members is also supported by cluster analysis carried out by Lantzsch et al. (2010) who discovered four main sedimentary facies.

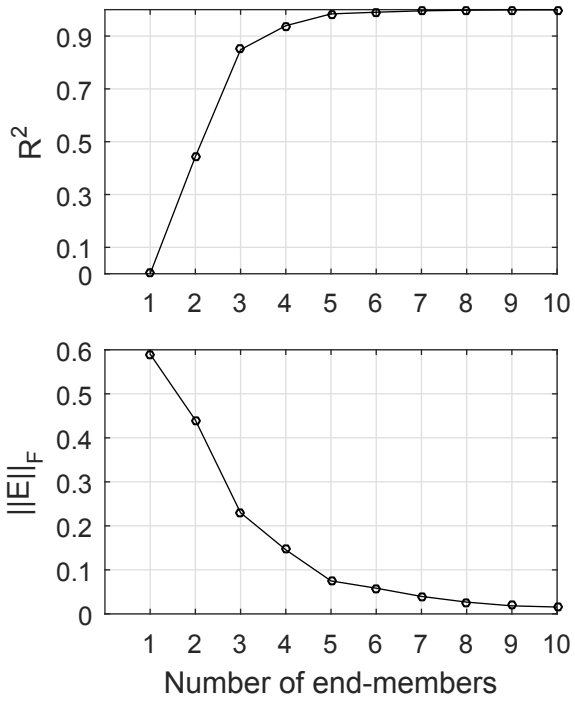

Figure 4.4: Coefficient of determination (top) and Frobenius norm of residuals (bottom) between measured GS and GS reconstructed from end-member modelling for different numbers of end-members.

The four end-members were sorted according to their modes such that End-member 1 has the smallest and End-member 4 the highest mode (Tab. 4.1). End-member 1 with a mean GS of 15.84 μm (silt fraction) represents the sediments from the GMB and is very similar to the GSD from core GeoB 15641-1 (Fig. 4.3), the core with the highest percentage of silt and clay. End-member 2 is characterised by a small standard deviation of 1.89 μm representing well sorted very fine sands from

the outer shelf. End-member 3 and 4 are bimodal end-members with dominant peaks in the fine and medium sand fraction (Fig. 4.3), respectively. Both have a distinct side peak in the silt fraction. Most similar sediments can be found in the Glaucony sediment facies of profile M84/4-EM03. In particular, End-member 3 represents the sediments in the troughs and End-member 4 those on the crests of the seafloor undulations. The four end-members have distinctive electromagnetic properties. Sediment samples with high abundances of a particular end-member build well defined clusters when represented in EC-MS cross-plots (Fig. 4.7 to Fig. 4.10). This suggests that there is high correspondence between GS end-members and electromagnetic clusters.

Table 4.1: Grain-size statistics of the four end-members.

	End-member 1	End-member 2	End-member	End-member4
Mode (μm)	28.70	116.27	185.35	324.40
Mean (μm)	15.84	108.08	74.71	141.45
Median (μm)	18.00	111.1	153.83	295.53
Standard deviation (μm)	3.43	1.89	4.64	6.23

4.4.2 Prediction of GSDs

Training and validation

Leave-one-out cross validation was performed to find the optimal regularisation parameter and to evaluate the performance of the end-member abundance prediction. Choosing successively one sample and predicting its end-member abundances from the RBFN which is trained using all the other samples provides a set of predicted data with the same size as the sample data set. The regularisation parameter was tested using values between 0.1 and 1. The Frobenius norm of residuals between the measured and predicted data and the coefficient of determination were calculated from the leave-one-out experiment for each regularisation parameter (Fig. 4.5). The lowest Frobenius norm of residuals and hence the best fit is achieved for a regularisation parameter value of 0.2 (Fig. 4.5, left). Although a value of 0.3 results in a slightly higher Frobenius norm of residuals this value was chosen because it maximises the lowest coefficient of determination (R^2) of the four end-members (Fig. 4.5, right) and thus offers a more consistent prediction accuracy between the different end-members.

The leave-one-out experiment using the optimal regularisation parameter of 0.3 reveals a high goodness of fit with R^2 values of 0.89, 0.78, 0.76 and 0.87 for End-member 1, End-member 2, End-member 3, and End-member 4, respectively (Fig. 4.6).

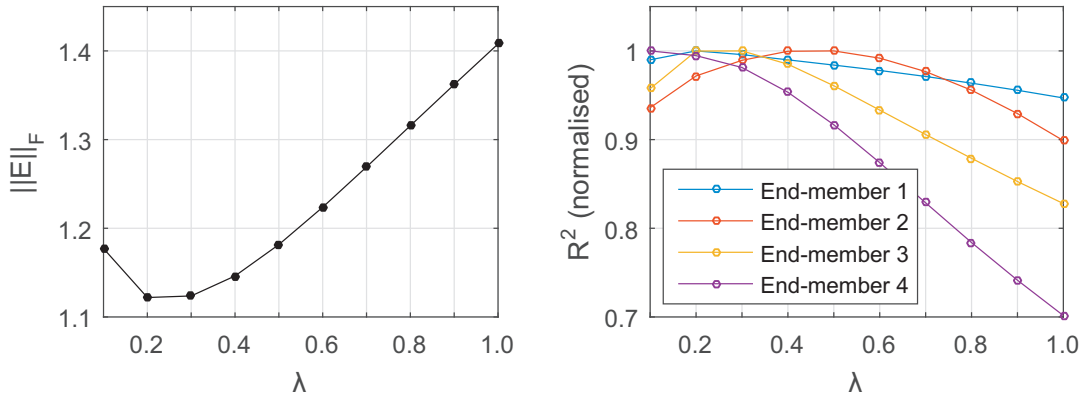

Figure 4.5: Frobenius norm of residuals between measured and predicted end-member abundances (left) and coefficient of determination for each end-member (R^2 normalised to self-peak, right) versus regularisation parameter λ.

The fact that the highest R^2 values are achieved for End-member 1 and 4 confirms the results of former studies that EC and MS are highly sensitive to the mud content (represented by End-member 1) and MS is sensitive to the paramagnetic glaucony represented by End-member 4.

RBFN prediction of end-member abundances

Representing the RBFN-derived end-member abundances for each electromagnetic measurement in a EC-MS cross-plot (Fig. 4.7 to Fig. 4.10) shows that clusters with high loadings are situated at distinct segments. High abundance of End-member 1 corresponds to high EC and high MS (Fig. 4.7), associated sediment samples are from cores retrieved from the GMB. For MS lower than $300 \cdot 10^{-6}$ the End-member 1 abundance does not exceed a value of 0.3. The abundance of End-member 2 (Fig. 4.8) has the highest values for susceptibilities below $250 \cdot 10^{-6}$ and conductivities between 0.6 and 1 S/m. All measurements within this EC-MS range originate from the outer shelf. High End-member 3 abundance corresponds with EC below 0.3 S/m and MS below $300 \cdot 10^{-6}$. End-member 4 shows similar electromagnetic characteristics with high abundances for low EC but higher MS ($330 \cdot 10^{-6}$ to $400 \cdot 10^{-6}$) than End-member 3. End-member 4 abundance is very low for EC higher than 0.6 S/m. The abundances of End-member 2 and End-member 3 in sample 54 and 04 are very different (Fig. 4.8 and Fig. 4.9), even though the EC and MS values are very similar. It is not clear why the electromagnetic properties do not reflect this GS variability, but inaccurate localisation of one or both samples might be the reason. It can be seen that the RBFN interpolation predicts smoother values than the underlying samples suggest,

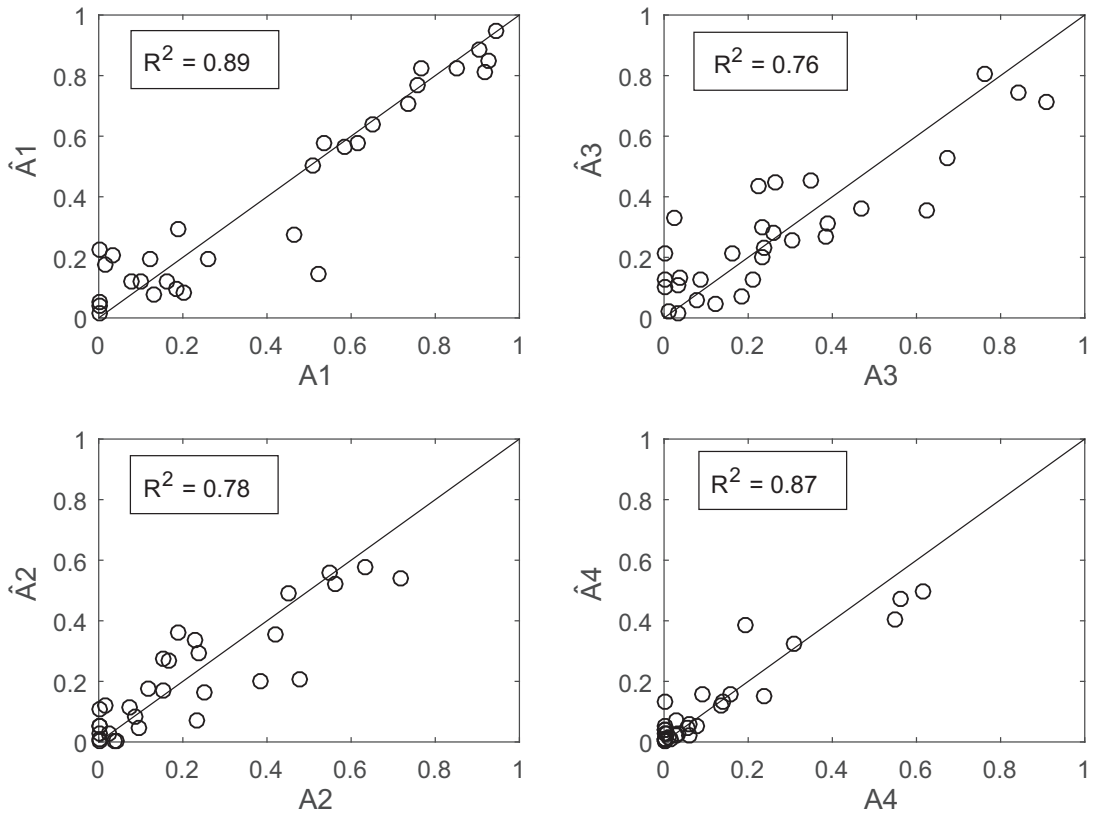

Figure 4.6: Comparison of end-member abundances ($\hat{\mathbf{A}}$) derived from the leave-one-out experiment and measured end-member abundances ($\mathbf{A}$) of the four different end-members.

this is to produce spatially consistent models and to avoid overfitting in areas where the electromagnetic data do not fully explain the GS variability.

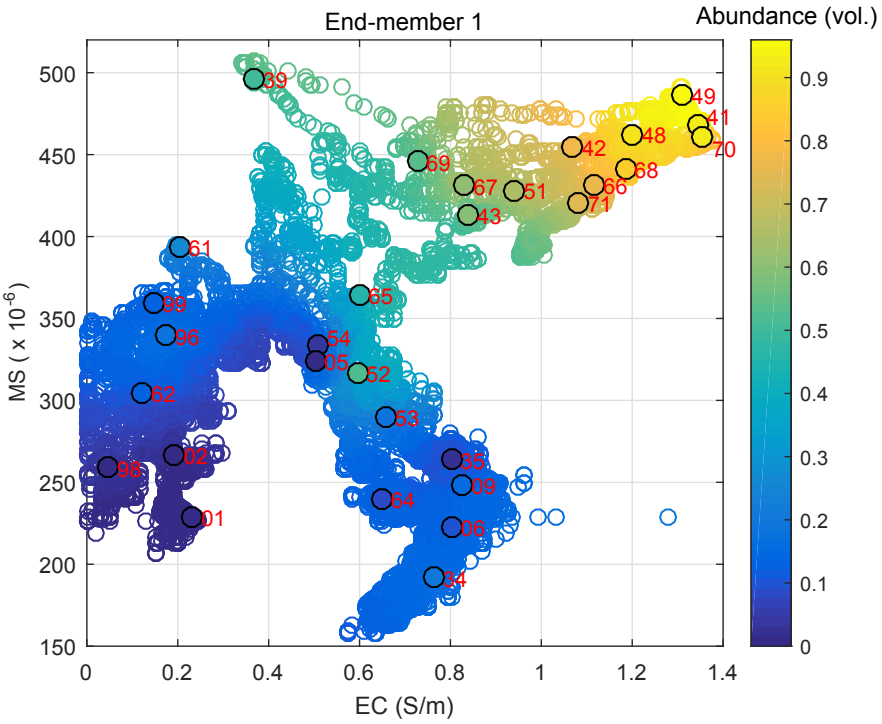

Figure 4.7: Cross plot, apparent MS versus apparent EC. Colour of circles indicates the loading of End-member 1. Filled circles indicate the end-member loadings from the training data (sediment-core samples). Red numbers show the last two digits of the GeoB-core number.

Spatial distribution of predicted end-members and grain sizes

The east-west profiles M84/4-EM01 (Fig. 4.11) and M84/4-EM02 (Fig. 4.12) both cross the Galician Mud Belt between 495000 m to 500000 m East. In this area EC and MS reach the highest values. The high amount of mud in this area is reflected in high End-member 1 contributions of up to over 90 per cent. Both profiles show a GS increase from the western edge of the mud belt towards the inner shelf which is related to a stronger wave impact towards the shore ((Lantzsch et al. 2009a). Correspondingly, the abundance of End-member 1 decreases while the End-member 2 abundance increases. This trend is stronger for profile M84/4-EM02 which could be linked to the steeper shoreward rise of the water bottom. The highest accumulation of mud occurs at the break of slope between the steeper inner shelf and flatter mid shelf on both profiles. In western direction the mud belt is followed by an area which

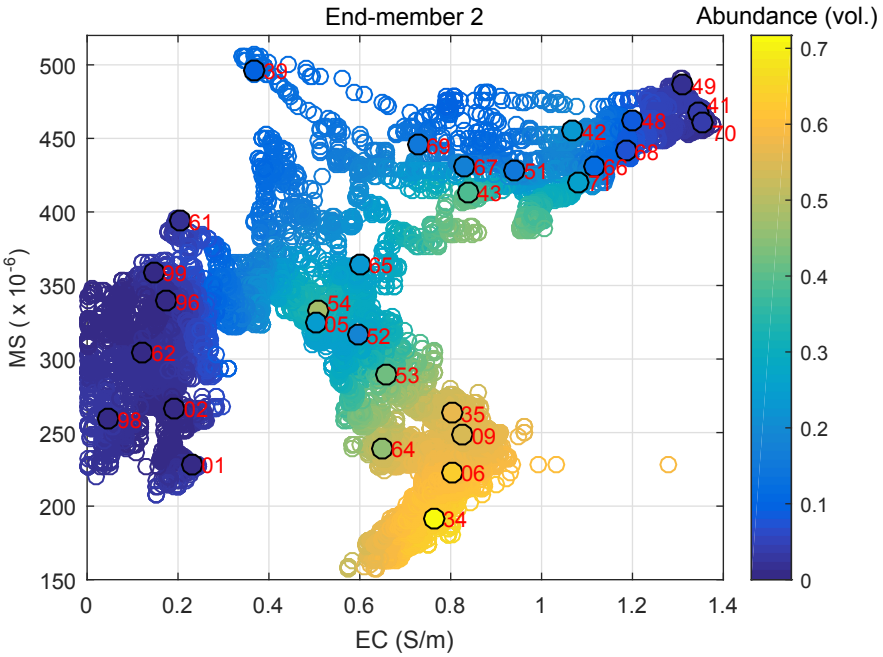

Figure 4.8: Cross plot, apparent MS versus apparent EC. Colour of circles indicates the loading of End-member 2. Filled circles indicate the end-member loadings from the training data (sediment-core samples). Red numbers show the last two digits of the GeoB-core number.

is characterised by sediment dunes and undulating EC and MS values. The dune's crests are represented by EC lows and MS highs, whilst the troughs show high EC and lower MS. This pattern has been earlier explained by local accumulations of mud in troughs (Baasch et al. 2015) and relatively higher paramagnetic glaucony content and higher compaction on crests (Müller et al. 2012). The predicted end-member abundances confirm this relationship between seabed topography, glaucony sand and mud abundance. End-member 1 and End-member 2 peak out in troughs and on crests, respectively. The GSDs are generally wide in this area, reflecting the sediment variety of this transition zone between mid-shelf mud belt and outer shelf. Towards the outer shelf GS and sorting of the trough's infill sediments increase. On the outer shelf End-member 2 dominates with contributions of over 60 % and hence GSDs are narrow representing highly sorted very fine to fine sands.

Profile M84/4-EM03 (Fig. 4.13) runs in a north-south direction on the outer shelf parallel to the coast line. In the south it is crosscut by the two other profiles. The predictive GSDs are very similar between the three profiles in the area where they overlap. Towards the north profile M84/4-EM03 passes a canyon. From the deepest point of the canyon towards the north the sedimentology changes distinctly. Abun-

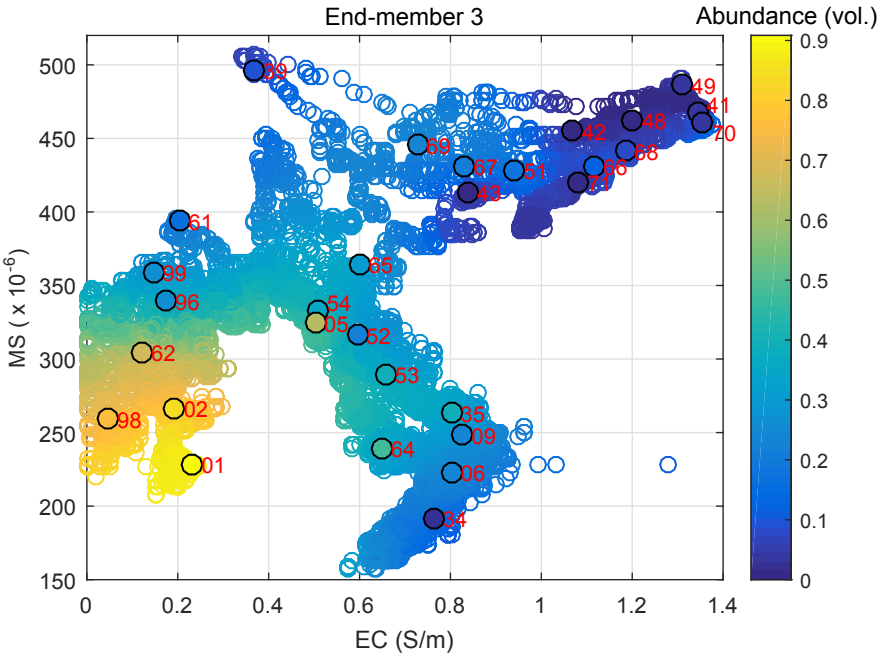

Figure 4.9: Cross plot, apparent MS versus apparent EC. Colour of circles indicates the loading of End-member 3. Filled circles indicate the end-member loadings from the training data (sediment-core samples). Red numbers show the last two digits of the GeoB-core number.

dance of End-member 4 increases and End-member 2 vanishes. In general, the main mode of the GS increases from south to north. Additionally, sediments change in north direction from a narrow unimodal distribution to a bimodal distribution with a side peak in the silt fraction. The northern end of the profile is characterised by rough seabed topography. Sediments at morphological highs have a higher proportion of End-member 4 (up to 60 %) and morphological lows have a higher proportion of End-member 3 (up to 90 %). The accumulation of End-member 4 at more exposed locations corresponds to the general assumption that Glaucony sands (mainly represented by End-member 4) are indicative for non-accumulating or erosional systems related to strong hydrodynamic forces.

4.5 Discussion

4.5.1 Electromagnetic profiling for sediment characterisation

Electromagnetic profiling as sediment characterisation tool has distinct advantages compared to other methods. It is a fast non- or minimal invasive technique which offers high spatial resolution and can be operated from small to large vessels. Although

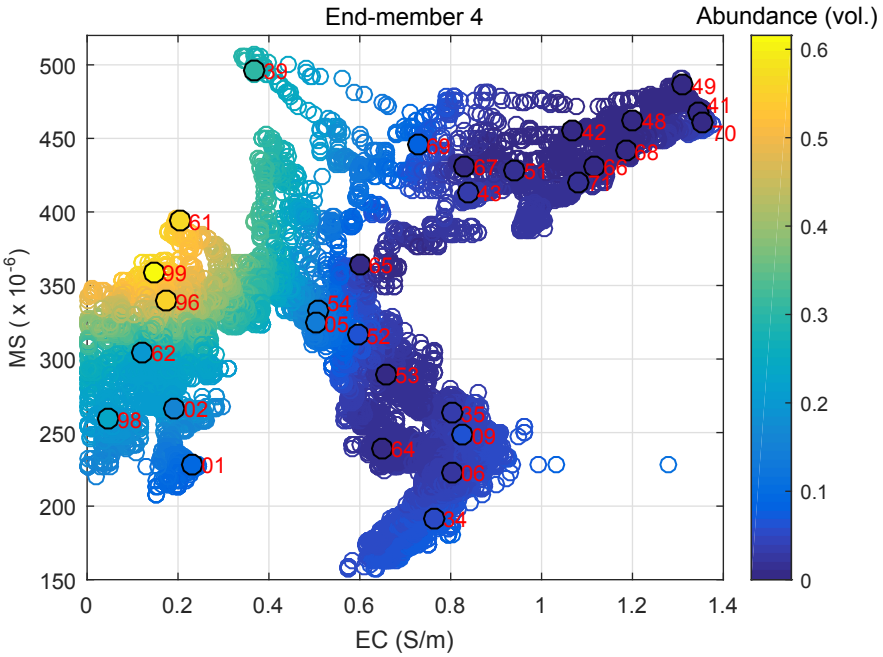

Figure 4.10: Cross plot, apparent MS versus apparent EC. Colour of circles indicates the loading of End-member 4. Filled circles indicate the end-member loadings from the training data (sediment-core samples). Red numbers show the last two digits of the GeoB-core number.

this is also true for acoustic methods, we showed that electromagnetic methods, unlike acoustic methods, can recover earth models with physical (electromagnetic) sediment properties through inversion. In contrast, acoustic methods measure backscatter features of the seabed which are not only influenced by sediment properties but also by the (micro) morphology of the seabed.

EC-MS-cross-plots revealed that different sediment types are represented by distinct clusters and hence enable an electromagnetic based sediment classification. These clusters well reflect GS based sediment types of this and former studies indicating a strong link between electromagnetic and textural sediment properties. The electromagnetic profiling based sediment classification can be used to define locations for sediment sampling and further investigations. The strong relationship between electromagnetic and textural properties can be mainly attributed to the sensitivity of EC and MS to mud content, the sensitivity of EC to sediment sorting and the sensitivity of MS to (coarse) paramagnetic Glaucony minerals. In other areas where no magnetic minerals are present, e.g. coastal areas with only quartz-bearing and carbonate sediments this relationship may be weaker. Additionally, in areas with fresh-water or gas seepages the relationship between EC and GS might be masked by

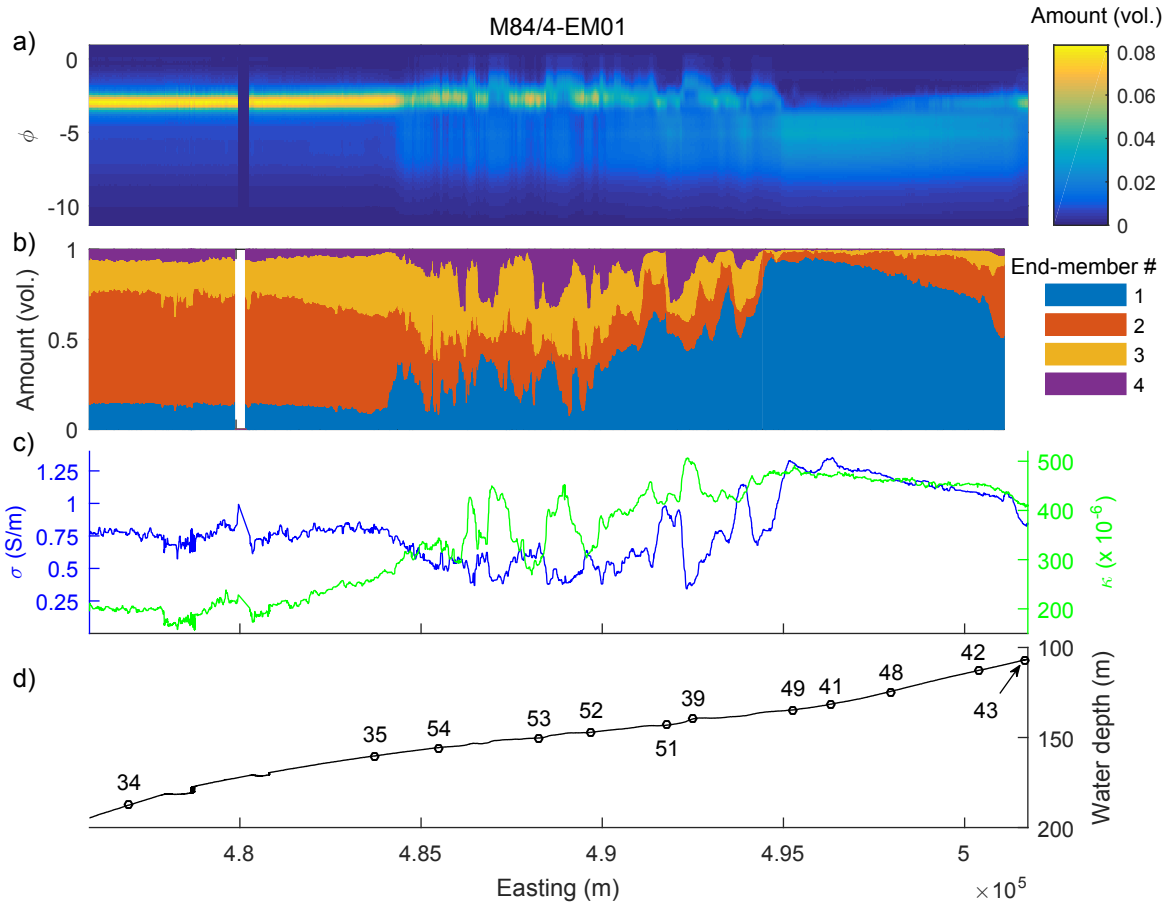

Figure 4.11: RBFN prediction results together with electromagnetic and bathymetric data along electromagnetic profile M84/4-EM01: a) Predicted GSD, b) predicted GSD end-member abundances, c) EC (blue line) and MS (green line), d) water depth, dots indicate surface sample locations and numbers indicate the two last digits of the GeoB core coring site.

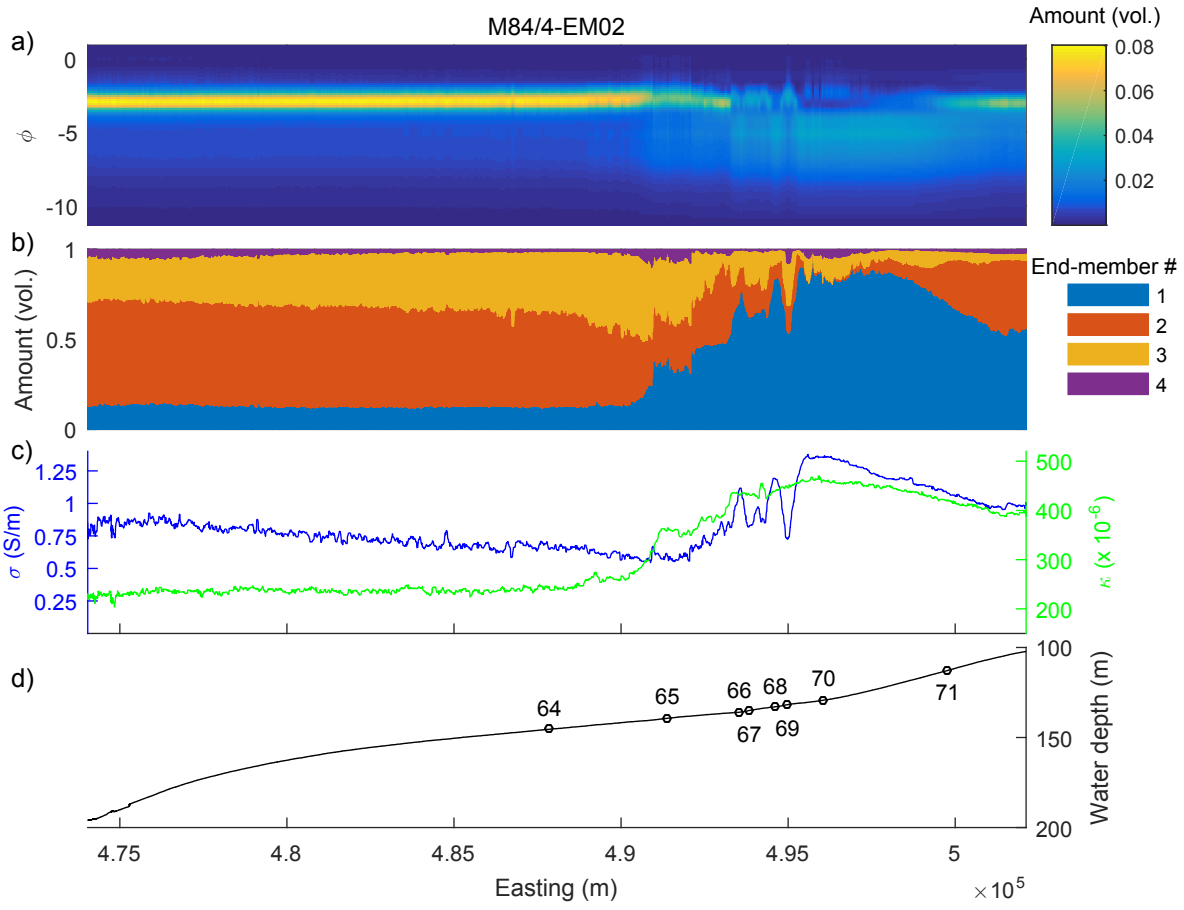

Figure 4.12: RBFN prediction results together with electromagnetic and bathymetric data along electromagnetic profile M84/4-EM02: a) Predicted GSD, b) predicted GSD end-member abundances, c) EC (blue line) and MS (green line), d) water depth, dots indicate surface sample locations and numbers indicate the two last digits of the GeoB core coring site.

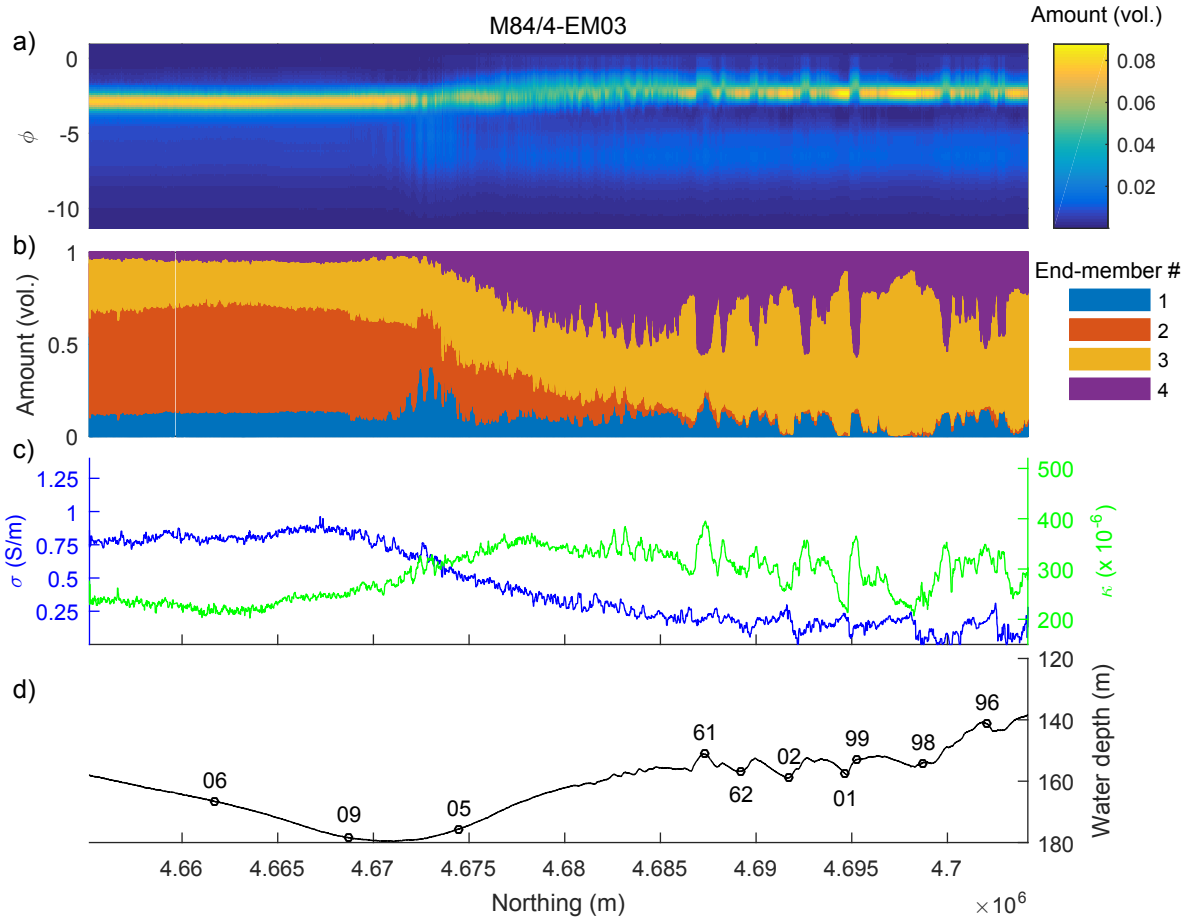

Figure 4.13: RBFN prediction results together with electromagnetic and bathymetric data along electromagnetic profile M84/4-EM03: a) Predicted GSD, b) predicted GSD end-member abundances, c) EC (blue line) and MS (green line), d) water depth, dots indicate surface sample locations and numbers indicate the two last digits of the GeoB core coring site.

the effect of variable pore-fluid on the sediment EC.

One constraint of the electromagnetic data presented here is that a homogeneous half-space is assumed in the inversion algorithm to recover EC and MS. Thus, lateral and vertical sediment changes within the electromagnetic sensor's footprint affect the reconstructed apparent EC and apparent MS. Consequently, the electromagnetic data are influenced by sediments of a certain volume. The size of this volume depends on the electromagnetic properties of the sediment and frequencies employed. Müller et al. (2012) specified the foot print of the EC related 5025 Hz quadrature signal and MS related 75 Hz in-phase signal to 3.5 m to 5.5 m and 1 m, respectively and the depth from which 90 % of the EC and MS information comes from to 92 cm and 50 cm, respectively. Comparing the electromagnetic data with sediment samples therefore means comparing bulk volume data with point data. This can be problematic if sediments have a high vertical or lateral variability which cannot be reflected by the diffusive nature of the electromagnetic method.

Another constraint is the localisation accuracy of the profiler and sampling devices to enable ground truthing at correct locations. Deviations between the profiler track and ground-truth locations naturally increase with current strength and water depth. A meaningful comparison of electromagnetic and ground-truth data is only feasible if the spatial sediment variability is small compared to the electromagnetic systems' footprint and positioning errors of the profiler and sampling device. Since the profiler is towed on the seafloor it is exposed to natural and artificial obstacles, which limits the application of the profiler in areas with rocky outcrops or man-made seafloor installations.

4.5.2 Prediction of compositional data

A GSD is a classic example of compositional data, meaning that no single GS fraction is free to vary separately from the rest of the total composition. This closure effect can cause misleading results if fractions of the GSD are predicted independently. The best solution is to predict the entire GSD. However, prediction of all GS classes (92 in this study) is not only computational expensive it is also numerically difficult because the abundances of the GS classes at both tails of the distribution are very low or zero for the majority of the sediment-samples. Additionally, not all GS classes are representative of certain sediment facies but rather have quasi constant abundances across all different sediment types. To overcome this problem we used a NMF algorithm to reduce the predicted parameters from 92 GS classes to four end-members with the goal to predict the abundances of these end-members rather than frequencies of the

GS classes directly. Other low rank factorizations, such as singular value decomposition or principal component analysis have not been tested here but could also be used for parameter reduction. It is worth mentioning that these techniques might require preconditioning of the compositional data in form of e.g. log-ratio transforms.

The main advantage of the end-member modelling is that it produces end-members which are directly interpretable. We showed that the NMF-derived end-members represent natural GSD end-members of the NW Iberian shelf sediments. The degree to which an end-member contributes to each sample offers valuable information for the sediment characterisation and can be used to define sediment patterns and corresponding transition/mixing zones. The spatial distribution of the end-member contributions can be used to create GS based facies maps. Furthermore, the end-members and its abundances carry all GS information and can be back-transformed into GS classes to reconstruct complete GSDs or to recover other statistical measures such as mean GS, sorting, skewness, number of modes etc. Just as the GSD the GS end-members are compositional data and thus their abundances are always positive and sum to one. These two inherent characteristics of compositional data need to be taken care of during the RBFN prediction. Since a conventional RBFN would violate both constraints we imposed positivity and the sum-to-one constraint of the end-member abundances in the RBFN learning algorithm. This means that RBFN predictions of all end-members need to be trained together.

4.5.3 Spatial constraining of the RBFN

In regression analysis various techniques exist to encounter overfitting attributed to noise in the data. Smoothing through regularisation is one of the most popular techniques to avoid overfitting (Girosi et al. 1995). Regularisation can be performed on the model parameters namely the weights in the RBFN. This approach is used in e.g. support vector regression where the norm of the weights is minimised together with the estimation error. Regularisation can also be performed on the output variables of the predictive model. In both cases the regularisation is conventionally implemented in the domain of the input variables (the feature space). Thus, output variables with similar input variables are constraint to be similar as well. This is a reasonable assumption in many applications.

In this paper we used a different regularisation approach, namely a minimum lateral variation constraint. It constraints the variability of the output variables (here the predicted GS end-member abundances) of neighbouring measurement points along the electromagnetic profile. This approach has the advantage that it respects spatial

correlations between the output data. Hence, it is not prone to instrument related acquisition footprints.

Another more straightforward way of incorporating spatial data in the RBFN training would be to include the spatial coordinates as predictor variables. In this case no distinction would be made between the spatial domain and the geophysical attributes pertaining to it. This would constrain the RBFN to learn from a limited range of coordinates simply because the RBFs of the hidden nodes produce a larger output when the input signal is close to the centre of the RBF. The problem is the two-dimensional nature of the electromagnetic profiling data acquisition that results in very high spatial data density along the profiles and a rather sparse density in cross-profile direction. This would affect the RBFN to produce models biased towards values along the profiles and hence would be similar to produce separate models for each profile.

In fact, incorporating spatial coordinates as input data requires that the training samples are randomly distributed within the spatial domain over the entire survey area (Cracknell and Reading 2014; Gahegan 2000) which is rarely the case. In contrast, our approach considers the centres and hence the sediment samples from all profiles equally because the Euclidean distance in the RBF is solely calculated from the electromagnetic properties rather than spatial coordinates. This enables the RBFN to predict the output variables in regions spatially disjoint from the training samples and thus minimised the total amount of sediment samples to be taken.

The drawback of the lateral variation constraint is that the matrix $\mathbf{\Phi}_d$ in eq. 4.10 which connects all electromagnetic measurement points to each centre can become very large and hence its computation and memory requirements can get expensive. In such a case we recommend splitting the profile into segments of reasonable size.

4.6 Conclusion

We have presented a new methodology to predict seafloor GSDs from geophysical data. An unsupervised end-member modelling approach based on nonnegative matrix factorisation is firstly used to reduce the number of target GS parameters from typically 92 GS classes to a minimum number of end-members. The end-member abundances are then predicted employing a RBFN which is trained using the geophysical data and end-member abundances at the sample location as input and target variables, respectively. The RBFN predicts the abundances for all end-member simultaneously enabling to incorporate a sum-to-constant constraint on the abundances.

This is approach respects the closure of the GSD which is a major advantage compared to previous studies that try to predict fractions of the GSD separately. In addition, the objective function to be minimised in the RBFN training includes a constraint penalising lateral variation between neighbouring predicted end-member abundances. This constraint allows a higher variability in the feature domain whilst avoiding over-fitting by incorporating spatial information. Not using this spatial information as explicit feature makes this approach preferable for spatially highly clustered sample data. The outputs of the RBFN, namely the predicted end-member abundances, can finally be back transformed to GSD.

The methodology was tested and validated using electromagnetic profiling data acquired on the NW Iberian shelf. Electromagnetic profiling is a new but established seafloor mapping technique. The electromagnetic data can be inverted for EC and MS of the seabed substrata, which both have proven to correlate with GS properties.

We have demonstrated that electromagnetic profiling in combination with machine learning approaches is capable to predict GSD with high accuracy and resolution along shelf-wide survey lines. This study suggests that electromagnetic benthic profiling in addition to acoustic methods should play a larger role for seabed characterization. However, our presented machine learning approach can be readily adapted to other geospatial problems which involve predictive modelling of compositional data from geophysical or remote sensing surveys. Therefore this study should also have an impact on e.g. acoustic seabed characterisation and benthic habitat mapping, mineral exploration and characterisation of spatial soil variability in precision agriculture.

References

Archie, G. (1942). "The electrical resistivity log as an aid in determining some reservoir characteristics". In: *Petroleum Transactions of AIME* 146, pp. 54–62.

Baasch, B., H. Müller, F. K. J. Oberle, and T. von Dobeneck (2015). "Inversion of marine multifrequency electromagnetic profiling data: a new approach to resolve surficial sediment stratification". In: *Geophysical Journal International* 200.1, pp. 438–451. DOI: 10.1093/gji/ggu406.

– (2016). "Determination of grain-size characteristics from electromagnetic seabed mapping data: A NW Iberian shelf study". In: *submitted to Continental Shelf Research*.

Berry, M. W., M. Browne, A. N. Langville, V. P. Pauca, and R. J. Plemmons (2006). "Algorithms and applications for approximate nonnegative matrix factorization". In: *Computational Statistics and Data Analysis*, pp. 155–173.

Billings, S. D., G. N. Newsam, and R. K. Beatson (2002). "Smooth fitting of geophysical data using continuous global surfaces". In: *GEOPHYSICS* 67.6, pp. 1823–1834. DOI: 10.1190/1.1527082.

Booth, C., J. Walden, A. Neal, and J. Smith (2005). "Use of mineral magnetic concentration data as a particle size proxy: A case study using marine, estuarine and fluvial sediments in the Carmarthen Bay area, South Wales, U.K." In: *Science of The Total Environment* 347.1 - 3, pp. 241–253. ISSN: 0048-9697. DOI: http://dx.doi.org/10.1016/j.scitotenv.2004.12.042.

Broomhead, D. S. and D. Lowe (1988). *Radial Basis Functions, Multi-Variable Functional Interpolation and Adaptive Networks*. Memorandum 4148. Malvern, Worcester, Great Britain: Royal Signals & Radar Establishment.

Brown, C. J., S. J. Smith, P. Lawton, and J. T. Anderson (2011). "Benthic habitat mapping: A review of progress towards improved understanding of the spatial ecology of the seafloor using acoustic techniques". In: *Estuarine, Coastal and Shelf Science* 92.3, pp. 502–520. ISSN: 0272-7714. DOI: http://dx.doi.org/10.1016/j.ecss.2011.02.007.

Butler, K. E. (2009). "Trends in waterborne electrical and EM induction methods for high resolution sub-bottom imaging". In: *Near Surface Geophysics*, pp. 241–246. ISSN: 18730604. DOI: 10.3997/1873-0604.2009002.

Cheesman, S. J., R. N. Edwards, and L. K. Law (1990). "A test of a short-baseline sea-floor transient electromagnetic system". In: *Geophysical Journal International* 103.2, pp. 431–437. ISSN: 0956540X. DOI: 10.1111/j.1365-246X.1990.tb01782.x.

Cracknell, M. J. and A. M. Reading (2014). "Geological mapping using remote sensing data: A comparison of five machine learning algorithms, their response to variations in the spatial distribution of training data and the use of explicit spatial information". In: *Computers & Geosciences* 63, pp. 22–33. ISSN: 0098-3004. DOI: http://dx.doi.org/10.1016/j.cageo.2013.10.008.

De, C. and B. Chakraborty (2009). "Acoustic Characterization of Seafloor Sediment Employing a Hybrid Method of Neural Network Architecture and Fuzzy Algorithm". In: *IEEE Geoscience and Remote Sensing Letters* 6.4, pp. 743–747. ISSN: 1545-598X. DOI: 10.1109/LGRS.2009.2024438.

Dias, J. M. A., J. M. Jouanneau, R. Gonzalez, M. F. Araújo, T. Drago, C. Garcia, A. Oliveira, A. Rodrigues, J. Vitorino, and O. Weber (2002). "Present day sedimentary processes on the northern Iberian shelf". In: *Progress In Oceanography* 52.2-4, pp. 249–259. ISSN: 0079-6611. DOI: DOI:10.1016/S0079-6611(02)00009-5.

Diesing, M. and D. Stephens (2015). "A multi-model ensemble approach to seabed mapping". In: *Journal of Sea Research* 100. MeshAtlantic: Mapping Atlantic Area Seabed Habitats for Better Marine Management, pp. 62–69. ISSN: 1385-1101. DOI: http://dx.doi.org/10.1016/j.seares.2014.10.013.

Eberle, D., D. Hutchins, S. Das, A. Majumdar, and H. Paasche (2015). "Automated pattern recognition to support geological mapping and exploration target generation - A case study from southern Namibia". In: *Journal of African Earth Sciences* 106, pp. 60–74. ISSN: 1464-343X. DOI: http://dx.doi.org/10.1016/j.jafrearsci.2015.03.011.

Evans, R. L. (2001). "Measuring the shallow porosity structure of sediments on the continental shelf: A comparison of an electromagnetic approach with cores and acoustic backscatter". In: *J. geophys. Res.* 106.C11, pp. 27047–27060. ISSN: 0148-0227.

Gahegan, M. (2000). "On the Application of Inductive Machine Learning Tools to Geographical Analysis". In: *Geographical Analysis* 32.2, pp. 113–139. ISSN: 1538-4632. DOI: 10.1111/j.1538-4632.2000.tb00420.x.

Girosi, F., M. Jones, and T. Poggio (1995). "Regularization Theory and Neural Networks Architectures". In: *Neural Computation* 7, pp. 219–269.

Heil, K. and U. Schmidhalter (2012). "Characterisation of soil texture variability using the apparent soil electrical conductivity at a highly variable site". In: *Computers & Geosciences* 39, pp. 98–110. ISSN: 0098-3004. DOI: http://dx.doi.org/10.1016/j.cageo.2011.06.017.

Huang, Z., S. L. Nichol, J. P. Siwabessy, J. Daniell, and B. P. Brooke (2012). "Predictive modelling of seabed sediment parameters using multibeam acoustic data: a case study on the Carnarvon Shelf, Western Australia". In: *International Journal of Geographical Information Science* 26.2, pp. 283–307. DOI: 10.1080/13658816.2011.590139.

Huang, Z., J. Siwabessy, S. Nichol, T. Anderson, and B. Brooke (2013). "Predictive mapping of seabed cover types using angular response curves of multibeam backscatter data: Testing different feature analysis approaches". In: *Continental Shelf Research* 61-62, pp. 12–22. ISSN: 0278-4343. DOI: http://dx.doi.org/10.1016/j.csr.2013.04.024.

Huang, Z., J. Siwabessy, S. L. Nichol, and B. P. Brooke (2014). "Predictive mapping of seabed substrata using high-resolution multibeam sonar data: A case study from a shelf with complex geomorphology". In: *Marine Geology* 357, pp. 37–52. ISSN: 0025-3227. DOI: http://dx.doi.org/10.1016/j.margeo.2014.07.012.

Jackson, D. R. and K. B. Briggs (1992). "High-frequency bottom backscattering: Roughness versus sediment volume scattering". In: *The Journal of the Acoustical Society of America* 92.2, pp. 962–977. DOI: http://dx.doi.org/10.1121/1.403966.

Jackson, P. D., D. T. Smith, and P. N. Stanford (1978). "Resistivity-porosity-particle shape relationships for marine sands". In: *GEOPHYSICS* 43.6, pp. 1250–1268. DOI: 10.1190/1.1440891.

Just, J., D. Heslop, T. von Dobeneck, T. Bickert, M. J. Dekkers, T. Frederichs, I. Meyer, and M. Zabel (2012). "Multiproxy characterization and budgeting of terrigenous end-members at the NW African continental margin". In: *Geochemistry, Geophysics, Geosystems* 13.9. Q0AO01. ISSN: 1525-2027. DOI: 10.1029/2012GC004148.

Lantzsch, H., T. J. Hanebuth, and V. B. Bender (2009a). "Holocene evolution of mud depocentres on a high-energy, low-accumulation shelf (NW Iberia)". In: *Quaternary Research* 72.3, pp. 325–336. ISSN: 00335894. DOI: 10.1016/j.yqres.2009.07.009.

Lantzsch, H., T. J. Hanebuth, V. B. Bender, and S. Krastel (2009b). "Sedimentary architecture of a low-accumulation shelf since the Late Pleistocene (NW Iberia)". In: *Marine Geology* 259.1-4, pp. 47–58. ISSN: 00253227. DOI: 10.1016/j.margeo.2008.12.008.

Lantzsch, H., T. J. Hanebuth, and R. Henrich (2010). "Sediment recycling and adjustment of deposition during deglacial drowning of a low-accumulation shelf (NW Iberia)". In: *Continental Shelf Research* 30.15, pp. 1665–1679. ISSN: 02784343. DOI: 10.1016/j.csr.2010.06.013.

Lawson, C. L. and R. J. Hanson (1995). "23. Linear Least Squares with Linear Inequality Constraints". In: *Solving Least Squares Problems*. Classics in Applied Mathematics. SIAM. Chap. 23, pp. 158–173. DOI: 10.1137/1.9781611971217.ch23.

Müller, H., T. von Dobeneck, C. Hilgenfeldt, B. SanFilipo, D. Rey, and B. Rubio (2012). "Mapping the magnetic susceptibility and electric conductivity of marine surficial sediments by benthic EM profiling". In: *Geophysics* 77.1, E43–E56. ISSN: 0016-8033. DOI: 10.1190/geo2010-0129.1.

Oberle, F. K., T. J. Hanebuth, B. Baasch, and T. Schwenk (2014a). "Volumetric budget calculation of sediment and carbon storage and export for a late holocene mid-shelf mudbelt system (NW Iberia)". In: *Continental Shelf Research* 76.0, pp. 12–24. ISSN: 0278-4343. DOI: http://dx.doi.org/10.1016/j.csr.2013.12.012.

Oberle, F. K., C. D. Storlazzi, and T. J. Hanebuth (2014b). "Wave-driven sediment mobilization on a storm-controlled continental shelf (Northwest Iberia)". In: *Journal of Marine Systems* 139, pp. 362–372. ISSN: 0924-7963. DOI: http://dx.doi.org/10.1016/j.jmarsys.2014.07.018.

Oberle, F. K., P. W. Swarzenski, C. M. Reddy, R. K. Nelson, B. Baasch, and T. J. Hanebuth (2016a). "Deciphering the lithological consequences of bottom trawling to sedimentary habitats on the shelf". In: *Journal of Marine Systems* 159, pp. 120–131. ISSN: 0924-7963. DOI: http://dx.doi.org/10.1016/j.jmarsys.2015.12.008.

Oberle, F. K., C. D. Storlazzi, and T. J. Hanebuth (2016b). "What a drag: Quantifying the global impact of chronic bottom trawling on continental shelf sediment". In: *Journal of Marine Systems* 159, pp. 109–119. ISSN: 0924-7963. DOI: http://dx.doi.org/10.1016/j.jmarsys.2015.12.007.

Odin, G. and M. Lamboy (1988). "Glaucony From The Margin off Northwestern Spain". In: *Green Marine Clays*. Ed. by G. Odin. Elsevier, pp. 249–275. DOI: http://dx.doi.org/10.1016/S0070-4571(08)70067-0.

Oldfield, F., B. A. Maher, J. Donoghue, and J. Pierce (1985). "Particle-size related, mineral magnetic source sediment linkages in the Rhode River catchment, Maryland, USA". In: *Journal of the Geological Society* 142.6, pp. 1035–1046. DOI: 10.1144/gsjgs.142.6.1035.

Oliveira, A., F. Rocha, A. Rodrigues, J. Jouanneau, A. Dias, O. Weber, and C. Gomes (2002). "Clay minerals from the sedimentary cover from the Northwest Iberian shelf". In: *Progress in Oceanography* 52.2 - 4, pp. 233–247. ISSN: 0079-6611. DOI: http://dx.doi.org/10.1016/S0079-6611(02)00008-3.

Paasche, H., J. Tronicke, K. Holliger, A. G. Green, and H. Maurer (2006). "Integration of diverse physical-property models: Subsurface zonation and petrophysical parameter estimation based on fuzzy c -means cluster analyses". In: *GEOPHYSICS* 71.3, H33–H44. DOI: 10.1190/1.2192927.

Paatero, P. and U. Tapper (1994). "Positive matrix factorization: A non-negative factor model with optimal utilization of error estimates of data values". In: *Environmetrics* 5.2, pp. 111–126. ISSN: 1099-095X. DOI: 10.1002/env.3170050203.

Schwalenberg, K., M. Haeckel, J. Poort, and M. Jegen (2010). "Evaluation of gas hydrate deposits in an active seep area using marine controlled source electromagnetics: Results from Opouawe Bank, Hikurangi Margin, New Zealand". In: *Marine Geology* 272.1-4, pp. 79–88. ISSN: 0025-3227. DOI: http://dx.doi.org/10.1016/j.margeo.2009.07.006.

Swidinsky, A., S. Hölz, and M. Jegen (2015). "Rapid resistivity imaging for marine controlled-source electromagnetic surveys with two transmitter polarizations: An application to the North Alex mud volcano, West Nile Delta". In: *GEOPHYSICS* 80.2, E97–E110. DOI: 10.1190/geo2014-0015.1.

Won, I., D. Keiswetter, D. Hanson, E. Novikova, and T. Hall (1997). "GEM-3: A Monostatic Broadband Electromagnetic Induction Sensor". In: *Journal of Environmental and Engineering Geophysics* 2.1, pp. 53–64. DOI: 10.4133/JEEG2.1.53.

Chapter 5

Conclusions and perspectives

This thesis demonstrates the great potential of EM profiling data to quantify physical properties of near-surface seafloor sediments. An entire processing sequence from the raw data to the final grain-size model is described.

Inverse modelling provides the mathematical framework for reconstructing electric conductivity and magnetic susceptibility subsurface models. Machine learning helps us to make statistical inference, to cluster and classify the data and to find relationships to other sediment parameters which than can be predicted from the geophysical data.

The fact that inversions try to recover earth properties, which are inherently continuously distributed, from spatially and temporally discrete geophysical data, make the inverse problem ill-posed. Therefore, the forward model needs to represent the data as accurate as possible to obtain reliable inversion results. This means that not only the mathematical description of the physical problem needs to be precise it also means that the noise needs to be low, preferably uncorrelated and known to control the inversion trough weighting of the data. This is especially true for 1-D (or higher dimensional) inversions, where the depth of investigation is drastically reduced if the noise increases. A classical approach to stabilise the solution of ill-posed problems is regularisation. In this thesis vertical and lateral minimum-variation constraints were combined to regularise the 1-D inversion. Constraining the data in more than one dimension avoids over-smoothing in e.g. the vertical direction in the presence of stronger noise and therefore increases the depth resolution. Additionally, unacceptable site to site variations are prevented. Nevertheless, for too noisy data the inversion is dominated by the regularisation and thus produces overly smooth models.

Standard processes such as stacking, mean and median filtering can be used to remove random and spiky noise. The corresponding loss of resolution can in most cases be mitigated by the possible high spatial (sub-meter) sampling rate of the EM sensor.

However, strong system related bias was observed in the presented EM data from the NW Iberian shelf which demanded data calibration prior to the inversion. The data were successfully calibrated employing a two-step calibration approach which firstly calibrates the primary EM field and then the secondary EM field. The primary field calibration is straightforward using independently CTD-measured water conductivity and constant water susceptibility. The secondary field calibration is more challenging because an artificial secondary field source is difficult to place and remove while the EM sensor is underwater. Alternatively, the secondary field component was calibrated by means of ground-truth conductivity and susceptibility measurements. This approach faces the problem that the errors in the sample measurements, which were remarkably high for the conductivity probe, and errors due to discrepancies between the profiler and sample locations affect the calibration. It is worth mentioning that the source of this bias is not fully understood and that further investigations are required to be able to manage this problem without relying on ground-truth data.

The recovered half-space conductivity and susceptibility presented in this thesis well reflect the main sediment facies and can hence be used for EM based sediment classification. However, electric conductivity and magnetic susceptibility might be unfamiliar parameters for sedimentologists and engineers who generally commission the sediment characterisation surveys. It is thus worthwhile to translate the EM parameters, if possible, into conventional sediment parameters.

Multiple regression analysis revealed strong relations between the EM and textural sediment properties. These results motivated the development of a predictive modelling approach which estimates grain-sizes from electric conductivity and magnetic susceptibility. The presented approach combines unsupervised and supervised learning methods to predict grain-sizes from the EM properties. It is to the author's knowledge the first predictive modelling approach which estimates entire grain-size distributions from geophysical data. The results of the predictive modelling showed that EM profiling in combination with machine learning techniques is a promising tool for sediment characterisation. In the next step relationships of the EM data to other biological, chemical and physical sediment parameters such as density and total organic carbon should be investigated and predictive models developed.

The NERIDIS III profiler is designed as a multi-sensor platform and carries besides the EM sensor, a CTD, a turbidity sensor and a motion sensor and can additionally be equipped with a high-resolution camera with LED flashlights to obtain seabed photographs. Combining these sensor data with the EM and if available sonar data has the potential to further improve the predictive models without extra cost.

In the age of big data and internet of things statistical methods such as data mining and machine learning evolve with an unprecedented pace offering new possibilities for all geoscientific disciplines to address data-driven spatial inference problems.

Appendices

Appendix A

Vertical porosity structure of surficial sediments on the NW Iberian shelf

Half-space electric conductivity and magnetic susceptibility, as well as the 1-D electric conductivity structure were recovered as explained in chapter 2. Electric conductivity was transformed to porosity using Archie's law (eq. 1.1). All three profiles acquired during the Meteor cruise M84/4b are presented (Fig. A.1 and A.3).

The EM surface electric conductivity and magnetic susceptibility represent the known sediment facies (indicated by background colours), with fine resolution of transitions. The two W-E profiles (Fig. A.1 and A.2) show a gradual narrowing of the mixed sand facies from south to north, while the glaucony sand facies widens. The topography of this facies is controlled by dipped sediment layers beneath the surface causing undulations of the seafloor with wave length of 2-3 km, which are reflected in high porosity values in troughs and minor porous sediments with high susceptibility on the crests. This can be interpreted as an alternation of glauconized sand ridges and troughs filled with modern, muddy sediments. The reconstructed 1-D porosity distributions reveal remarkable stratifications within the uppermost three meters. On the mid-shelf mud belt sediments between 1 and 1.5 m show the highest porosity while the younger overlying mud has lower porosity. This inverse layering indicates a change in the fines composition at the source area towards coarser material or changes in the hydrodynamic conditions resulting in increased transport energy.

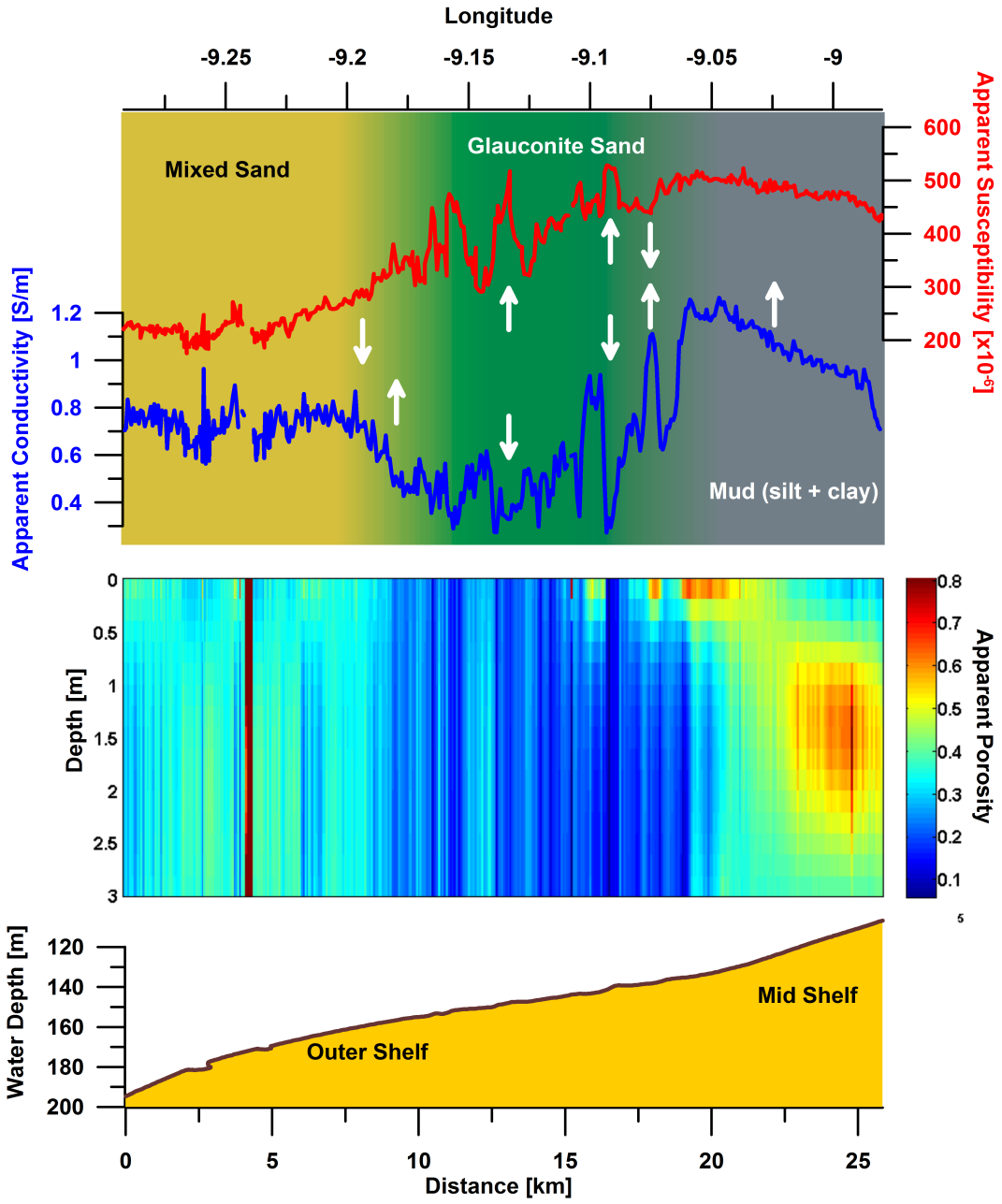

Figure A.1: Profile M84/4-EM01: Half-space magnetic susceptibility and porosity (top), Pseudo 2-D porosity representation (middle), CTD-measured bathymetry (bottom).

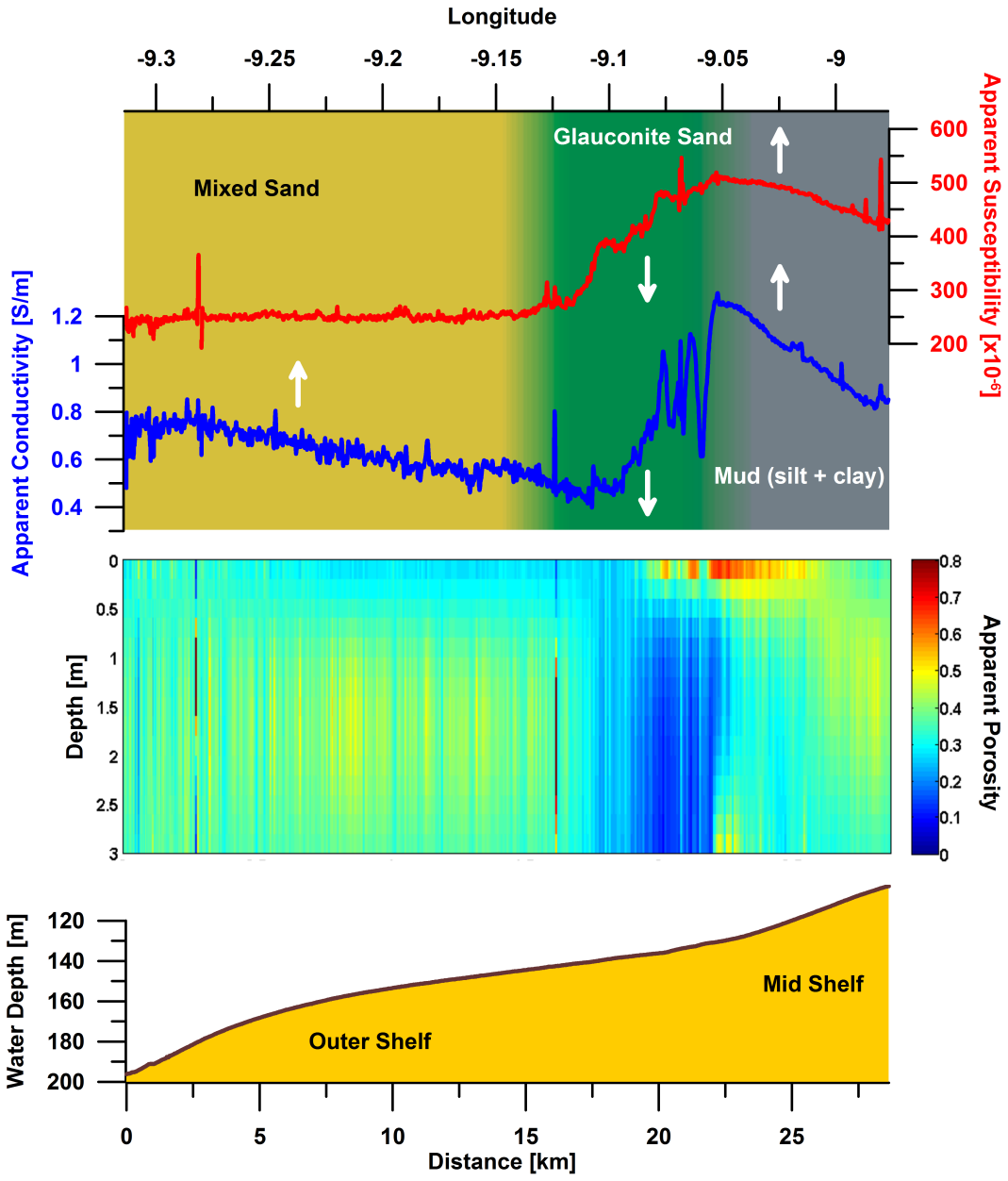

Figure A.2: Profile M84/4-EM02: Half-space magnetic susceptibility and porosity (top), Pseudo 2-D porosity representation (middle), CTD-measured bathymetry (bottom).

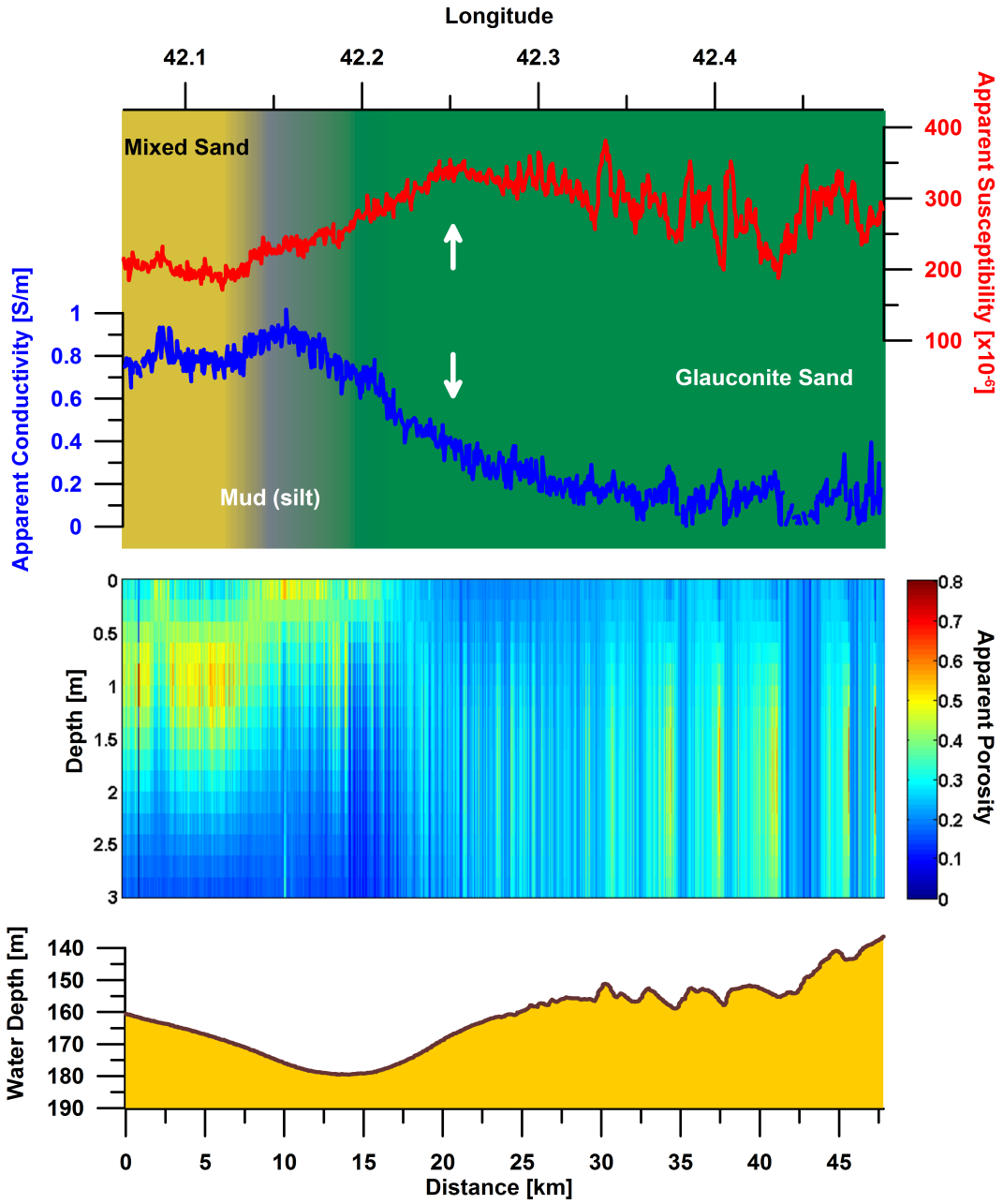

Figure A.3: Profile M84/4-EM03: Half-space magnetic susceptibility and porosity (top), Pseudo 2-D porosity representation (middle), CTD-measured bathymetry (bottom).

Appendix B

Comparison of electromagnetic properties with acoustic backscatter

Half-space electric conductivity and magnetic susceptibility of profile M84/4-EM01 are compared with acoustic backscatter measured with a multi beam echo sounder.

Three main sediment facies can be discriminated:

1. Outer shelf mixed sands: low susceptibility, intermediate to high porosity, the lowest backscatter intensity.
2. Glaucony sand facies: high susceptibility, low porosity, highest backscatter.
3. Mud belt: high susceptibility, high porosity, intermediate backscatter.

Positive linear correlations of susceptibility and porosity indicates fining or coarsening, while negative correlation indicates glauconization.

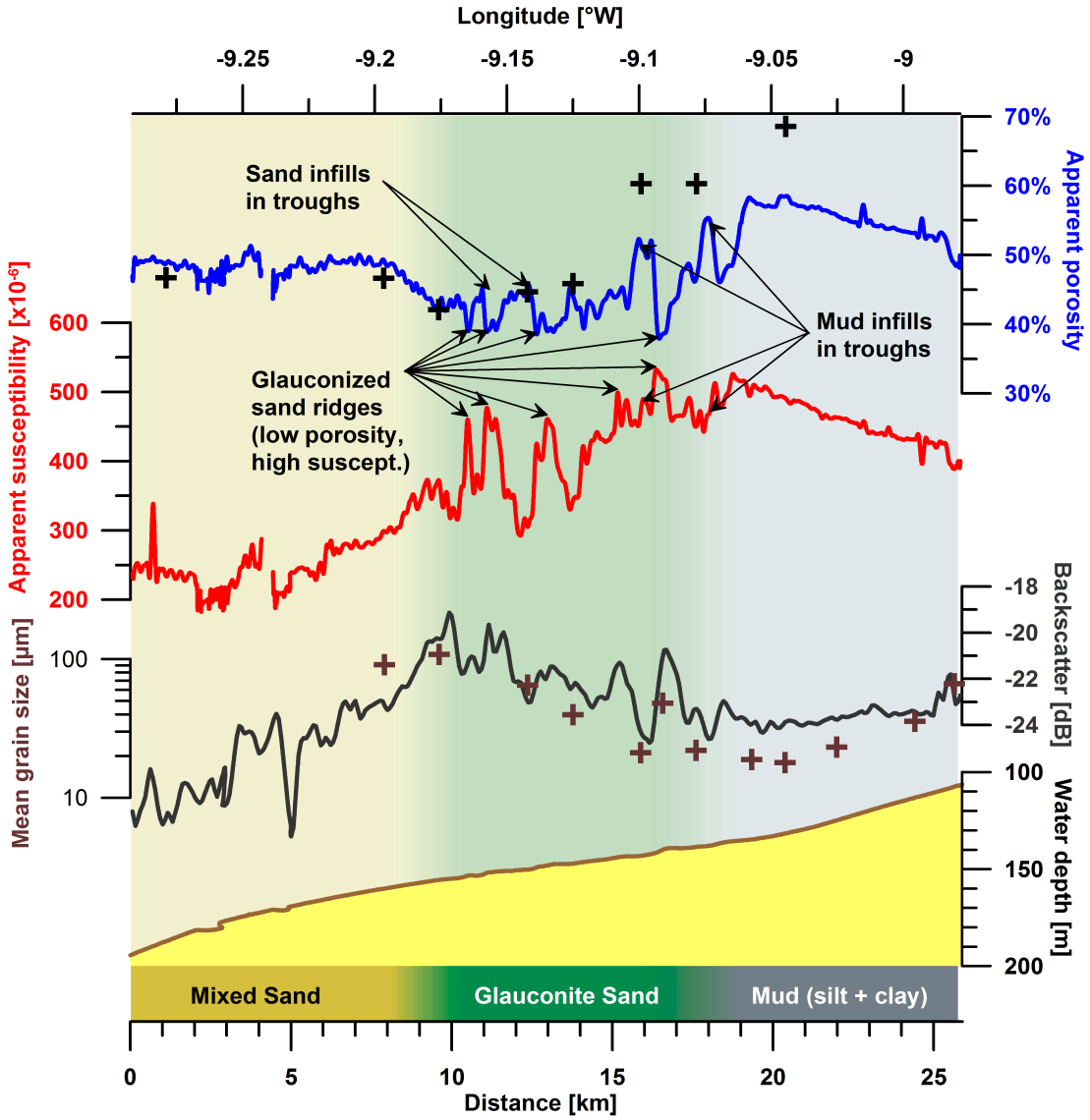

Figure B.1: Profile M84/4-EM01: EM Half-space magnetic susceptibility and porosity (crosses indicate laboratory measurements at surface samples) together with acoustic backscatter and grain-size from surface samples.

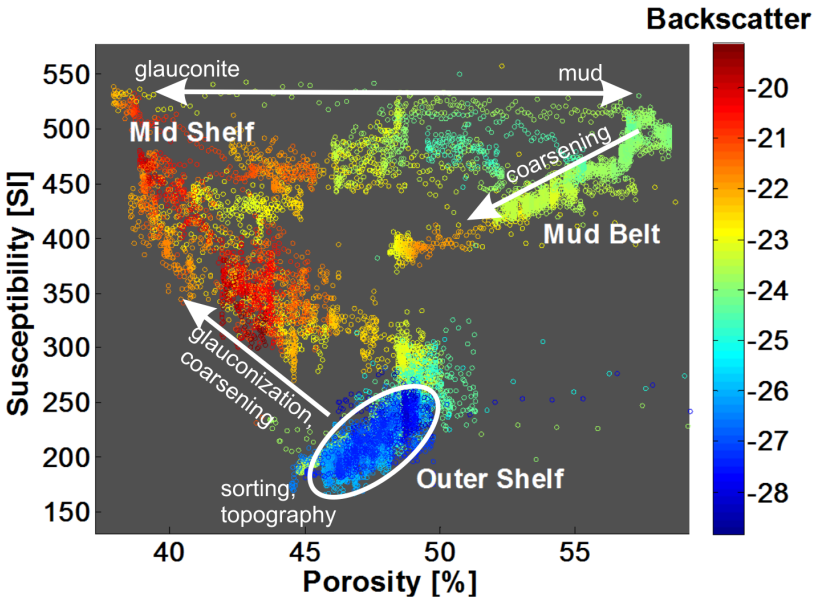

Figure B.2: Cross-plot shows magnetic susceptibility versus sediment porosity of profile M84/4-EM01. Colour indicates backscatter intensity.

Appendix C

Volumetric budget calculation of sediment and carbon storage and export for a late Holocene mid-shelf mudbelt system (NW Iberia)

Ferdinand K.J. Oberle, Till J.J. Hanebuth, Benjamin Baasch, Tilmann Schwenk, *Continental Shelf Research* 2014, 76, 12–24.

Confined fine-grained depocenters (mudbelts) on continental shelves play an important role as common and major fluviogenic submarine depocenters along the source-to-sink pathway and in global sedimentary and carbon cycles. This study provides a complete high-resolution isopach-based budget analysis using closely-spaced, high-resolution seismic-reflection data of an exemplary mid-shelf mudbelt system located on the open and narrow continental shelf of NW Iberia. The budget analysis reveals that 3.957-4.227 km^3 of sediments [i.e., 4073 to 4351 Mt (dry)] are stored in this depocenter. In conjunction with river-discharge estimates, we calculate that, over the past 5300 yr, approximately 34% to 36% of total fluvial sediments supplied to the ocean remain in the shelfal mud depocenter and the balance bypasses the shelf. Total accumulation values for TOC and CaCO3 amount to 40.31 to 43.46 t and 174.73 to 186.68 Mt, respectively. High-resolution isopach analysis shows high regional morphodynamic variability of the main sediment transit routes, an aspect easily over-looked by core-based or low-resolution profiling studies. The budget analysis reveals persistent low accumulation over the past 5300 yr and thus clarifies that a uniformitarian view of applying modern accumulation rates to the late Holocene can significantly underestimate effective sediment off-shelf transport.

Appendix D

Deciphering the lithological consequences of bottom trawling to sedimentary habitats on the shelf

Ferdinand K.J. Oberle, Peter W. Swarzenski, Christopher M. Reddy, Robert K. Nelson, Benjamin Baasch, Till J.J. Hanebuth, *Journal of Marine Systems* 2016, 159, 120–131.

Widespread bottom trawling on the NW Iberian shelf causes chronic sediment and habitat disturbance. The few studies that have investigated vessel-modified sedimentary-structure and texture of the seabed have typically classified their results as being either impacted by trawling or not. This study indicates that bottom trawling can result in a sequence of vastly different effects to the lithology of seabed sediment, which have in turn different ecological consequences. Here, we combined very high-resolution spatial bottom-trawling data with sedimentological (grain size, porosity) and geochemical datasets (excess ^{210}Pb, 3D petroleum fingerprinting) to study sediment disturbance, including sorting and mixing. Our results were used to develop five conceptual disturbance scenarios: minimal seabed effects, sediment overturning, complete sediment mixing, sediment grading and layering, and loss of sediment. Considering that bottom trawling is a widespread and growing global fishing technique, such impacts need to be considered in the management of habitat conservation as well as in the reconstruction of late Holocene climate history from shallow-water deposits, not just on the NW Iberian shelf, but also globally.